Eingefrorene Unordnung
und
Magnetismus
in
$TiFe_2$ Laves-Phase-Dünnschichten

Dissertation
zur Erlangung des Grades
Doktor der Naturwissenschaften (Dr. rer. nat.)
am Fachbereich Physik
der Johannes Gutenberg-Universität Mainz

von
Jürgen Köble
geb. in Frankfurt/Main

Mainz, 2001
D 77

Tag der Einreichung: 21.12.2001
Tag der mündlichen Prüfung: 05.04.2002

Quenched Disorder
and
Magnetism
in
TiFe$_2$ Laves Phase Thin Films

Ph.D. thesis
by
Jürgen Köble

Mainz, Germany 2001

Meinen Eltern und meiner Frau Jutta.

Contents

List of Figures

List of Tables

Introduction

The first synthesis of Laves phase compounds and the identification of their crystal structure was achieved by Laves and Witte in 1935 [1]. The Laves phase crystal structure defines an effective way of space filling for a binary compound with the particular ratio of the atomic radii $r_1/r_2 \simeq 1.2$. Since then a multitude of Laves phase compounds and their physical properties were investigated. Recently interest was attracted to the $\mathrm{LFe_2}$-type compounds (L is usually a 3d- or 4f- element with a larger atomic radius than Fe) due to their diversity of different magnetic ground states in conjunction with newly developed methods of calculating the electronic bandstructure of these compounds. As a result of such calculations, the variability of the magnetic ground states in these $\mathrm{LFe_2}$ compounds was associated with the energetic near-degeneracy of different spin-structures [2–5]. Interestingly, this may also result in a strong dependence of the magnetic properties on the composition for structurally homogeneous off-stoichiometric compounds or compounds with substitution of a third kind of atoms. $\mathrm{TiFe_2}$ is a prominent representative for this sensitivity to compositional variation. It can be hoped that an accurate description of the composition-dependent magnetic properties of the complicated $\mathrm{TiFe_2}$ system may yield a more general understanding of the magnetism of the $\mathrm{LFe_2}$ compounds. As an introduction to the $\mathrm{TiFe_2}$ problem, which will be discussed in the present work, a brief overview of the historical development of the comprehension of this Laves phase compound is given in the following.

After the discovery of $\mathrm{TiFe_2}$, further studies on this compound started in 1954 by Elliot [6] and in the following years by Piegger, Nakamichi, Kocher and Wallace [7–10]. During their research differing conclusions concerning the magnetic long-range behavior were drawn. While Piegger et al. stated paramagnetism down to $T = 4\,\mathrm{K}$ for their samples, Kocher et al. found their samples to be unambiguously ferromagnetic. Wallace et al. realized the sensitive dependence of the magnetic properties on the preparation environment. They found antiferromagnetism in carefully prepared samples. Despite the preliminary nature of these results they still give an indication of the strong relationship of structural and magnetic properties in this compound. The first serious attempt to elucidate this relationship was made by Nakamichi. He showed that for $\mathrm{Ti}_x\mathrm{Fe}_{1-x}$ with $x \approx \frac{1}{3}$

a composition-dependent transition from ferromagnetism for Fe-rich samples to antiferromagnetism for Ti-rich samples takes place. However, the microscopic origin of this behavior remained unclear. Recent studies approached this problem by even more controlled sample preparation techniques, as well as by theoretical means based on spin-resolved advanced band structure calculations. As a result, magnetic clustering was suggested to be responsible for the different magnetic states as a function of composition. The still lacking phase purity of the samples prepared so far and the incomplete microscopic understanding of the antiferromagnetic to ferromagnetic transition suggests to attempt an alternative approach to the $\mathrm{TiFe_2}$ problem. This is the subject of the present work.

Molecular beam epitaxy was chosen to prepare polycrystalline and epitaxial thin films in the C14 stability range of $\mathrm{Ti}_x\mathrm{Fe}_{1-x}$. The aim was to investigate the magneto-structural interrelationships in this system as a function of x based on well-defined samples which allow to unambiguously distinguish between preparation-induced and intrinsic magnetic properties. This approach offers an alternative to earlier works on $\mathrm{TiFe_2}$ bulk samples which suffered from preparational problems due to impurity phase segregation [11]. Such bulk samples may only prepared in thermal equilibrium. With the epitaxial thin film preparation methods samples far from thermal equilibrium can be prepared and the segregation problem can be overcome. After a brief overview on Laves phase compounds in chapter 1, chapter 2 is devoted to the preparation process of the thin films employing molecular beam epitaxy. Polycrystalline (110)-textured samples and epitaxial (001)-oriented films were prepared in this work. In chapter 3 the results of the structural characterization of the films are presented. The standard methods used for this characterization include reflection high energy electron diffraction, scanning tunnelling microscopy, X-ray diffraction, Rutherford backscattering and energy dispersive X-ray spectroscopy. The magnetic characterization was performed by SQUID magnetometry. Additional data processing steps were required to distinguish between the sample signal and the external signal of the magnetometer. This is briefly illustrated in chapter 4. Further magnetization and magnetoresistivity measurements, as detailed in chapter 5, revealed an unidirectional magnetic anisotropy for the polycrystalline samples. In chapter 6 an analysis of the composition-induced transition between different magnetic ground states is performed for a series of epitaxial thin films. Many issues remained unsolved within this analysis. Therefor, a microscopic model with random quenched disorder based on the 3D Ising antiferromagnet is introduced in chapter 7 to gain further insight into these problems. Monte Carlo simulations were performed to establish the model's composition dependent magnetic properties in comparison with the experimental data. The work concludes with a summary and open questions in chapter 7.6.

Chapter 1

$\mathrm{Ti}_x\mathrm{Fe}_{1-x}$ in the C14 Laves phase stability range: a brief review

1.1 Laves phase compounds and their crystal structure

In 1935 F. Laves described for the first time a new type of intermetallic compounds commonly known as Laves phases [1] or Laves phase intermetallic compounds (LIC). The Laves phase crystal structures offer an efficient way of space filling for LS_2 (L: large atoms; S: small atoms) binary compounds with an ideal ratio of the atomic radii r_L:$r_S = \sqrt{\frac{3}{2}} \approx 1.2$. Three different crystal structures are realized: the cubic C15 (prototype: $MgCu_2$), the hexagonal C14 (prototype: $MgZn_2$) and, less common, the hexagonal C36 structure (prototype: $MgNi_2$). A comparison of the C14 and C15 structure is given in Fig. 1.1: the hexagonal C14 structure constitutes a hexagonal closed package with a sublattice stacking sequence of the form AB along the c-axis (space group 194 with $P6_3$/mmc symmetry) [12]. The L-atoms are placed on the (4f)-sites, and the Wyckoff sites (2a) and (6h) are occupied by the S-atoms. The cartesian coordinates of the corresponding positions are given in table 1.1.

	S(2a)		**S(6h)**						**L(4f)**			
	1	2	3	4	5	6	7	8	9	10	11	12
x	0	0	-x	-x	2x	-2x	x	x	1/2	1/3	2/3	2/3
y	0	0	-2x	x	x	-x	2x	-x	2/3	2/3	1/3	1/3
z	0	1/2	1/4	1/4	1/4	3/4	3/4	3/4	z	1/2-z	1/2+z	c-z

Table 1.1: The Cartesian coordinates of the atomic sites for the C14 structure. For the perfect structure z=1/16 and x=-1/6.

The cubic C15 structure is fcc closed packed with a stacking sequence ABC along the [111]-direction (space group 227 with $Fd\bar{3}m$ symmetry) [12]. In this case the unit cell contains the L-atoms on the (8a) sites and the S-atoms on the (16d) sites. The cartesian coordinates of the C15 structure are summarized in table 1.2.

	S(8a)		**S(16d)**			
	1	2	3	4	5	6
x	0	1/4	5/8	5/8	7/8	7/8
y	0	1/4	5/8	7/8	5/8	7/8
z	0	1/4	5/8	7/8	7/8	5/8

Table 1.2: The Cartesian coordinates of the atomic sites for the C15 structure.

The difference between both structures can easily be identified if one selects pairs of L-atoms along the c-axis of the C14 structure as a sublattice and compares these to the stacking of the corresponding pairs along the [111]-direction in the C15 structure. Both structures consist of S-atom tetrahedras and L-atoms fitting between them. Fig. 1.2 gives a perspective view to the coordination of the tetrahedras in the C14 structure (left) and a truncated view of the voids containing the L-atoms (right). The surface surrounding the voids which is bound by the next-neighbor S-atoms, is constructed by four hexagons and four triangles.

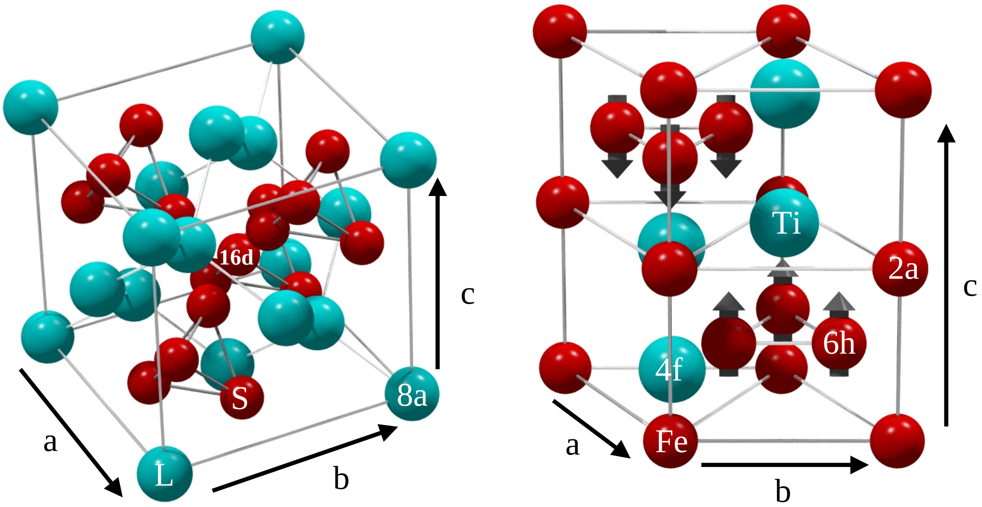

Figure 1.1: Crystallographic unit cell of the C15- (left) and the C14-Laves phase structure (right). The Wyckoff positions are representatively denoted on the respective sites. The lattice constants of the C14-structure of $TiFe_2$ are a=0.4785 nm and c=0.7790 nm. The magnetic configuration is indicated by arrows.

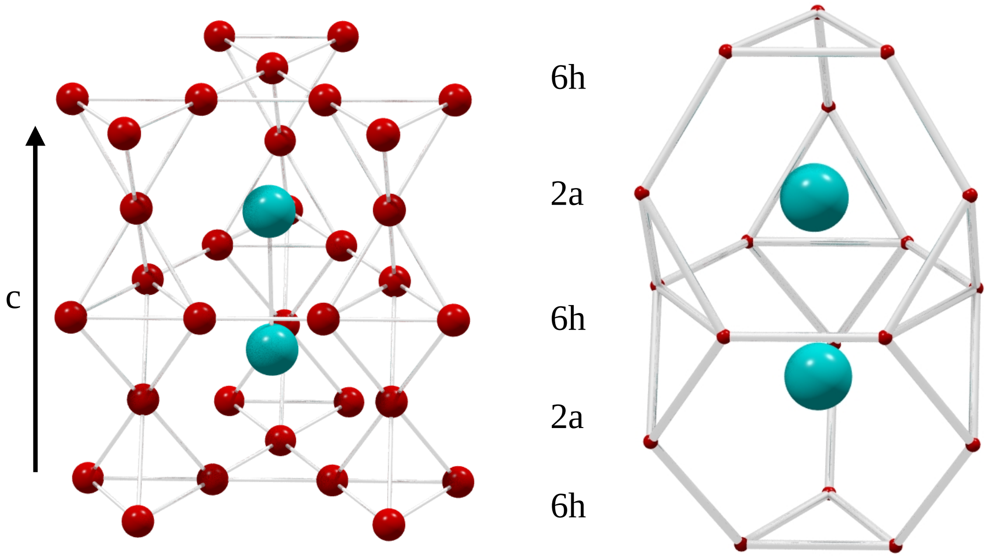

Figure 1.2: Left: alignment of the tetrahedras in the C14 structure. The small atoms form tetrahedras which share bases on the (6h) sites and tops on the (2a) sites (relative sizes of the atoms are not to scale). Right: the large atoms are placed between the tetrahedras. Only next-neighbor S atoms are shown for clarity.

The large radius L-atoms are either rare-earth or transition metals, the small radius S-atoms are simple metals or transition metals. A combinatorial overview of commonly known Laves phase compounds with their respective crystal structure is given in table 1.3.

Pseudobinary compounds do also form Laves phase structures: The large atom can be substituted by another atom of comparable size, as, for example, in the compounds $Sc_{1-x}Ti_xFe_2$ [14–16] and $Hf_{1-x}Ta_xFe_2$ [16,17].

Special interest in the Laves phase compounds stems from the extraordinary magnetic properties of the LFe_2-type compounds. For L=Y, Zr and the Lanthanides the C15 structure is found, while for L=Sc, Ti, Nb, Hf, Ta and W the C14 structure is preferred. All C15 compounds exhibit a ferromagnetic ground state [16]. The pronounced magnetic anisotropy and the large magnetoelastic constants of these compounds are of major importance with regard to possible applications. A rich spectra of magnetic states occurs for compounds with the C14 structure and their pseudobinary analogs. For several LFe_2 Laves phase compounds the electronic band structure was calculated with respect to the magnetic ground state [2–5,18–20]. Ferromagnetic, antiferromagnetic and paramagnetic ground states were found. As a result, the magnetic state and the preferred crystal structure strongly depend on the lattice constants and, thus, on the hybridization of the d-bands with the neighbored atoms.

L\S	Cr	Mn	Fe	Co	Ni	Mo	Tc	Ru	Rh
Sc	-	C14	C14	C15	-				
Ti	C15(C14)	C14	C14	C15	-				
Y	-	C15	C15	C15	C15	-	-	C14	C15
Zr	C15,C14	C14	C15	C15	-	C15	C14	C14	-
Nb	C15(C14)	C14	C14	C15	-				
Hf				C15+C14					
Ta				C14					
W				C14					
Ce				C15					
Tb				C15					
Dy				C15					

Table 1.3: The crystal structures of Laves phase compounds. $TiCr_2$ and $NbCr_2$ crystallize in the C15 structure at low temperatures and in the C14 structure at high temperatures [3,13].

1.2 Ti_xFe_{1-x} in the C14 stability range - an extraordinary intermetallic compound

1.2.1 Binary phase diagram

The present work focuses on the C14 Laves phase compound $TiFe_2$. The binary system Ti_xFe_{1-x} exhibits a relatively wide stability range for the C14 structure between x=0.276 and x=0.352 at $T \approx 1300\,°\mathrm{C}$ as depicted in Fig. 1.3 (x=0.285 and x=0.355 in [21]). The maximum of the liquidus line occurs at the LIC composition $x = \frac{1}{3}$ at T=1427 °C [22] where the C14 structure melts congruently. On the other hand, in a recent work the congruent melting point was found at x=0.35 and T=1415 °C [23]. Passing the phase boundary towards lower x, one enters a coexistence region of the C14 phase and α-iron. Crystallization in this region is eutectoid below T=1289 °C. For higher x a coexistence region of the C14 phase and the at T=1317 °C peritectically forming TiFe with CsCl structure adjoins the C14 stability range. The range of homogeneity and the congruent melting point of the C14 structure seem to depend substantially on the preparation method (e.g. annealing time etc.) [23,11,21,22]. However, the available data are expected to give a good starting point for the thin film preparation discussed in this work.

1.2.2 Magnetic unit cell

After the discovery of $TiFe_2$ by Laves [1], first measurements of the magnetic behavior were performed by Elliot, Piegger et al. and Nakamichi [6–8] by means

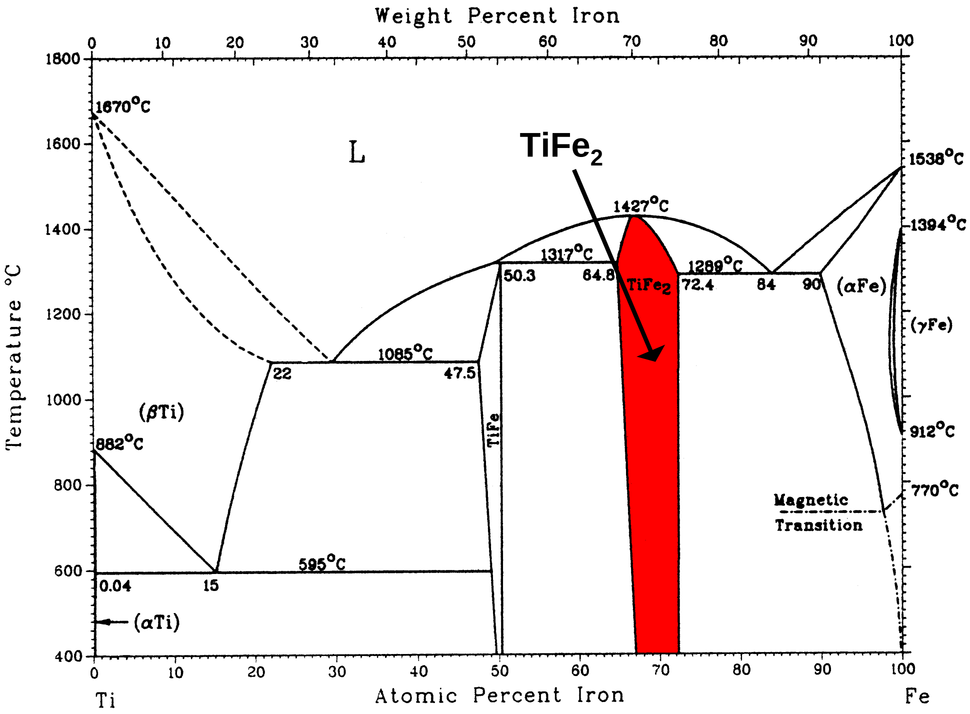

Figure 1.3: Binary phase diagram for the alloy $Ti_{1-x}Fe_x$ [22].

of conventional magnetization measurement methods, neutron diffraction and Mößbauer spectroscopy [9,10]. Controversial results concerning the magnetic state (ferromagnetic, antiferromagnetic or even exchange enhanced paramagnetic) were obtained, indicating the difficulties in preparation and the sensitive magnetic behavior of the LIC. The first complete description of the size and the alignment of the magnetic moments on the different symmetry sites within the unit cell were given in 1992 by Brown et al. [24]. The configuration corresponds to an anisotropic collinear antiferromagnet as shown in Fig. 1.1: the magnetic moments are stabilized on the Fe(6h) sites and are aligned parallel to the c-axis in a staggered fashion; the magnetic moment amounts to $|\vec{m}_{6h}| = 1.4\mu_B$ at T=4 K [24]. The molecular field on the Fe(2a) sites cancels due to site symmetry. Thus, no ordered moment on these sites is found for the stoichiometric compound. In off-stoichiometric compounds the excess atoms substitute on antisites. In this case, the symmetry is disturbed and non-zero magnetic moments are found on the Fe(2a)- and the Fe-substituted Ti(4f)-sites [25](see next section).

1.2.3 Calculations, experiments and open questions

The binary compound Ti_xFe_{1-x} in the C14 stability range exhibits various magnetic properties that strongly depend on the site occupation within the unit-cell and the interatomic distances. Calculations have shown that this diversity has its origin in a magnetic instability which occurs about the stoichiometric point [4,5]. At this point the antiferromagnetic (AF) and ferromagnetic (FM) state are nearly energetically degenerate, with the FM state being situated a few meV above [4,5]. The calculations by Asano and Ishida [4] predict a transition from an AF to a FM ground state with increasing lattice volume. This does not correspond to the experimental results, probably caused by the low accuracy of the underlying linear muffin tin orbital (LMTO) method. Thus, these calculations will not be considered in the following discussion. As can be seen in Fig. 1.4, Hoffmann et al. calculated the dependence of the total energy on the lattice constants by first principles density functional calculations for the C14 and the (hypothetical) C15 structure [5]. All magnetic states of the C15 structure are at a significantly higher energy than the corresponding states of C14 structure. Consequently, the C15 structure is not formed. The calculations for the C14 structure exhibit, beside a non-magnetic state at higher energy, a FM state and an AF state. While the FM state has its minimum energy for small lattice constants, the absolute minimum is found for the AF state at slightly larger lattice constants. The energy of the AF state is lowest in energy for large lattice constants, indicating a preferential AF ground state for large cell volumes. For small lattice constants the AF and FM state are, within the accuracy of the calculations, virtually degenerate.

In the off-stoichiometric case the magnetic state can also be predicted by the calculations for the stoichiometric case if it is assumed that the valences of the atoms in the neighborhood of a substitution site are not altered. In this case, the electronic bandstructure is comparable to that of the stoichiometric compound. In various experiments on bulk samples a composition-dependent transition from AF behavior for $x \geq \frac{1}{3}$ to FM behavior for $x < \frac{1}{3}$ was observed [8,11,25,26]. Wassermann et al. [11] prepared a series of samples about the LIC composition and measured the dependence of the magnetization on the temperature while applying a magnetic field of 1 T. The isothermal magnetic susceptibility reflects a transition from predominantly AF to predominantly FM behavior close to the stoichiometric point. For significantly off-stoichiometric alloys a mixed AF/FM phase behavior was found. According to a model by Wassermann et al., for off-stoichiometric compounds the excess atoms occupy antisites [11]. This was proved for the Fe substitution on Ti(4f) sites by X-ray and neutron diffraction [21] as well as by Mößbauer spectroscopy [25,26]. No direct experimental prove for the substitution on Fe sites by Ti atoms is available, but Brückner [21] and Wassermann [11] assumed this in their work. Wassermann et al. [11] proposed that by varying the composition the cell volume shrinks for Fe substitution (atomic radius r_{Fe}=1.241 nm) on Ti-sites or increases for Ti substitution (atomic radius r_{Ti}=1.448 nm) on Fe-sites. According to Fig. 1.4 this has a direct impact on the magnetic properties. In Mößbauer spectroscopy experiments it was found that,

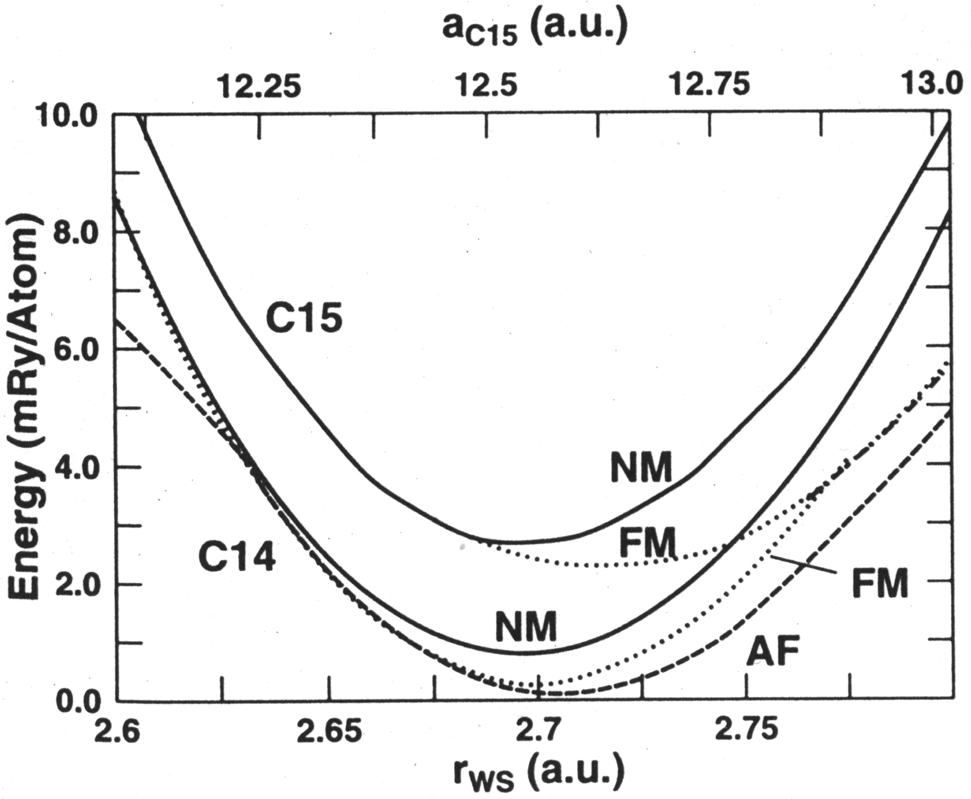

Figure 1.4: Total energy dependence of $TiFe_2$ on the lattice constants (here: radius of the Wigner-Seitz cell). The C15 structure is not formed due to its higher energy [5].

as the number of Ti-sites occupied by Fe-atoms increases, the symmetry within the unit-cell is disturbed and ordered magnetic moments on the initially paramagnetic Fe(2a)-sites appear [25,26]. Wassermann et al. assume that small (for small deviations from stoichiometry superparamagnetic) iron clusters are formed and the spin-structure may be no longer collinear. If the number of the small clusters increases, a percolation threshold is passed and a long-range ordered FM contribution to the AF susceptibility can be detected [11]. As the Ti-atoms are paramagnetic, for $x > \frac{1}{3}$, but still close to the LIC composition, the molecular field on the iron sites is not significantly distorted and the overall AF-matrix is retained. For higher x the distortion is not negligible anymore and FM-clusters are formed again [11]. The formation of a FM state from an AF state by the substitution of a small magnetic atom by a larger non-magnetic atom was examined by Nishihara et al. in the pseudobinary system $Sc_{1-x}Ti_xFe_2$ for x close to one [14–17]. Their results support this picture. Wassermann et al. determined the critical temperatures from their susceptibility data and derived a magnetic phase diagram which is formed of AF, FM and mixed AF/FM regions [11]. This topic will be treated in detail in chapter 6, in which a magnetic phase diagram for epitaxial thin films at low aligning fields is established.

In addition to the mixed magnetic phase behavior found in the experimental magnetic susceptibility, first principles density functional calculations exhibited anharmonicities in the projection of the total energy to the moment-volume plane (binding surface) at $T = 0\,\mathrm{K}$ [5]. These anharmonicities occur as rather sharp transitions from distinct moment-volume states to different moment-volume states which differ only a few meV in energy [27,28]. In general, these moment-volume instabilities lead to a phenomenon called the Invar effect which was found in several ferromagnetic or antiferromagnetic alloys. Its name is derived from the transition metal alloy Invar ($Fe_{0.64}Ni_{0.36}$) in which this effect was first observed [29]. Indicative of the Invar effect is an almost constant thermal expansion coefficient $\alpha(T)$ in a wide temperature range. The effect vanishes for $T \gg T_\mathrm{C}$ [30]. During warm-up from $T = 0\,\mathrm{K}$ the thermal lattice expansion is at least partially compensated by the increasing density of excitations into other moment-volume states. For Invar alloys excitations from the high-spin (HS) state at the equilibrium volume to the low-spin (LS) state at reduced volume generate the Invar effect. $\alpha(T)$ is reduced with respect to the expected Grüneisen behavior for non-magnetic alloys [31]. If the equilibrium state is the low-volume LS state an anti-Invar effect with an increased thermal expansion coefficient $\alpha(T)$ is found [32].

The AF and FM binding surfaces of the Fe(6h)-atoms calculated in [5] show for reduced volume a LS-to-NM (NM: non-magnetic) state transition which may generate an Invar-effect. For the FM binding surface at increased volume a LS-to-HS transition occurs, indicating an anti-Invar behavior [33]. The samples analyzed in [33] are not expected to completely comply with these predictions due to their off-stoichiometric composition with a probably non-linear spin structure. Nevertheless, an Invar-effect was found for samples composed in a compositional range about the stoichiometric LIC. Additionally, a transition of a ferromagnetic to an antiferromagnetic Invar-effect was observed, corresponding to the preferential magnetic ordering of the samples (see Fig. 1.5). This transition occurs within a small range $\Delta x = 0.045$ [33]. A martensitic transition, which is typically observed for Invar alloys, has not yet been observed for $TiFe_2$.

Crystalline phase purity, elemental purity and homogeneity of the samples is a crucial requirement for an accurate investigation of the magnetic properties. The strong dependence on the lattice structure and the influence of magnetic impurities, as induced e.g. by segregation, must not be disregarded. The preparation of single crystals with high phase purity appears to be non-trivial. In early experiments, crucibles were used for the melting process. Due to the high reactivity with standard crucible materials at least small amounts of the crucible are dissolved in the samples [23,21]. The position of the congruent melting point

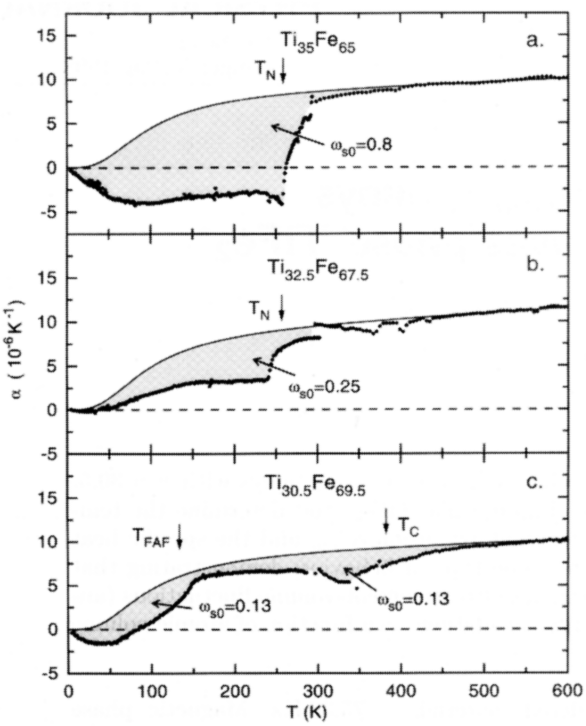

Figure 1.5: Thermal expansion coefficient for bulk Ti_xFe_{1-x} samples with $x = 0.35$ (top), $x = 0.325$ (middle) and $x = 0.305$ (bottom). The full curves are Grüneisen-fits for $T \gg T_C$ which disregard effects of magnetism. The Debye-temperature needed for the Grüneisen fits was determined by specific heat measurements. The shaded areas correspond to the respective spontaneous volume magnetostriction ω_{SO} [33].

also seems to be very sensitive to the composition as determined by differential thermal analysis [23]. Even for the supposedly best crystallization method, the Czochralski technique with levitating melt, cracks frequently occur [23]. Thus, only small single crystals could be prepared so far. These still seem to contain a small amount of phase separated iron, indicated by a clear signature at the Curie temperature of Fe in temperature-dependent susceptibility measurements [11]. Interestingly, completely amorphous alloys can be prepared by mechanical alloying of a mixture of Fe and Ti in stoichiometric proportions as is indicated by the chemical short range order found in neutron-diffraction experiments on such samples [34].

A quite different approach to these preparational problems is given by epitaxial thin film growth which is described in the following chapter. So far, only amorphous films have been prepared [35,36].

Chapter 2

Preparation of $\mathrm{Ti}_x\mathrm{Fe}_{1-x}$ thin films

In contradistinction to crystal growth from the melt thin film growth methods, such as the molecular beam epitaxy (MBE) deposition technique or DC sputtering, offer the possibility to prepare single- or polycrystalline thin films far from equilibrium. In case of the single crystalline films this might help to mitigate the problem of iron phase-separation, as mentioned in section 1.2.3. In-situ characterization methods, as used in MBE, allow for an additional monitoring of the growth process. Moreover, epitaxial strain and clamping, partly induced by the cooling process after deposition, will exert their influence on the instable magnetic ground state of TiFe_2. It thus offers an additional means to alter the magnetic properties. Alternative growth directions can be achieved by changing the templates' surface symmetry or, as will be discussed in the following sections, by varying the substrate temperature during deposition.

2.1 Sputtering

A fast and cheap method for preparing thin films is given by DC sputtering. In contradistinction to ultra high vacuum (UHV) condition in MBE growth, sputtering may be performed at much higher pressure which allows for a fast sample change. The increased kinetic energy of the sputtered atoms in the eV range increases the surface mobility of the adatoms and allows for lower substrate temperatures. $\mathrm{Ti}_x\mathrm{Fe}_{1-x}$ samples were prepared by the dual-facing sputtering method which has been applied successfully to grow other binary compounds (for example UPt_3 [37]): the sample is rotated between an Fe and a Ti target. The facing time and the sputtering rate r_{sp} were adjusted to deposit only a fraction of the TiFe_2 unit cell height corresponding to the inter-planar distance of adjacent Fe layers ($d \approx 0.2\,\mathrm{nm}$) during each cycle. A crystal growth may then be induced due to thermally activated surface diffusion to equilibrium sites at the topmost atomic layers.

All samples were prepared using Ar as sputtering gas. $Al_2O_3(001)$ substrates were attached to a heater by silver paint or a ceramic glue (see next section). The composition was varied about the stoichiometric point as determined by energy dispersive X-ray spectroscopy (EDX). Additionally, different substrate temperatures T_{sub} between 770 K and 940 K were chosen. As a result, no crystalline $TiFe_2$ was detected in the films which would have been indicated by Bragg reflections in X-ray diffractometry patterns. Samples prepared at $T_{\text{sub}} = 940\,\text{K}$ and growth rates in the range $0.02 < r_{\text{sp}} < 0.1\,\text{nm/s}$ exhibit, in contradistinction to samples prepared by molecular beam epitaxy under comparable conditions, no $TiFe_2$ phase at all. This may be caused by the different high energy kinetics or the higher impurity concentration of the deposited atoms during the sputter process, influencing the sensitive growth process of $TiFe_2$. No further evaluation of the sputtering of Ti_xFe_{1-x} was performed within this work.

2.2 Molecular beam epitaxy

Molecular beam epitaxy is the preferred method for epitaxial thin film preparation if a detailed monitoring of the deposition process is necessary. As seen in section 2.1, the epitaxial growth of $TiFe_2$ cannot be easily achieved by DC sputtering. Consequently, the growth of epitaxial Ti_xFe_{1-x} in the C14 stability range was attempted by MBE. The instrumental configuration and the deposition procedure are described in this section.

2.2.1 Varian Picotorr 450 MBE system

Most of the samples described in this work were prepared using a Varian Picotorr 450 MBE system (see Fig. 2.1) with an in-situ reflection high energy electron diffraction (RHEED) analysis facility operated at an acceleration voltage of 9 keV and an incident angle of 1.6 °. The system is evacuated via a load-lock chamber by a roughing pump and a turbo molecular pump. Furthermore, an ion-getter pump combined with a titanium sublimator is situated in the main preparation chamber which allows for UHV conditions. The stainless steel sample holder can be transferred between the load-lock chamber, the main preparation chamber, a sputtering chamber and a post-deposition analysis chamber. The latter was not used in this work. A more complete description of the system can be found in [38]. The temperature was measured by a W/W-Re thermocouple attached to the substrate heater and by a pyrometer set to the emissivity $\epsilon = 0.35$ of stainless steel. The deposition was accomplished by co-evaporation of Fe and Ti from electron beam evaporators. The growth rate was measured and stabilized by a quartz crystal rate monitor and controller.

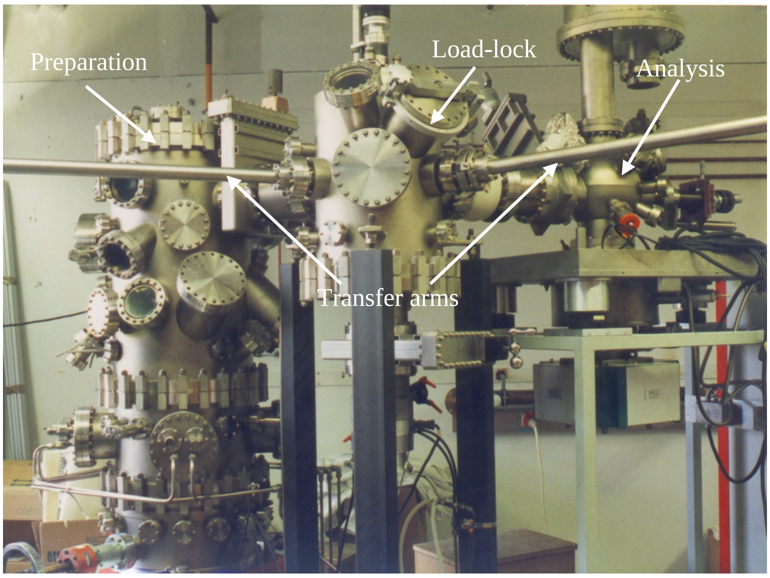

Figure 2.1: The Varian Picotorr 450 MBE system. The sputter chamber is not shown as it was mounted after the picture was taken.

2.2.2 Omicron custom-designed MBE system

Several samples were prepared in a custom designed MBE system assembled by Omicron Vacuum Physics. A comparison of the structural properties of these films with the films prepared in the Varian system allows to exclude hidden parameters in the preparation process, e.g. residual gas concentration or evaporation method. Additionally, an UHV scanning tunnelling microscopy (STM) facility attached to the system was used to examine the surface structure. The system (see Fig. 2.2) is divided into separate chambers: a load-lock chamber is pumped by a roughing pump and a turbo molecular pump. The samples, which are mounted on stainless steel or molybdenum sample plates by silver paint, are stored in a rotatable sample holder. This sample holder can pick up six sample plates which can be transferred by a transfer arm, situated in the central distribution chamber (R2P2), to a heating station which is also mounted in the load-lock chamber. In the heating station the samples can be degassed by either radiation heating or direct heating. The load-lock chamber is separated from the distribution chamber by a gate valve. The distribution chamber can be evacuated by the pumps attached to the load-lock chamber while the gate valve is open. An additional ion-getter pump with titanium sublimator allows for UHV conditions. Further chambers attached to the distribution chamber are the MBE chamber

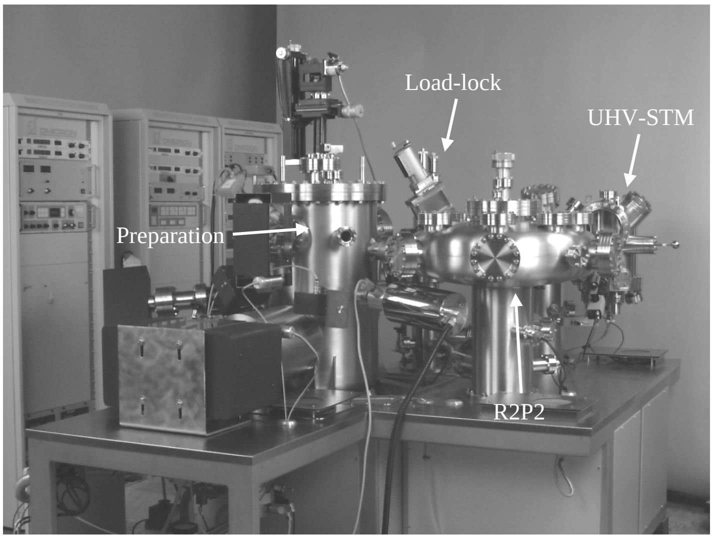

Figure 2.2: The custom-designed MBE system (assembled by Omicron Vacuum Physics).

and an analysis chamber. The thin films are prepared in the MBE chamber which is divided into two parts by a surrounding cooling shroud. The shroud may be cooled by liquid nitrogen for an additional decrease of pressure by adsorption of residual gas. The transfer opening of the shroud is closed by a linear shutter. The upper part is used for low energy electron diffraction (LEED) analysis and the lower part for the deposition. The evacuation is performed by a roughing pump, turbo molecular pump and two ion-getter pumps with titanium sublimator. Within the MBE chamber the sample plates are transferred by a manipulator with five different degrees of freedom: linear up and down, x-y position, azimuth and inclination. The samples can be heated either by radiation or direct heating. Evaporation of different materials can be achieved by a multipocket electron beam evaporator (MDC EV-FMP-10RUHV) and high-temperature (MBE-Komponenten HTEZ-40) or low-temperature effusion cells. The growth rate is measured by a cross-beam quadrupol mass spectrometer (Hiden HAL/3F 301) or by a quartz crystal rate monitor (Intellimetrics IL150). A RHEED analysis unit (STAIB Instrumente RH20) allows for additional monitoring of the growth process. The analysis chamber is equipped with a heater on a long transfer manipulator which is identical to the heaters described above. A variable temperature STM (Omicron VT-STM RH) is located in an attached chamber. A combination of roughing pump, turbo molecular pump and ion-getter pump with titanium sublimator generates UHV conditions. The models of the pumps employed for the evacuation of the UHV system are EDWARDS RV3 (roughing pumps), Pfeiffer TMU 260 (turbo molecular pumps), Varian Vac Ion Plus (ion-getter pumps) and Varian VG-ZST22 (titanium sublimation pumps).

2.2.3 Pre-processing of the substrate

The proper choice of the substrate is crucial for an epitaxial growth of thin films. $Al_2O_3(001)$ with an a-axis length $a = 0.4758\,nm$ (misfit to $TiFe_2$ $\eta = \{a_{sub} - a_{film}\}/a_{film} = -0.6\,\%$) [12] and its pseudo-hexagonal symmetry provides an excellent substrate for epitaxial c-axis growth of the hexagonal $TiFe_2$ compound (see Fig. 2.3). Commercially available $Al_2O_3(001)$ single-side epitaxially polished substrates (Crystec Kristalltechnologie) were used throughout this work. The substrates were delivered with a polymer protection layer on the polished surface. Employing a diamond wire saw the substrates were cut to the desired size with de-ionized water as a coolant. To remove the polymer layer the substrates were cleaned for 8 minutes in acetone and twice for 2 minutes in isopropyl alcohol employing an ultrasound cleaning bath in either case, as recommended by the manufacturer. A surface analysis using an optical microscope exhibited no stains or particle remainders within the resolution of the microscope. The substrates were attached to a stainless steel sample plate by silver paint. Two samples were prepared in parallel ($2.5x2.5\,mm^2$, $4.5x4.5\,mm^2$) to allow for a homogeneity check. The crystalline properties were compared for a selected set of sample pairs and were found to be virtually identical. The small samples were used for magnetization measurements as described in chapter 6.

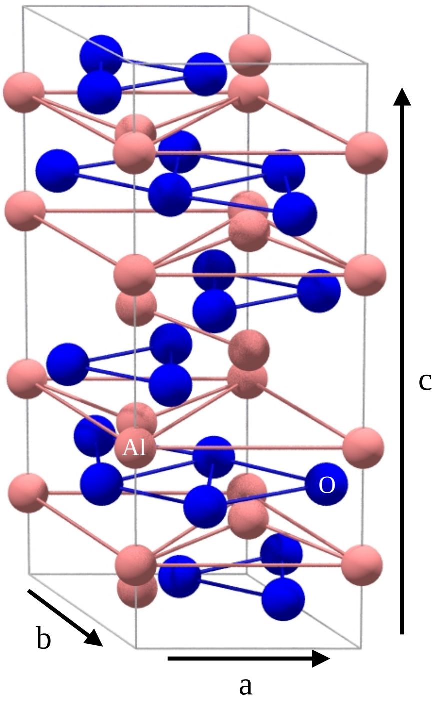

Figure 2.3: Crystallographic unit cell of Al_2O_3 with Al atoms (light) and O atoms (dark). The overall symmetry is rhombohedral. The Al sublattice is hexagonal.

2.2.4 Deposition process

After evacuation to $p \approx 10^{-7}$ mbar the samples prepared in the Varian MBE system were transferred from the load-lock chamber to the preparation chamber. Before deposition all substrates were degassed and annealed in-situ for 1 h at $T = 1100$ K to improve the surface morphology [39]. Subsequently, the substrates were cooled to the deposition temperature T_{sub}. The deposition was accomplished by co-evaporation of Fe (purity 99.95 %) and Ti (purity 99.99 %) (both in molybdenum liners) from electron beam evaporators at a base pressure below 10^{-9} mbar. The acceleration voltage of the evaporators was fixed at U_{acc} =4 kV. Fe was evaporated at a power $P \cong 120$ W and Ti at $P \cong 280$ W. The temperature was measured as described in section 2.2.1. All temperatures given in this work relate to the temperatures obtained by the pyrometer. No additional calibration of the pyrometer was performed. After the deposition the samples were cooled to 400 K within 1 h. Next, they were transferred in-situ to the sputtering chamber and sputter-coated with an aluminum anti-oxidation barrier of 20 to 30 nm thickness as determined by low-angle X-ray reflectometry. According to the binary alloy phase diagrams [22] any reaction between Al, Fe and Ti at this temperature can be excluded. A workflow diagram of the standard procedure including preparation and structural characterization is shown in Fig. 2.4.

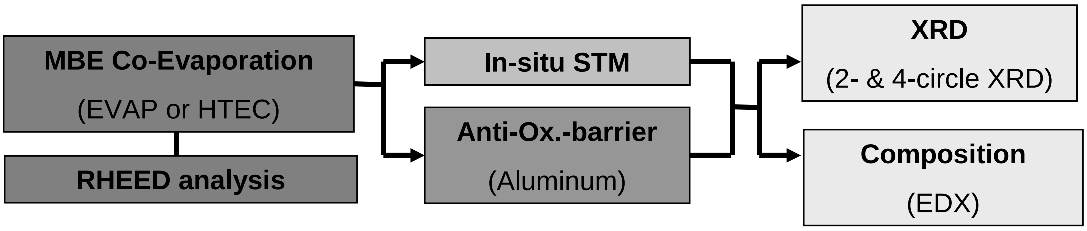

Figure 2.4: Standard preparation and structural characterization workflow as applied to the Ti_xFe_{1-x} samples.

Samples prepared in the Omicron system were degassed in the load-lock chamber by quickly heating to $T \approx 600$ K and cool down to room temperature. After the transfer to the preparation chamber the substrates were annealed for 1 h at $T = 1100$ K (see above) and cooled to T_{sub}. In this system Ti was evaporated with a liner-free electron beam evaporator and Fe from a high temperature effusion cell (HTEC) with a BeO crucible at $T_{\text{cru}} = 1820$ K. All other parameters were chosen identical to the process described above, except for the deposition of the aluminum protection layer which was left out.

In either case the overall growth rate of the Ti_xFe_{1-x} layer was held at 0.02-0.03 nm/s. All samples remain stable under ambient conditions which was verified by a long-time comparison of X-ray diffraction (XRD) and magnetization measurements. The samples without aluminum coating exhibit an 2 to 3 nm oxidation layer as indicated by low-angle X-ray reflectometry.

Chapter 3

Structural characterization

A detailed structural characterization of the $\mathrm{Ti}_x\mathrm{Fe}_{1-x}$ samples is important for an understanding of the magnetic properties due to their strong dependence on the composition and the sublattice order, as described in chapter 1. Consequently, several different, partially complementary characterization methods were applied to the films. These methods include RHEED, XRD, STM, EDX and Rutherford backscattering spectroscopy (RBS). The results of the structural characterization are presented in this chapter.

3.1 Polycrystalline (110)-textured thin films

Below the epitaxial temperature T_{epi}, which amounts to $T_{\mathrm{epi}} = 825\,\mathrm{K}$ as will be described in section 3.2, only polycrystallline textured growth was observed. Due to the reduced surface diffusion, the hexagonal equilibrium sites on the substrate surface are not periodically occupied and the epitaxial relation to the substrate is not developed. Instead, seed grains of different orientations and compositions are formed, which do not perfectly adopt the symmetry of the substrate, and grow as polycrystalline parts of the thin film. Thus, differently textured polycrystalline films of $\mathrm{Ti}_x\mathrm{Fe}_{1-x}$ in various proportions of the constituents are formed for $T_{\mathrm{sub}} < T_{\mathrm{epi}}$. Fe(110), TiFe(110), TiFe_2(110) and TiFe_2(001) texture with varying proportions were found as indicated by the relative reflection intensities in the XRD patterns. The dependence of the different polycrystalline growth modes on the temperature and the composition was not studied in detail. Representatively, two samples were chosen for which the magnetic properties can be associated non-ambiguously with the structure.

The samples were prepared in the Omicron MBE system according to conditions described in section 2.2.3 and 2.2.4. The thin films were deposited at temperatures $T_{\mathrm{sub}} \cong 770\,\mathrm{K}$. The X-ray characterization was performed with a conventional Philips X-Pert MPD 2-circle diffractometer with Cu-K_α radiation in Bragg-Brentano geometry, and the stoichiometry was verified by EDX. Fig. 3.1 shows a longitudinal X-ray scan of a $Ti_{0.25}Fe_{0.75}$ thin film sample mainly consisting of Fe(110) with smaller contributions of $TiFe_2(110)$ and $TiFe_2(004)$. The width of transverse scans of these reflections range from 0.2 ° to 0.4 °, but no resolution limited narrow epitaxial component was found. This indicates polycrystalline textured growth. Further investigations by 4-circle XRD would have been necessary to decide if the grains were aligned isotropically. However, the low intensity of the reflections in the 2-circle diffractometer indicated a too low intensity for accurate 4-circle XRD measurements. SQUID magnetization measurements revealed ferromagnetism dominated by the Fe(110) component.

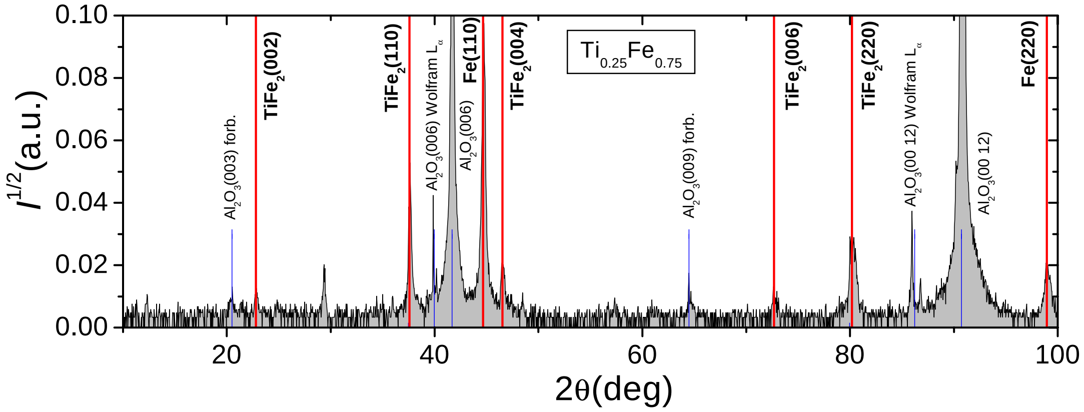

Figure 3.1: Longitudinal scan of a polycrystalline film with $x = 0.25$ deposited at $T_{\mathrm{sub}} \cong 770\,\mathrm{K}$.

Fig. 3.2 depicts XRD scans of a $Ti_{0.32}Fe_{0.68}$ thin film sample. The longitudinal measurement (top) exhibits (110)-textured $TiFe_2$ and TiFe(110) as a minor impurity phase, but no Fe(110) contributions. The integrated scattering intensities of the reflections indicate a ratio of $TiFe_2(110)$:TiFe(110) of about 10:1 [40]. In this case, the magnetic response of the sample is mainly due to $TiFe_2(110)$ since ordered TiFe is paramagnetic [41,42]. Detailed temperature- and field-dependent magnetization measurements were only performed on this sample (see chapter 5). Similar to the mainly Fe(110) textured sample, transverse scans of the $TiFe_2(110)$ and TiFe(110) reflections (see insets) show no epitaxial component, but a rather broad mosaic-like profile with a full width at half maximum (FWHM) larger than 1 °. This again indicates polycrystalline textured growth due to the lacking symmetry adaption to the underlying substrate.

As determined from low-angle diffraction the overall thickness is 108 nm with a topmost 4 nm thick oxide layer, indicated by the long-wavelength component Λ_2 (see Fig. 3.3). The rms roughness does not exceed 1 nm. The thickness of the films was determined by a Parratt analysis [43] implemented in the software package GIXA [44].

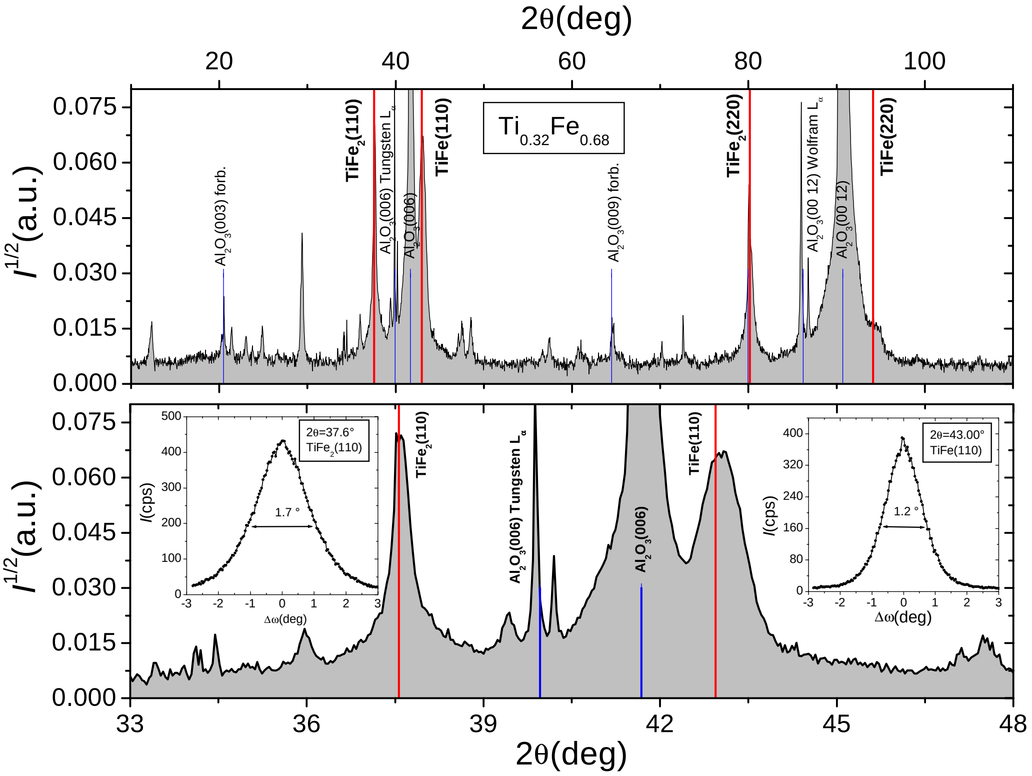

Figure 3.2: XRD scans of a polycrystalline film with $x = 0.32$ deposited at $T_{\text{sub}} \cong 770\,\text{K}$. Top: longitudinal scan. The non-indexed peaks are not due to the thin film. The intensity is normalized to the $Al_2O_3(006)$ reflection to facilitate comparison of the data. Left: expansion of the (110) reflection range. The insets show the transverse scans of the $TiFe_2(110)$ and the TiFe(110) reflection.

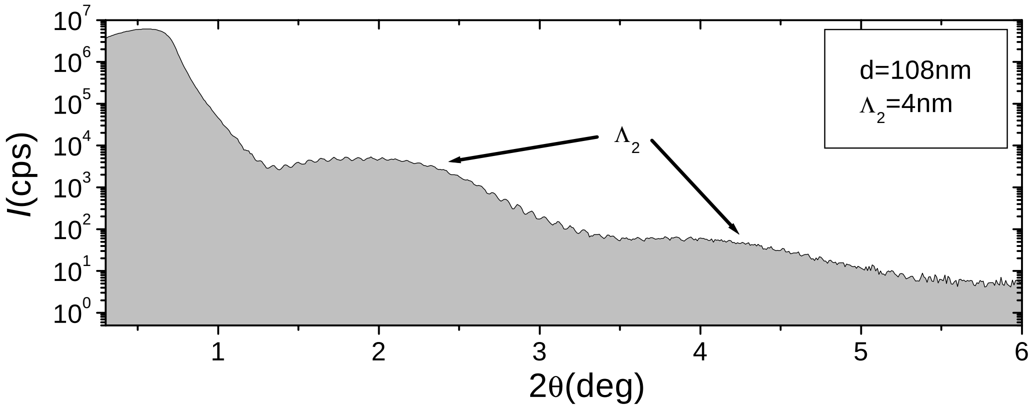

Figure 3.3: Low-angle reflectometric scan with a superposition of oscillations due to the film thickness and the oxidation layer (Λ_2).

3.2 Epitaxial (00l)-grown thin films

The present work focuses on epitaxial (00l)-grown thin films. The presented results extend the examined materials base of polycrystalline and small single crystalline bulk samples [7–9,23,13,21,24,25,34] and amorphous films [35,36]. In section 3.2.1 the determination of the composition is described. In section 3.2.2 the conditions for epitaxial growth and the influence of the substrate temperature are discussed. Next, RHEED patterns of selected samples taken during the deposition process and their interpretation are presented. In section 3.2.5 a comparison of the lattice constants of the films as a function of the composition with the results obtained for bulk samples is made. Finally, STM images are shown which were taken directly after growth employing an UHV-STM.

3.2.1 Determination of the composition

The pronounced sensitivity of the magnetic properties of $\mathrm{Ti}_x\mathrm{Fe}_{1-x}$ in the C14 stability range to the composition has been discussed previously (see section 1.2). A sufficient relative and absolute accuracy in the determination of the composition was achieved by EDX (spot-size $\Delta A = 30\,\mu\mathrm{m}^2$) in a Jeol JSM-6300F scanning electron microscope (SEM). For all samples the acceleration voltage was set to 20 kV. The ZAF (nucleus charge **Z**, **a**bsorption and **f**luorescence) corrections and integrations of the spectra were performed by the EDX analysis software SEMQuant [45]. As can be seen in a typical spectra in Fig. 3.4, an accurate and reproducible determination of the composition by EDX was possible because the

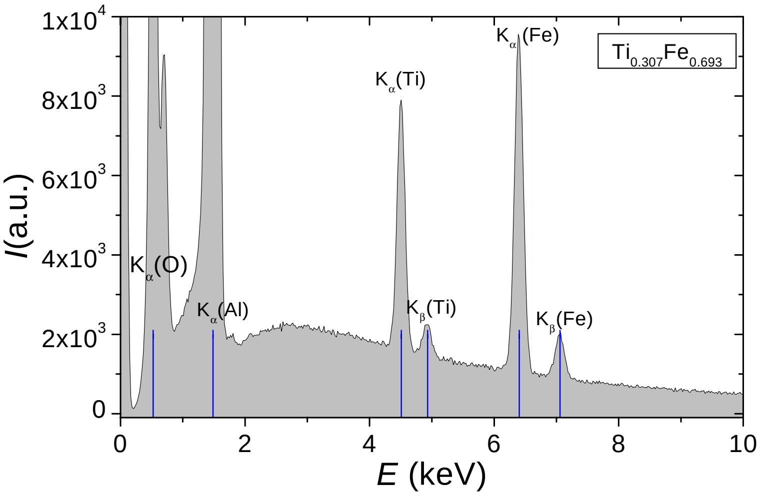

Figure 3.4: Typical EDX spectra of a thin film with $x = 0.31$. The positions of the corresponding fluorescence lines of the film and the substrate are marked.

$K_{\alpha/\beta}$ fluorescence lines of Ti and Fe do not overlap and are located at sufficiently high energy. EDX spectra, taken from two different locations of the samples, were found to be virtually identical within the error limits.

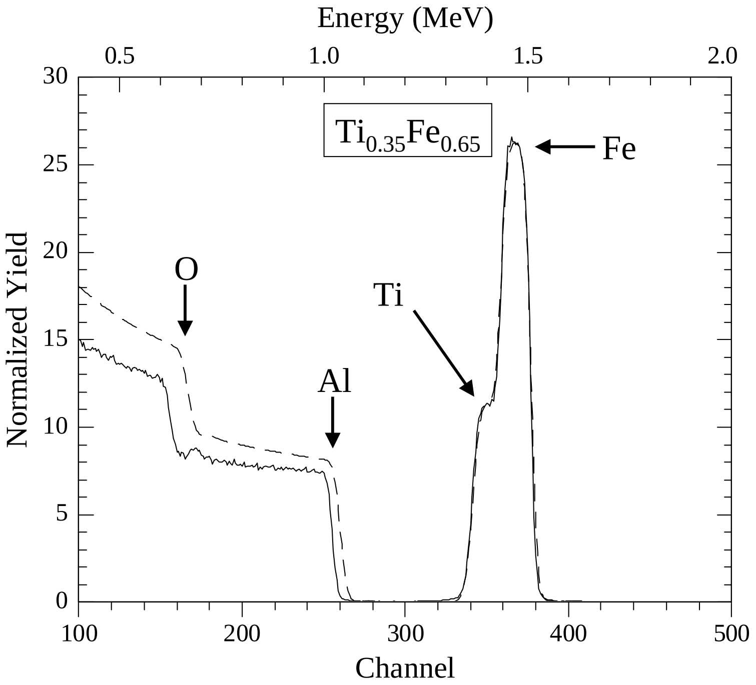

Figure 3.5: RBS spectra (solid) of a thin film with composition $Ti_{0.33}Fe_{0.67}$ as determined by EDX. The simulation (dashed curve) coincides with the measurement in the Ti/Fe energy range allowing for an accurate calibration. The input composition for the simulation was $Ti_{0.35}Fe_{0.65}$.

To check for the inherent systematic errors due to electron backscattering from the substrate the EDX spectra were calibrated against an RBS measurement ($^4He^+$ at 2 MeV) which was performed at the FZ Karlsruhe [46]. The spectra was simulated employing the RBS simulation software RUMP [47] (see Fig. 3.5). The intensities of the Al and O backscattering could not be simulated properly, but the ratio of Fe and Ti in the film could be deduced accurately. The deviations of the simulation from the measurement of the sample with $x = 0.33$, as determined by EDX, were lowest for $x_{\mathrm{sim}} = 0.35$. Since the EDX results differ only slightly from the RBS results, the nominal compositions determined by EDX are used in this work. All uncertainties given in the average composition are the statistical errors of the EDX analysis and are typically less than 1 %.

3.2.2 Epitaxial growth and temperature

The hexagonal (001) surface of the Al_2O_3 substrate induces epitaxial $(00l)$-oriented growth of the C14 Laves phase above the epitaxial temperature T_{epi} (see below). This was verified for a selected $Ti_{0.36}Fe_{0.64}$ sample by Φ-scans in a 4-circle diffractometer using Cu-K_α radiation [48]. As can be seen in Fig. 3.6 the reflections of the {112} planes of the film coincide with the respective {112} reflections of the substrate. Thus, the respective in-plane directions of Ti_xFe_{1-x} in the C14 stability range and Al_2O_3 are collinear. This was then assumed to be the case for all samples exhibiting a narrow epitaxial component in the rocking curve (see below).

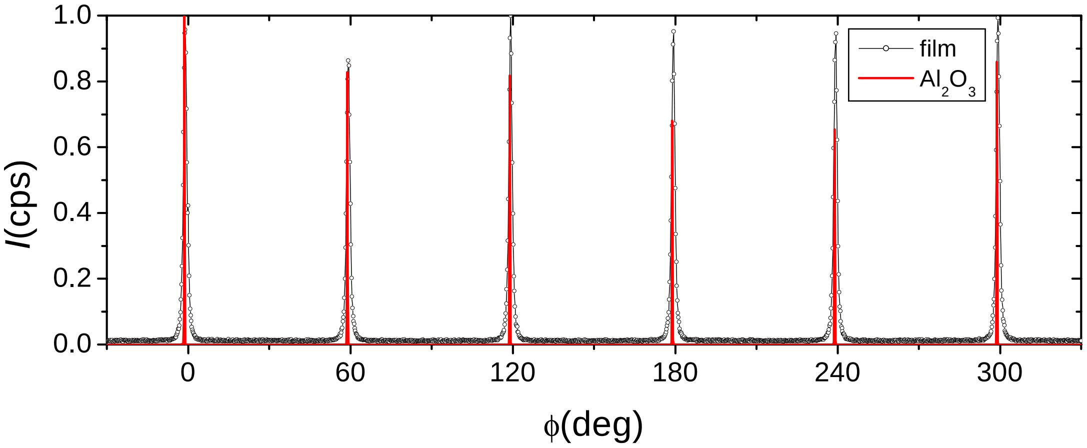

Figure 3.6: Φ-scans of {112} planes in a 4-circle diffractometer [48] proving the epitaxial relation between the $Ti_{0.36}Fe_{0.64}$ thin film (circles) and the Al_2O_3 substrate (vertical lines).

Additionally, the crystalline in-plane order was verified by 4-circle X-ray scans of the the $\{hk2\}$ and $\{hk3\}$ planes. The left of Fig. 3.7 shows the (002)-centered $\{hk2\}$ plane with the {112} and the {202} reflections. On the right the $\{hk3\}$ plane reveals the {103} and the {203} reflections. All reflections expected from the $P6_3$/mmc symmetry were found indicating a sufficiently coherent sublattice order [40].

For many simple metals the optimum growth temperature can be estimated to be $\frac{3}{8}T_{\mathrm{melt}}$ [49]. For the epitaxial growth of intermetallics and ordered alloys a slightly larger fraction of the melting temperature should be chosen because of a slower diffusion caused by the non-equivalent atomic species and lattice sites [50]. For $TiFe_2$ the congruent melting point is 1700 K [22]. This leads to an estimated lower bound for the epitaxial temperature of $\frac{3}{8}T_{\mathrm{melt}} \cong 640\,\mathrm{K}$ to $\frac{1}{2}T_{\mathrm{melt}} \cong 850\,\mathrm{K}$. Taking this rule as a guide for the choice of an appropriate substrate temperature range, several samples with equal composition, thickness

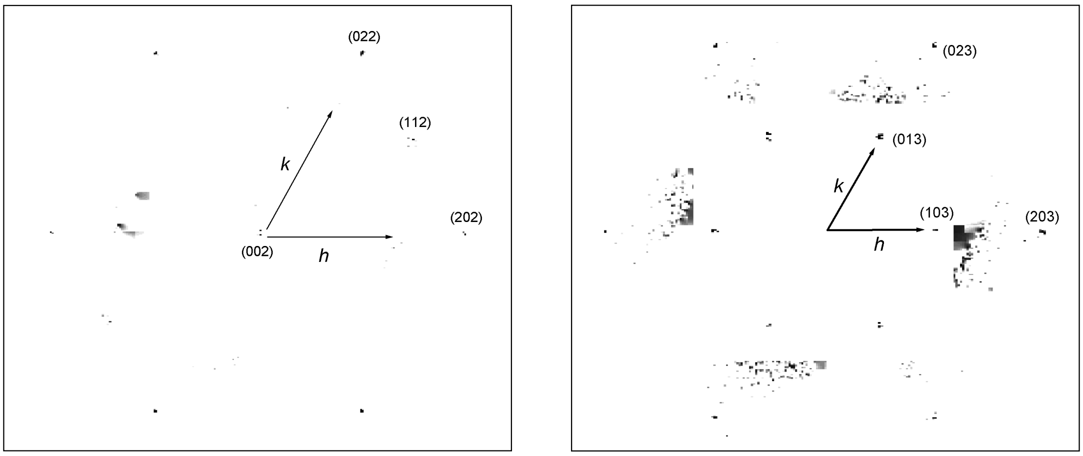

Figure 3.7: Q-scans of the $\{hk2\}$ (left) and the $\{hk3\}$ planes (right). The direction of the reciprocal lattice base vectors are indicated by the arrows. The reflections are labelled representatively for the equivalent reflections. The intensities, indicated by the grey scale contrast, are not to scale.

and varying deposition temperature were prepared in order to determine the optimum growth temperature for epitaxial and single crystalline growth. The indicators used for the optimization were sharpness, intensity and stability of the RHEED patterns during growth. RHEED patterns analyzed in this work were generally obtained at an acceleration voltage of 9 keV and an incident angle of 1.6 °, as mentioned in chapter 2. Additionally, the normalized intensity of the $TiFe_2(004)$ Bragg reflection in longitudinal scans and the width of transverse scans (rocking curves) of the $TiFe_2(004)$ reflection performed with a 2-circle X-ray diffractometer (Cu-K_α) were examined.

The top of Fig. 3.8 depicts the evolution of the (004)-reflection for a series of samples grown at different substrate temperatures T_{sub}. The highest intensity is observed for $T_{\mathrm{sub}} \cong 1100\,\mathrm{K}$ which amounts to the highest temperature obtainable with the available substrate heater. No epitaxial c-axis growth was observed below $T_{\mathrm{epi}} = 825\,\mathrm{K}$. At the bottom of Fig. 3.8 the normalized rocking curves of the (004)-reflection are compared. The rocking curves split into two components: a weakly pronounced broad Gaussian component and a more intense resolution limited component as described in [51]. This two-component line shape was recently quantitatively explained by Barabash et al. [52]: the narrow component is due to the specular Bragg contribution damped with increasing film thickness as a consequence of misfit dislocations induced at the film/substrate interface. The diffuse broad component is caused by the dislocation-network-induced lattice distortion. For the present samples the overall shape does not depend on T_{sub}

during growth. Thus, the ratio of the mosaic-like to the epitaxial contribution is not changed, but the films' coherent volume is increased with increasing T_{sub}.

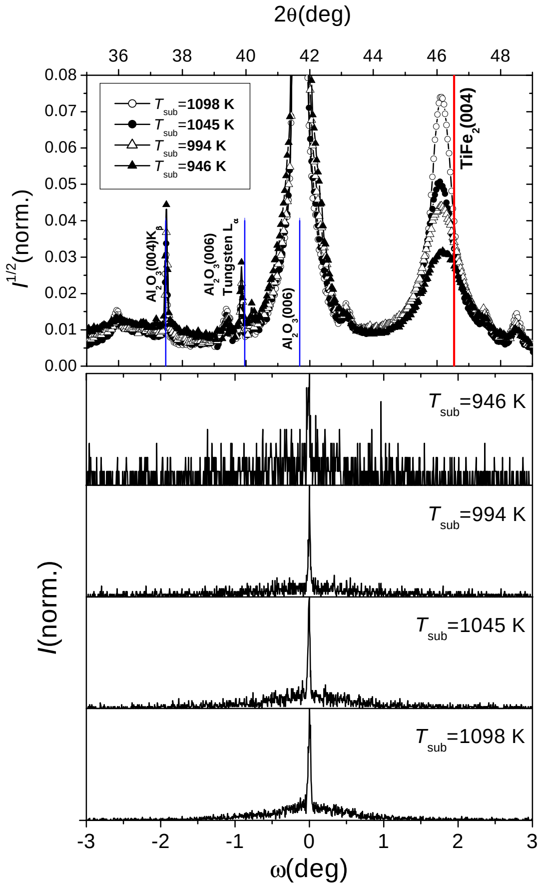

Figure 3.8: Dependence of the $TiFe_2$(004) reflection on the deposition temperature T_{sub}. Top: longitudinal X-ray scan of the $TiFe_2$(004) reflection showing the dependence on the deposition temperature T_{sub} for $x = 0.34$. Higher deposition temperatures promote an increase of the integrated intensity. All other reflections are not due to the thin film. Bottom: Transverse X-ray scan (rocking curve) of the $TiFe_2$(004) reflection. The ratio of the integrated intensity of the narrow component and the broad mosaic-like component remains almost constant.

The effect of the deposition temperature on the crystalline in-plane order of the samples was examined by Φ-scans taken by a 4-circle diffractometer employing Cu-K_α radiation (see Fig. 3.9). Two samples with $x = 0.25$ were chosen because of their higher intensity of the (004) reflection (see below), but other compositions gave very similar results. Both samples have a well-defined sixfold symmetry, but the reflection of the sample deposited at a lower temperature splits into a broad component, indicating a mosaic-like spread, and a narrow component, indicating a highly coherent lateral crystal structure. In addition, for the sample prepared at $T_{\mathrm{sub}} \cong 880\,\mathrm{K}$ an increased background intensity is found which is probably due to residual polycrystalline contributions of the sample. In contrast, the peaks of the sample deposited at higher temperature consist only of the narrow component, thus indicating a reduction of the mosaic-like in-plane spread for low x samples with increasing substrate temperature. The FWHM of the reflections amounts to $0.56\,^{\circ}$. This small value again indicates the good crystalline coherence of the epitaxial thin films.

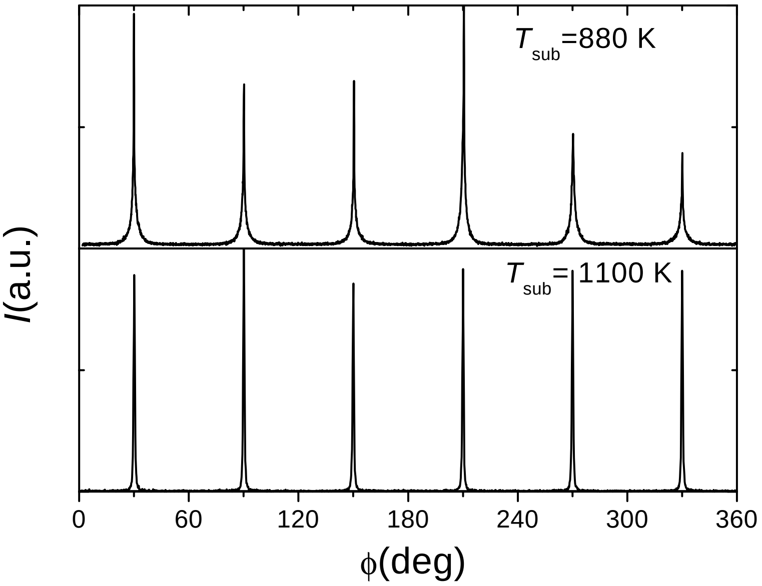

Figure 3.9: Φ-scans of the $\{112\}$-reflections of two samples grown at different temperatures as indicated. The sample deposited at $T_{\mathrm{sub}} = 1100\,\mathrm{K}$ shows a significantly reduced mosaic component. Both samples have $x = 0.25$. Varying peak intensities are due to the small peak width in conjunction with the coarse Φ-resolution and a small misalignment of the sample.

The influence of the deposition temperature on the growth process was also analyzed by RHEED. A common observation during the preparation of all samples was the gradual disappearance of the RHEED pattern with deposition time. The time period over which RHEED patterns were observable was significantly extended by increasing the deposition temperature. Fig. 3.10 shows a series of RHEED images for two samples with $x = 0.34$ deposited at $T_{\mathrm{sub}} = 950\,\mathrm{K}$ and $T_{\mathrm{sub}} = 1100\,\mathrm{K}$, respectively. The left images depict the RHEED-patterns along the $[1\bar{1}0]$-direction after 30 % of the deposition time and the right images the patterns along the same direction after deposition. For the sample grown at lower T_{sub} the reflections show dot-like contributions indicating surface roughness by

3D scattering. The first Laue order reflections are only faintly visible. The patterns almost completely vanish until the deposition ends. The sample deposited at elevated temperature exhibits no 3D scattering but distinct first order reflections. In addition, intermediate reflections between the main reflections appear which may indicate a superstructure due to surface reconstruction. This pattern is stable with only a slight loss of intensity until the end of the deposition. A more detailed analysis of the evolution of the RHEED patterns is given in section 3.2.3. In conjunction with the results of the transverse X-ray scans, a loss of crystalline coherence with increasing film thickness and decreasing deposition temperature can be stated.

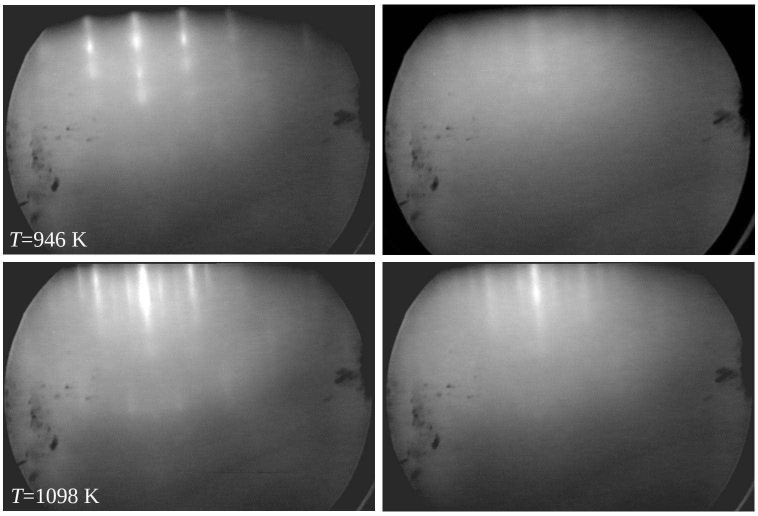

Figure 3.10: RHEED images taken along the $[1\bar{1}0]$-azimuth at different growth temperatures at 30 % of the deposition time (left) and the deposition end (right). The irregular black spots are due to defects on the fluorescence layer of the screen.

Furthermore, the effect of annealing was analyzed. A sample was deposited at $T_{\mathrm{sub}} = 880\,\mathrm{K}$ until almost all RHEED reflections had disappeared resulting in a thickness of 8.8 nm. Left at this temperature for 24 h no visible change in the RHEED pattern was observed. Subsequently, the sample was annealed in-situ at 1100 K for 105 minutes. This induced a reappearance and a significant improvement of the RHEED diffraction pattern: first order and superstructure reflections appeared in addition to the $(0, n)$ reflections. After cool-down to room temperature reflections up to the Laue order $N = 3$ could be detected (see Fig. 3.11). Longitudinal X-ray scans of the sample revealed strongly enhanced $(00l)$-reflections with finite-thickness fringes. The appearance of additional reflections indicate a competitive nucleation of (110)-oriented grains of the C14 Laves phase (see Fig. 3.12). This is in accordance with the previous studies that showed that

Figure 3.11: Effect of annealing on the RHEED patterns along the [100]-azimuth of a $\mathrm{Ti}_x\mathrm{Fe}_{1-x}$ thin film with $x = 0.28$. First, the sample was deposited at $T_{\mathrm{sub}} = 880\,\mathrm{K}$ (left), then the sample was annealed in-situ at $T_{\mathrm{sub}} = 1100\,\mathrm{K}$ for 105 min. (middle), and cooled to $T_{\mathrm{sub}} = 400\,\mathrm{K}$ (right).

below the epitaxial temperature a (110)-textured nucleation of grains is favored (section 3.1, [53]).

Another sample was deposited at 1100 K and kept at this temperature for 1 h. This resulted in minor improvements of the RHEED patterns but again, as indicated by longitudinal X-ray scans, the formation of other growth directions and Fe phase-separation.

The epitaxial temperature, where epitaxial growth sets in, was determined to $T_{\mathrm{epi}} \cong 825\,\mathrm{K}$. An optimum epitaxial deposition temperature of $T_{\mathrm{opt}} \cong 1100\,\mathrm{K}$ was found. Crystal growth of high lateral and longitudinal coherence was obtained up to a thickness of at least 25 nm at growth rates of 0.02 to 0.03 nm/s. T_{epi} is in accordance with the estimation given in the beginning of this section. Fig. 3.13 shows a typical longitudinal scan and reflectometry data for a sample grown under optimal conditions. No secondary phase formation was observed. The surface

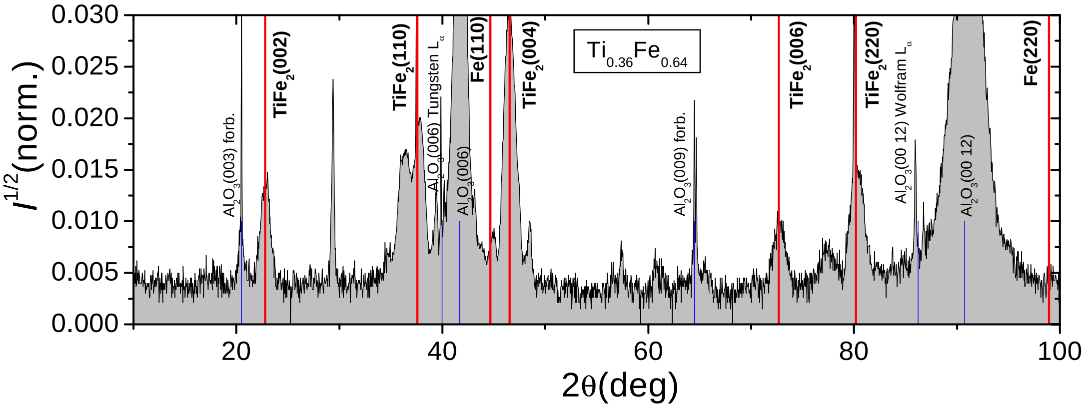

Figure 3.12: Effect of annealing on the grain growth: a longitudinal X-ray scans of the sample (see Fig. 3.11) reveals enhanced (00l)-reflections with finite-thickness fringes and a competitive nucleation of (110)-oriented grains. Peaks without labels could not be identified.

roughness amounts to $\sigma_{\mathrm{rms}} = 0.5\,\mathrm{nm}$ allowing for an accurate determination of the film thickness.

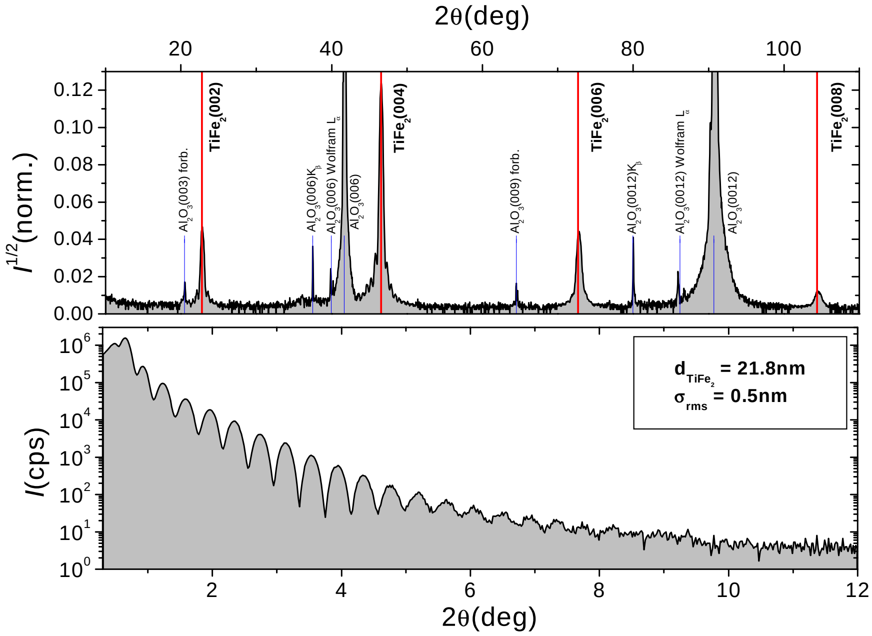

Figure 3.13: Longitudinal X-ray scan of a typical sample grown under optimal conditions (top). Low-angle X-ray scan of a typical sample (bottom). Film thickness and roughness were determined from a Parratt analysis [43].

Simulations of longitudinal scans exhibiting finite size oscillations were performed within a kinematical model. As a result, for samples with thicknesses below 25 nm the coherence length perpendicular to the film plane corresponds to the respective sample thickness as determined by low-angle XRD. A further increase of the thickness causes a loss of lateral coherence and an increase of the broad component of the rocking curve. Post-annealing results only in minor improvements of the crystalline order of samples already grown at 1100 K. As it also promotes the growth of misaligned grains this thermal treatment was not used for the samples analyzed below.

3.2.3 Time dependence of RHEED patterns

The typical time-dependent evolution of the RHEED-patterns along the $[1\bar{1}0]$-direction at the optimum deposition temperature $T_{\mathrm{sub}} = 1100\,\mathrm{K}$ is shown in Fig. 3.14. RHEED streaks indicating 2-dimensional growth almost instantly appear at the (0,0), (0,±1) and (0,±2) positions of the substrate reflections (a,b) indicative of the epitaxial 1:1 relation of the first layers. After the first two

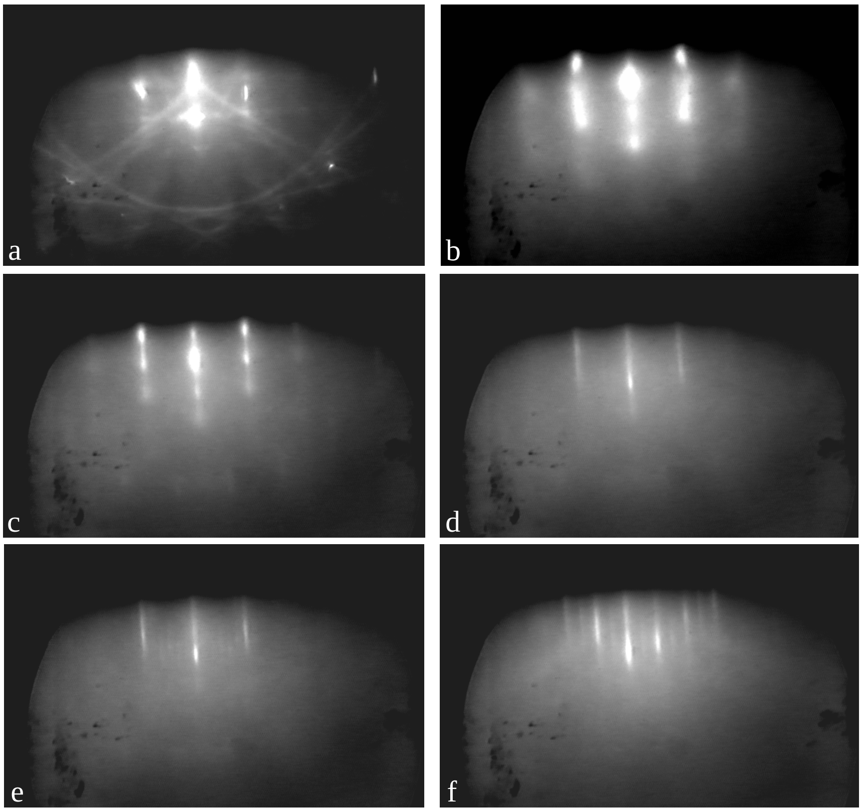

Figure 3.14: Time evolution of the RHEED patterns of a thin film with $x = 0.273$ at $T_{\mathrm{sub}} = 1100\,\mathrm{K}$. The images were taken along the $[1\bar{1}0]$ azimuth after (a) 0 s, (b) 20 s (0.6 ML), (c) 80 s (2.5 ML), (d) 390 s (12 ML), (e) 700 s (21.5 ML) (at deposition end) and (f) (at deposition end along [100] azimuth).

monolayers dot-like patterns develop on the streaks most likely due to volume-diffraction contributions as a consequence of increasing roughness. With increasing film thickness the 3D scattering contributions gradually disappear (c). First and, occasionally, second order reflections evolve after 2-3 monolayers, but their intensity and sharpness gradually decreases with deposition time. The overall reflection intensity decreases until approximately 10 ML have been deposited. This may be caused by an increasing number of crystal defects inserted during growth that causes a shift of spectral weight from the reflections into the diffuse background. Simultaneously, the sharpness slightly increases due to the growing lateral crystalline surface coherence (d). No significant change is visible until deposition end since most relaxation-driven growth effects appear to be in equilibrium after approximately 10 ML (e). Faint indications of intermediate reflections at $(0,n \pm \frac{1}{3})$ become visible and appear more distinct during sample cool-down (see Fig. 3.15, bottom row). For the [100] azimuth a well defined pattern of the

$N = 0$ Laue order complying with the new symmetry direction is observed (f). The streak profiles are comparable to those taken in $[1\bar{1}0]$-direction. At the positions $(0,n \pm \frac{1}{2})$ additional low intensity reflections occur indicating a doubling of the periodicity of the $\{010\}$ surface-rows. A continuation of the deposition process results in a gradual decrease of the intensity. In transverse X-ray scans an increased contribution of the mosaic-like component is found. Two possible reasons for the intermediate reflections at non-integer positions are a corresponding surface reconstruction, either driven by residual gas adsorption because of the getter-capabilities of Ti (and Fe) or by an amount of Fe segregation which is beyond the detection limit of the XRD experiments. Instead of segregation a periodic occupation of Ti sites by Fe atoms may occur. This would cause a periodic Fe cluster structure in the lattice and yield superstructure reflections in RHEED patterns. In Mößbauer spectroscopy measurements clustering due to antisite occupation by Fe atoms was deduced for bulk samples [26].

3.2.4 RHEED patterns and composition

The quality (sharpness and intensity) of the RHEED patterns during deposition strongly depends on the composition of the films. A comparison of the diffraction patterns taken at 400 K for three different compositions about the stoichiometric point for samples prepared at $T_{\mathrm{sub}} = 1100\,\mathrm{K}$ is presented in Fig. 3.15. Along both, the [100] and $[1\bar{1}0]$ azimuths, a common behavior is observed: at high x epitaxial growth is observed with medium intensity $N = 0$ reflections coinciding with the substrate reflex positions within our experimental resolution. Two low-intensity intermediate reflections (see above) evolve between the main reflections along the $[1\bar{1}0]$-direction but not for the [100]-direction. For both directions faint first order reflections can be detected. At approximately stoichiometric composition all reflections appear more distinct and the first order reflections along the [100] azimuth show low intensity intermediate reflections, too. The sample situated at the Fe/TiFe$_2$ phase boundary of the range of homogeneity ($x = 0.273$, see section 3.2.5) exhibits the highest image contrast and rather sharp reflections along both directions. In addition to the intermediate reflections observed for the other compositions more intermediate reflections appear for the $[1\bar{1}0]$-direction at $(0,n \pm \frac{1}{6})$ and $(0,n \pm \frac{3}{6})$ indicating a periodicity $\Lambda_{\mathrm{perp}} = 6a$ perpendicular to the $[1\bar{1}0]$-direction. An analysis of the reflection intensities reveals a shift of the spectral weight into the intermediate reflections. Furthermore, the formation of $N = \frac{1}{2}$ Laue order reflections can be observed indicating a doubling of the periodicity Λ_{par} parallel to the $[1\bar{1}0]$-direction. This same doubling of periodicity is observed for the [100] azimuth in conjunction with distinct $N = 1$ order reflections.

In summary, Ti$_x$Fe$_{1-x}$ in the C14 Lave phase stability range perfectly adopts the symmetry of the substrate surface and grows epitaxially with a 1:1 relation-

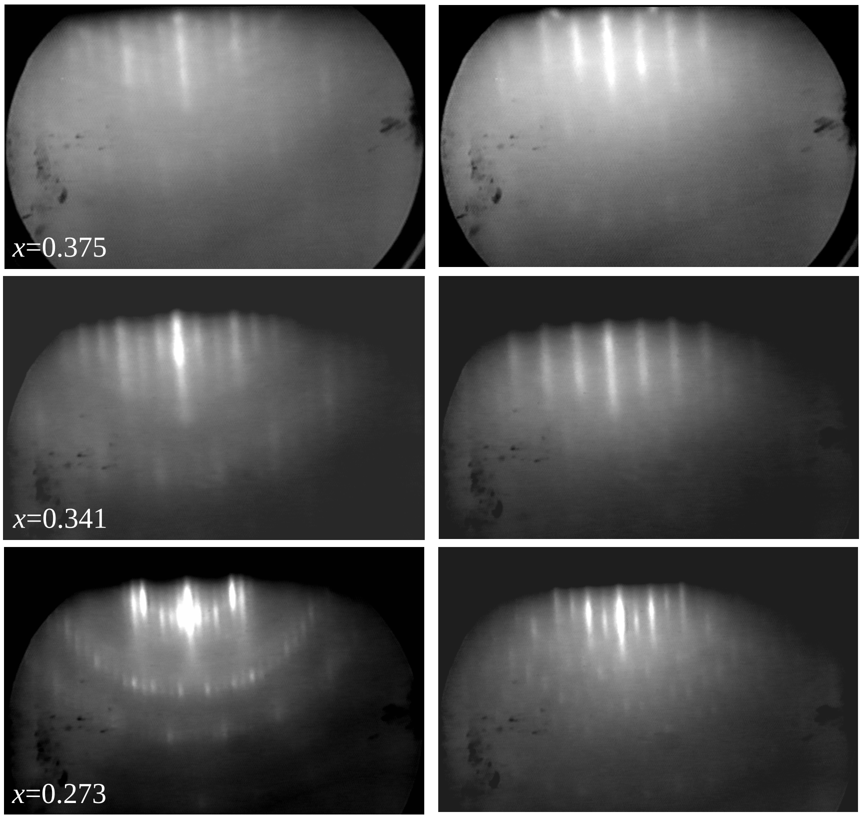

Figure 3.15: Dependence of the RHEED patterns on the composition along the $[1\bar{1}0]$- (left) and the [100]-direction (right) at $T \approx 400\,\mathrm{K}$. The images are not to scale.

ship on $Al_2O_3(001)$ substrates at $T_{\mathrm{sub}} = 1100\,\mathrm{K}$, in agreement with the results of section 3.2.2. The growth coherence decreases with deposition time. An, as yet, unidentified superstructure is imposed on the surface during growth. With increasing iron concentration coherent crystal growth is promoted in conjunction with particularly pronounced surface reconstructions. The latter point seems to indicate that the reconstruction is driven by periodic Fe clustering but without chemical information about the composition of the topmost layers this has to remain for future resolution.

3.2.5 Lattice-constants and composition

A series of (00*l*)-oriented thin film samples with varying composition about the stoichiometric point was prepared applying optimal preparation conditions. The growth rate was kept constant for all samples to about 0.02 to 0.03 nm/s. The composition was determined by EDX according to section 3.2.1. The a- and c-axis lengths of selected samples were determined by 4-circle diffractometry using a least-square fit to the {112} and {201} reflections and the (004) reflection. The errors range for the c-axis length from 0.09 % to 0.24 % and for the a-axis length from 0.04 % to 0.16 %. Fig. 3.16 shows a section of longitudinal X-ray scans of the $TiFe_2$(004) reflection as a function of sample composition. The intensities are normalized to the Al_2O_3(006) reflection to facilitate a comparison of the data. Depending on the sample composition three main features can readily be identified: (1) the peak positions continuously shift with composition towards smaller c-axis lengths for increased Fe concentration with respect to the bulk value of the stoichiometric compound, (2) the intensity decreases with increasing Ti concentration and (3) the Fe(110) reflection evolves in the Fe rich region below $x = 0.28$.

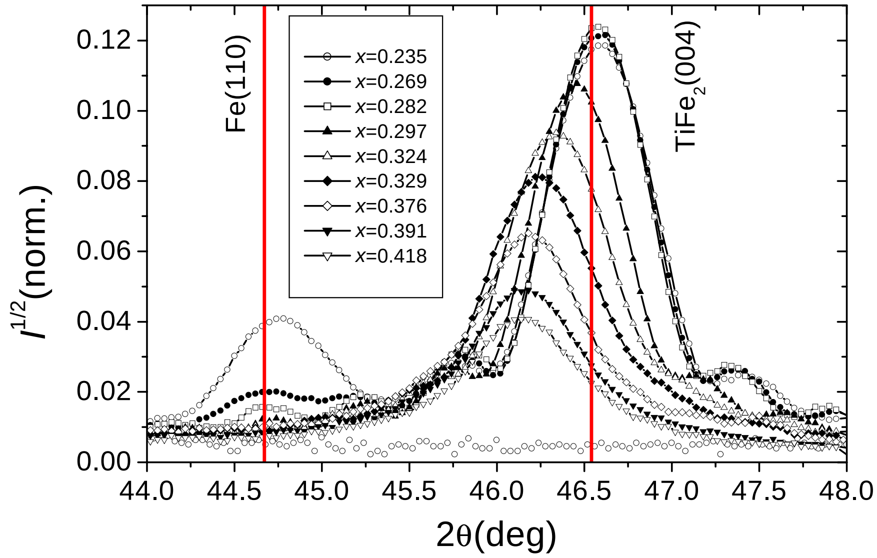

Figure 3.16: Longitudinal X-ray scans of the $TiFe_2$(004) reflection for a series of films with various compositions as indicated. The peak position is shifted towards larger c-axis lengths with increasing x and the Fe(110) reflection evolves at high Fe concentrations.

Fig. 3.17 summarizes the measured a- and c-axis values depending on x as determined by 4-circle XRD for a selected set of films. Starting from high Fe concentration and small lattice constants the a- and c-axis lengths remain constant until approximately $x = 0.27$. This is followed by an increase until saturation sets in for the c-axis length at approximately $x = 0.34$. The a-axis length also increases with the Ti concentration, but starts with a reduced slope at $x = 0.27$ and continues to grow with an increased slope at $x = 0.34$ saturating at 39 % Ti.

The unit cell volume increases linearly within the error bars (see Fig. 3.18) in the range from $x = 0.27$ to 0.39, as one would expect from a hard-ball model. The error in the determination of the lattice constants does not allow for the

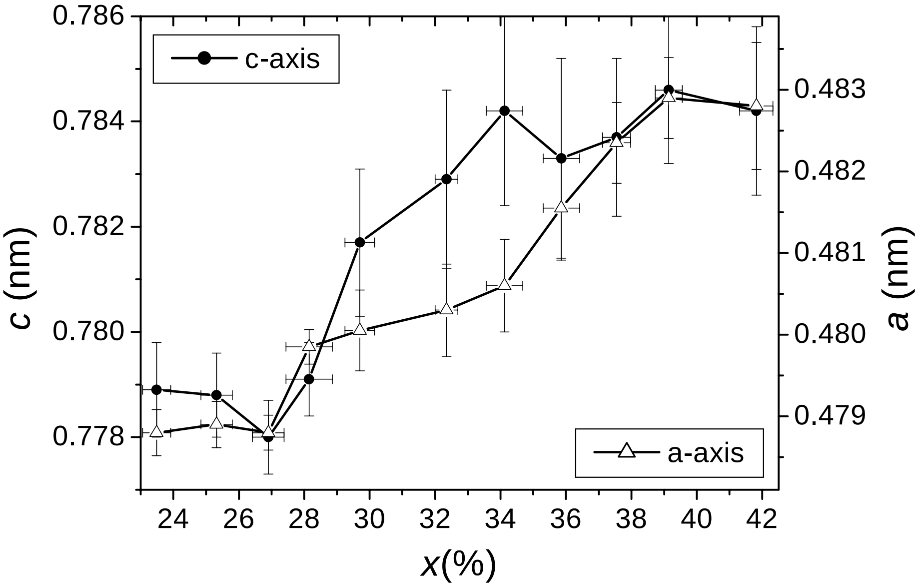

Figure 3.17: Lattice constants as determined by 4-circle XRD. The error bars for x are the statistical errors of the EDX analysis, the uncertainties for the lattice constants result from the least-square fit of the orientation matrix refinement procedure.

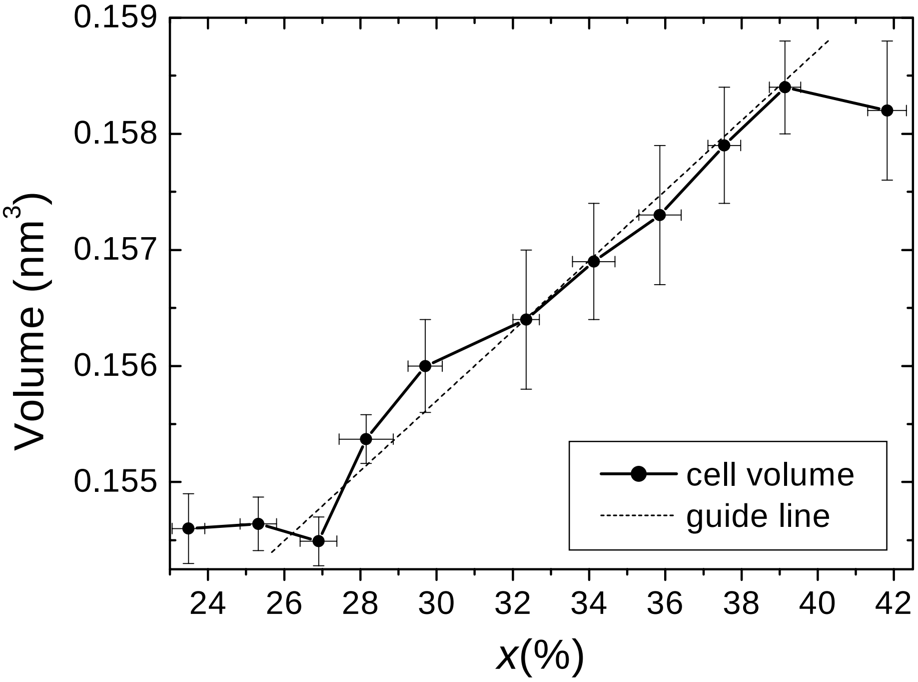

Figure 3.18: Unit cell volume as determined by 4-circle XRD (see also Fig. 3.17).

identification of possible deviations from Vegard's law [54]. From all this can be concluded that the point of saturation of the lattice constants at high Fe concentration corresponds to the onset of Fe(110) segregation. The Ti(4f) sites are occupied by the smaller Fe atoms until oversaturation sets in [25]. On the Ti-rich side the $TiFe_2(004)$ reflection gradually disappears with increasing Ti concentration. The larger Ti atoms do not easily substitute on the Fe sites and thus disturb the overall crystal structure resulting in a loss of coherent X-ray scattering. For $x \geq 0.34$ the complete volume expansion is predominantly caused by an increase of the a-axis length resulting in an appreciable change of the c/a-ratio. Consequently, the range of homogeneity of the C14 structure extends from $x = 0.28$ to 0.39. Since there are 8 Fe and 4 Ti atoms per unit cell, the maximum average substitution is 0.64 Fe atoms per unit cell on Ti sites and 0.68 Ti atoms on Fe sites. This relies on the assumption that there are no secondary phases present which is plausible since the Fe(110) and the TiFe(110) reflection readily appear if the composition lies outside this range.

3.2.6 Ti_xFe_{1-x} surface morphology

For in-situ STM studies as a function of the film thickness under optimum growth conditions, a second group of samples was prepared in the Omicron MBE system as detailed in section 2.2.4. RHEED studies during growth and the XRD analysis confirm that this group of samples is comparable to the first series. In this section two samples are compared with the respective thicknesses of 20 nm and 55 nm and compositions of $x = 0.31$ and 0.32. The STM images were taken immediately after the samples were cooled to room temperature. The data were acquired in constant current mode (0.2 nA) at a tip-to-sample bias of +1 V. The results appear in Fig. 3.19 and 3.20: In large scale scans both samples exhibit three-dimensional islands with island diameters between 50 nm and 200 nm and rms roughnesses of 0.44 nm and 1.05 nm for sample one and two, respectively. The maximum position of the height distribution function, as shown at the bottom of Fig. 3.19 and 3.20, increases with the average film thickness. At higher resolution a rather smooth surface for sample one with an rms roughness of 0.24 nm in conjunction with small facetted regions following the thermodynamic equilibrium shape to be expected for a hexagonal crystal are observed. Sample two shows islanding with rounded step edges and a rms roughness of 1.17 nm. A comparison of the height distributions reveals a distinct step structure for the surface of sample one. The height distribution function peaks at about the height of the unit cell of $TiFe_2$ at 0.78 nm. A line scan along the direction indicated in Fig. 3.20 reveals islands with a height corresponding to half the c-axis length of the C14 phase $TiFe_2$ (see Fig. 3.21). Line scans taken through islands at different locations exhibit multiple heights of c/2. The main peaks in the height distribution function of

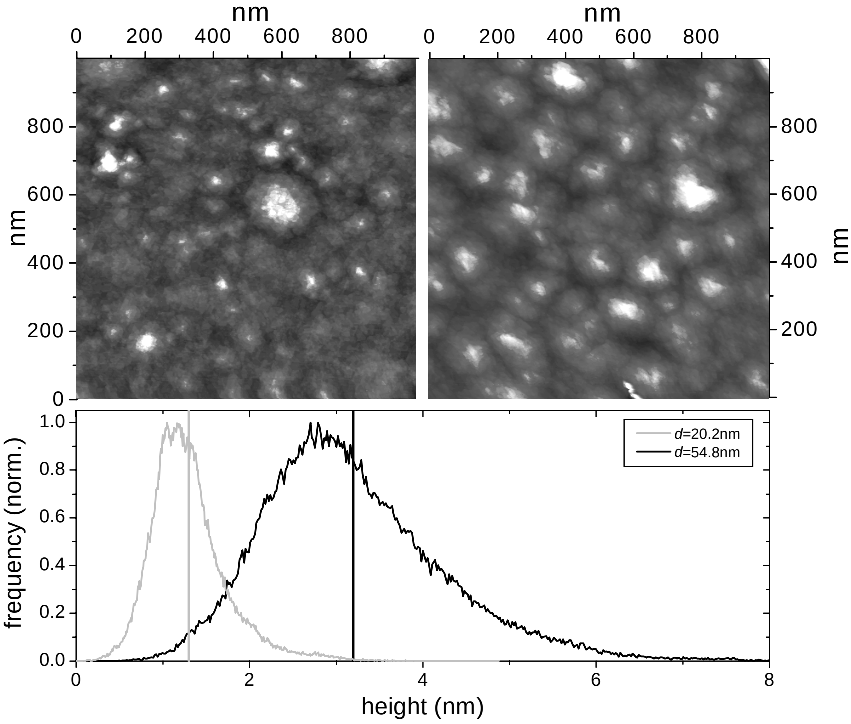

Figure 3.19: Top: In-situ STM images for two $TiFe_2$ surfaces with thicknesses of $d = 20.2\,\mathrm{nm}$ (left) and $d = 54.8\,\mathrm{nm}$ (right) and the same composition. Bottom: Height distribution function and, indicated by vertical lines, the arithmetic average height.

sample two, indicated by vertical lines, are also separated by the $TiFe_2$ unit cell height indicating step edges with the same height.

3.2.7 Conclusions

Epitaxial single phase thin films of Ti_xFe_{1-x} in the C14 Laves phase stability range with c-axis orientation were prepared on $Al_2O_3(001)$ templates by MBE. The epitaxial MBE growth process allows for the preparation of the C14 phase in an extended range of homogeneity as compared to bulk samples prepared from the melt. Epitaxy was confirmed by RHEED and XRD analysis. An epitaxial temperature $T_{\mathrm{epi}} \cong 825\,\mathrm{K}$ and an optimal growth temperature $T_{\mathrm{opt}} \cong 1100\,\mathrm{K}$ were determined at a growth rate of 0.02 to 0.03 nm/s. In a film series with varying composition the unit cell volume increases with the Ti concentration complying with a hard-ball model. The STM analysis of the surface indicate island formation and small-scale facetting according to the thermodynamic equilibrium shape of the hexagonal structure. Increased iron concentrations promote the growth coherence and thus improve the X-ray- and RHEED diffraction patterns. It also

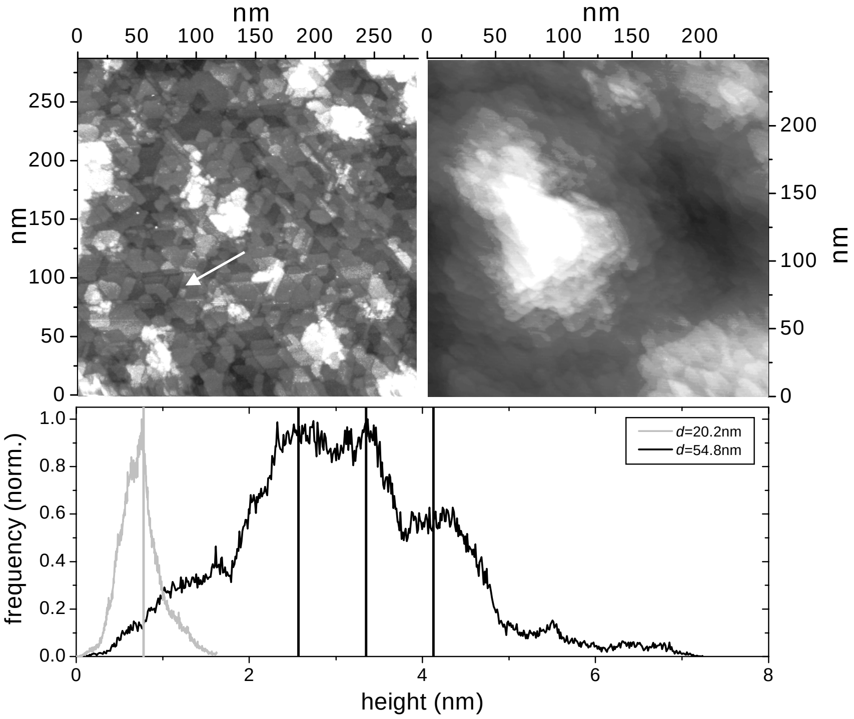

Figure 3.20: Top: Higher resolved STM images of the two samples in Fig. 3.19 with thicknesses of $d = 20.2\,\mathrm{nm}$ (left) and $d = 54.8\,\mathrm{nm}$ (right). The arrow indicates the line scan shown in Fig. 3.21. Bottom: Height distribution function and, indicated by vertical lines, lines at 0.78 nm distance corresponding to the c-axis length of $\mathrm{TiFe_2}$.

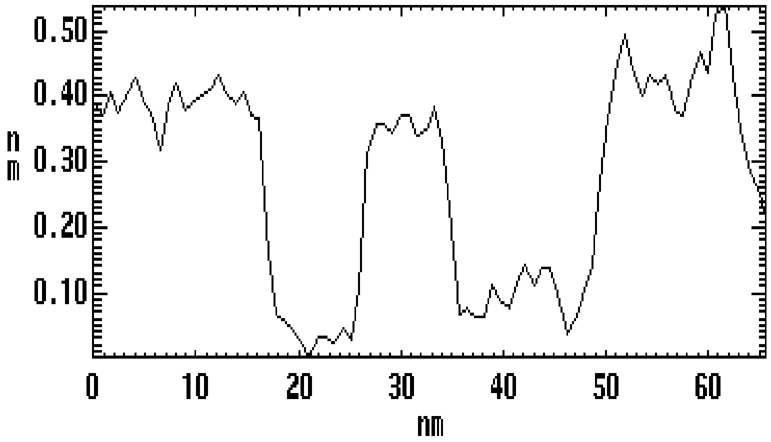

Figure 3.21: STM line scan of sample one (see arrow in Fig. 3.20). The height of the islands corresponds to half the c-axis length of the $\mathrm{TiFe_2}$ C14 phase.

promotes the formation of surface superstructures as found in the RHEED analysis. This may be due to a periodic surface manifestation of iron clustering in the bulk, as was previously deduced from Mößbauer spectroscopy studies [26]. Further analysis must provide the origin of the driving mechanism of this superstructure formation and its relation to coherent crystal growth. Studies of the magnetic properties of bulk crystals of $\mathrm{Ti}_x\mathrm{Fe}_{1-x}$ in the C14 stability range always suffered from preparational difficulties with regard to homogeneity and phase purity [8,11]. Based on the improved phase purity of the epitaxial films an alternative pathway for a systematic study of the composition-dependent magnetic properties of $\mathrm{Ti}_x\mathrm{Fe}_{1-x}$ is established. A detailed analysis of the magnetic properties of the samples prepared in this work is presented in chapter 6.

Chapter 4

Measuring low magnetic moments with the SHE SQUID magnetometer

All temperature- and magnetic field-dependent magnetization measurements of the samples were performed with a SHE radio frequency superconducting quantum interference device (rf-SQUID) magnetometer [55]. The instrumental resolution of the SQUID magnetometer is specified with $10^{-8}\,\mathrm{emu}$ (=erg/G) in Gaussian units or $10^{-11}\,\mathrm{J/T}(=\mathrm{Am}^2)$ in SI units. The presented magnetization measurements were performed in external fields $|\mu_0 H_{\mathrm{ext}}| \leq 1\,\mathrm{T}$ and at temperatures $5\,\mathrm{K} \leq T \leq 300\,\mathrm{K}$. At elevated temperatures and large external magnetic fields instabilities in the SQUID signal of the SHE magnetometer were detected. Additionally, an asymmetric contribution caused by the wire sample holder was found to be superimposed to the signal. To compensate these effects a simulation method for the effective signal was developed which allows to measure small-moment samples with an improved precision.

Consequently, this chapter is concerned with the SQUID measurement process and the consecutive data processing which was performed to obtain the data presented in chapter 5 and 6. In section 4.1 a short overview is given of the rf-SQUID. Next, the sample mounting and alignment for high-resolution (HR) measurements is described. Finally, in section 4.3 a signal correction method by applying a non-linear least-squares fit to the SQUID signal is presented.

4.1 SHE rf-SQUID magnetometer

A detailed description of the SHE rf-SQUID magnetometer can be found in [55]. Nevertheless, a brief overview of the instrument, necessary for the understanding of the following sections, shall be given here.

The main sensor device in the magnetometer is the rf-SQUID head. A superconducting ring with one weak link is coupled to an LC-circuit operating in the MHz range.

The external magnetic flux Φ_{ext}, which acts on the SQUID, is a superposition of the flux Φ_{dc} of the magnetic sample and the flux Φ_{ac} of the LC circuit. For a constant amplitude of the current in the LC circuit (called rf-level), the voltage U_{rf} at the capacitor of the circuit shows a triangular-shaped functional dependence on Φ_{dc}. A dc-current is back coupled and induces a compensating flux in the pick-up coils fixing the operating point to the peak of the triangular response function U_{rf}. The back coupled current is a measure for Φ_{dc}. For further information on rf-SQUIDs see [55].

The SQUID magnetometer is cooled by liquid ^{4}He. A constant flux of He gas through the sample space is injected through a capillary connected to the main bath. The He flow in combination with a gas heater allows to control the sample temperature in the range $4.3\,\mathrm{K} \leq T_{\mathrm{sample}} \leq 300\,\mathrm{K}$. In the present experiment, a carbon glass resistor (CGR) sensor was used for temperature measurement and control during the magnetization measurements. The sample holder is attached to a Ti ribbon which cycles the sample between the two pick-up coils, driven by a stepping motor. An external magnetic field up to $\mu_0 H_{\mathrm{ext}} = 5\,\mathrm{T}$ can be applied by a superconducting magnet. The maximum remnant magnetic field of NbTi magnets, as used in the present SQUID magnetometer, amounts to approximately 40 Oe after generation of an external field in excess $\mu_0 H_{\mathrm{ext}} = 1\,\mathrm{T}$ and is thus assumed as the maximum remnant field in the sample area.

4.2 Sample alignment

The sample was attached to the sample holder dangling from a metal connector clamped to the Ti ribbon. While the sample holder is cycled through the pick-up coils the magnetic properties of the holder significantly determine the shape of the SQUID signal. For either a paramagnetic or diamagnetic sample holder with any mounting asymmetry with respect to the symmetry center of the pick-up coils, the SQUID signal will be asymmetric, too. This asymmetry is not negligible if the mass and thus the magnetic moment of the holder is large as compared to the sample moment.

One standard method is to mount the sample in the center of a (diamagnetic) plastic straw. The straw is cycled between the pick-up coils. The SQUID signal is generated by subtracting the signal of one coil from the signal of the other. If the straw is long enough with respect to the distance between the pick-up coils ($l_{\mathrm{straw}} \gg d_{\mathrm{coil}} = 50\,\mathrm{mm}$), both coils generate the same signal and the difference signal of the straw is cancelled. In this case, the remaining signal purely originates from the sample. Unfortunately, the distance between the lower coil and the bottom of the sample space is only 50 mm [55]. Thus, the length of the straw is limited and the difference signal of both coils does not cancel, yielding an asymmetric SQUID signal. Since the signal of the samples measured in this work were rather small as compared to the signal of the straw, this method was not applicable.

A suitable method was found by attaching the sample to a sufficiently thin copper wire ($d_{\text{wire}} = 100\,\mu$m). The 2.5x2.5x0.5 mm^3 sized samples were fixed using a "gift" package method (see Fig. 4.1) with symmetric alignment of the wire with respect to the sample. The ends of the wire were twisted to a length of approximately 15 cm and attached to the metal holder. The signal of this alignment is still asymmetric but, due to the thin wire, significantly reduced as compared to the straw method. Furthermore, the arrangement of the symmetric packaging of the sample and the mostly uniformly twisted wire is well defined and facilitates a simulation of the sum signal (see section 4.3).

For in-plane measurements the sample was aligned with the film plane parallel and for out-of-plane measurements perpendicular to the external field. The respective angle was estimated by visual inspection.

4.3 Enhancing resolution by fitting the SQUID signal

The data acquisition program [55] returns in the peak-to-peak mode the difference between the maximum and minimum value of the SQUID signal taken during one complete cycle through the pick-up coils. This is proportional to the magnetization. Several problems prevent a direct evaluation of these signals:

1. Large discontinuities of the SQUID signal occur preferably at high external fields. The origin of this behavior could not be unambiguously identified.
2. A large linear drift of the SQUID signal with time occurs at high magnetic fields. This may be induced by the extended time over which the magnet approaches the set point. Though, large time scale experiments exhibited no saturation of this effect.
3. The SQUID signal is asymmetric, caused by the asymmetric arrangement of the Cu wire and the sample.

To obtain a reasonable evaluation the complete SQUID signal of one cycle was extracted and analyzed. Problem (1) was solved by removing the discontinuities by a Matlab [56] filter program which relies on the large signal jump of the discontinuity as compared to the expected quasi-continuous behavior of neighbored data points. As the drift of the signal was almost linear, problem (2) was solved with the same program by subtracting a linear background. Problem (1) was treated by applying a non-linear least-squares fit to the resulting data. The fit was performed consecutively on all buffer files by a Mathematica [57] program. A brief description of the fit formula used is given here:

A point-like dipole with a magnetic moment m at the origin of the coordinate system generates a magnetic flux Φ in a single-winded coil with radius R_0 centered at distance z according to [58]

$$\Phi(z) = 2\pi\mu_0 m \frac{R_0^2}{(R_0^2 + z^2)^{3/2}} \tag{4.1}$$

Fig. 4.1 illustrates the arrangement of the sample between the pick-up coils and the corresponding variables. In the present case the dipole extends along z over the range $[-L_-, +L_+]$ with a magnetic moment distribution denoted as $\rho(z)$. Integration yields

$$\Phi(z) = 2\pi\mu_0 \int_{z-L_-}^{z+L_+} \rho(z_0) \frac{R_0^2}{(R_0^2 + z_0^2)^{3/2}}\, dz_0 \tag{4.2}$$

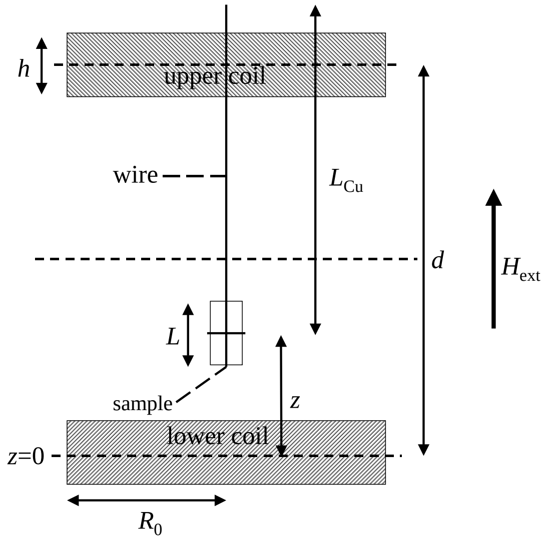

Figure 4.1: Sample arrangement in the SHE SQUID magnetometer. h denotes the height, R_0 the radius and d the distance of the pick-up coils. $L = L_- + L_+$ is the length of the sample, L_{Cu} the length of the Cu wire. The coordinate of the center of the lower coil is denoted z.

If we assume a homogeneous distribution $\rho(z) = \rho_m = \frac{m}{L}$ equation 4.2 simplifies to

$$\Phi(z) = 2\pi\mu_0\rho_m \int_{z-L_-}^{z+L_+} \frac{R_0^2}{(R_0^2 + z_0^2)^{3/2}}\, dz_0 \tag{4.3}$$

As the coils have a non-zero height they symmetrically extend along z in the range $[-\frac{h}{2}, +\frac{h}{2}]$. Assuming that the flux pick-up mechanism is homogeneous along the coil, the local flux density $\rho_\Phi = \frac{\Phi(z_1)}{h}$ can be introduced. Again, integration for a single looped coil yields

$$\Phi(z) = 2\pi\mu_0 \frac{\rho_m}{h} \int_{z-h/2}^{z+h/2} \int_{z_1-L_-}^{z_1+L_+} \frac{R_0^2}{(R_0^2 + z_0^2)^{3/2}} \, dz_0 \, dz_1 \tag{4.4}$$

For a coil with multiple loops the signal is just scaled with a constant factor. The SQUID signal for two pick-up coils separated by d is generated by positioning the second coil at $z-d$ and adding the signal according to equation 4.4. Moreover, the additional contribution of the wire is easily included by introducing ρ_w, $L_{\mathrm{w}-} \approx 0$ and $L_{\mathrm{w}+}$ in equation 4.4. Fig. 4.2 shows how the sum signal is formed by adding the symmetric sample signal and the asymmetric wire signal.

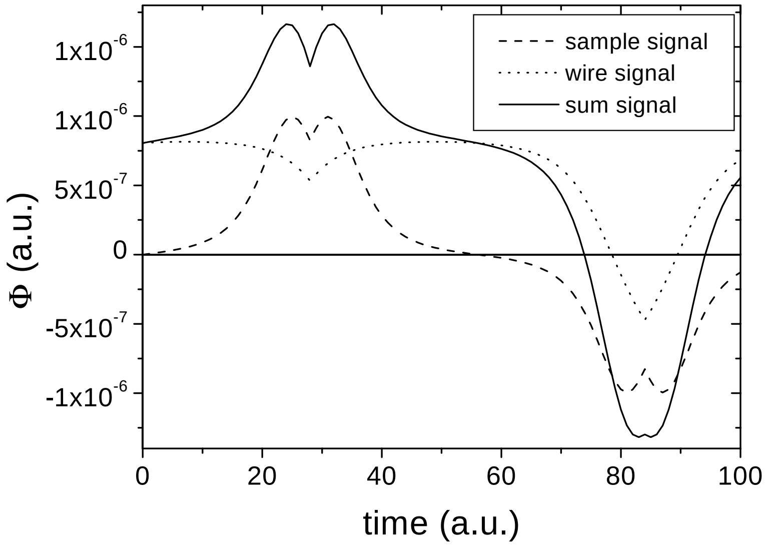

Figure 4.2: Simulation of the time evolution of the SQUID signal for a magnetic sample cycling between two pick-up coils. The asymmetric signal of the Cu wire is superimposed. The sample is cycled a short distance above the upper and below the lower coil indicated by the dips at the extremals.

The parameters involved in the fitting were the height h, the radius R_0 and the distance d of the pick-up coils, the length of the sample below and above the center L_+ and L_-, the length of the Cu wire below and above the center $L_{\mathrm{w}-}$ and $L_{\mathrm{w}-}$, the magnetic moment m of the sample and of the wire m_Cu and a flux offset $\Delta\Phi$. As the alignment of the sample and wire in the SQUID varied from sample to sample, the first step in the analysis was the determination of the parameters for the new geometry. This was performed with simulation and fitting based on the data analysis software Microcal Origin 6.0 [59] employing a

LabTalk$^{\mathrm{TM}}$ script. A sample signal curve with the best fit curve is presented in Fig. 4.3. The thus obtained fit parameters were entered as starting parameters for a Mathematica [57] fit program which offers a fast non-linear least-squares fit routine. The only parameters in the program set as non-fixed were the magnetic moment of the sample, the magnetic moment of the Cu wire and the flux offset which varied between the measurements. Sufficient accuracy $\Delta m \approx 5 \times 10^{-10}$ J/T for the samples with the lowest saturated magnetic moment of $m_{\mathrm{S}} \approx 4 \cdot 10^{-8}$ J/T was achieved.

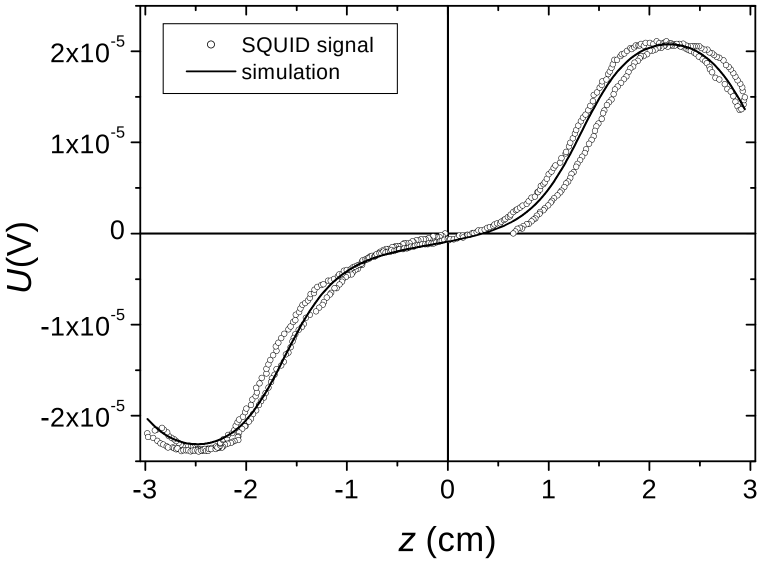

Figure 4.3: Non-linear least-squares fit using the Levenberg-Marquardt algorithm (solid line) of a typical asymmetric SQUID signal (circles). The ordinate is the relative position of the sample with respect to the center of the upper and lower pick-up coil. A complete cycle is performed indicated by the overlay of the up and down cycle curve.

Chapter 5

Exchange bias and magnetoresistance in textured thin film samples

Exchange bias (EB) effects in inhomogeneous materials have been observed in numerous earlier experiments. However, the intrinsic near-degeneracy of antiferromagnetism and ferromagnetism in the $TiFe_2$ system in conjunction with magnetic AF/FM clustering, which is associated with compositional inhomogeneities, results in a more or less pronounced EB at the AF/FM interface of these clusters. In the present case the possibility to prepare polycrystalline samples allows for the formation of large interfaces. This facilitates the detailed analysis of the EB in inhomogeneous magnetic systems for which $TiFe_2$ due to its structural homogeneity may serve as a reference compound.

A $TiFe_2$(110) textured polycrystalline sample with $x = 0.32$ was prepared in the Omicron MBE system as described in chapter 2. The sample exhibits besides the $TiFe_2$(110) and (220) reflections only TiFe(110) and (220) reflections in longitudinal X-ray scans (see section 3.1). Considering the form factors of these reflections [40], a ratio of $TiFe_2$(110):TiFe(110) of about 10:1 can be estimated. Since TiFe is paramagnetic in its crystalline bcc phase [11,41,42], any magnetic moment in the sample can be associated with the properties of the $TiFe_2$ phase. In this chapter the magnetic properties of this sample are analyzed. The magnetization measurements were performed using the in-plane geometry as described in chapter 4. After a brief review of the exchange bias phenomenon in section 5.1.1, magnetic susceptibility measurements are presented in section 5.1.2. An EB effect was found in the magnetic isotherms which is described in section 5.1.3. The chapter concludes with a discussion of the results.

5.1 Exchange bias in textured thin films

5.1.1 Exchange bias: a short introduction

Magnetic heterogenous systems with interfaces of FM and AF ordered regions and $T_\mathrm{C} > T_\mathrm{N}$ typically exhibit an unidirectional magnetic anisotropy when the system is cooled to below T_N from $T > T_\mathrm{N}$ while a magnetic field H_FC is applied. Due to this anisotropy the magnetic hysteresis loop is usually shifted to the opposite direction of the applied field. This offset field is called the *exchange bias* field H_EB.

In 1956 Meiklejohn and Bean [60] discovered this phenomenon during their research on oxidized Co particles (see Fig. 5.1). The particles were cooled in zero field to below T_N of CoO and the hysteresis curve showed a symmetric FM hysteresis curve (dashed line). If the sample was cooled in a saturating magnetic field a significant shift and enhanced coercivity could be detected (solid line). Meiklejohn and Bean attributed it to an interaction between the ferromagnetic Co and its native antiferromagnetic oxide CoO. In subsequent publications [61,62] more detailed explanations were given by these authors. Since that time many systems where found exhibiting a similar behavior, such as small coated particles, granular and inhomogeneous systems, polycrystalline and textured thin films and coated single crystals. The effect is not limited to AF/FM interfaces but is also found in AF-ferrimagnetic and ferrimagnetic-FM interfaces. Further references on particular EB systems can be found in [63,64].

In the last decade a growing interest was initiated by possible applications of the EB effect in thin films at room temperature. Today, exchange biased domain stabilizers in magnetoresistive reading heads for hard-disks and exchange biased pinning layers for spin valve systems exhibiting giant magnetoresistance (GMR) or tunnelling magnetoresistance (TMR) are widely used. An example for a spin valve device is shown in Fig. 5.2. The magnetization direction of the lower permalloy layer is pinned to the AF layer. When an electrical current is passed through the layers a magnetoresistance effect is observed when the top permalloy layer's magnetization direction is reversed.

In a simplified model, an ideal flat surface of an antiferromagnet is coupled to a ferromagnetic layer on top. The spins of the AF are aligned unidirectionally along a single axis, the anisotropy axis of the AF. The surface of the AF is uncompensated, i.e. a net magnetization is present. In contradistinction, for a compensated surface the net magnetization is zero on a microscopic length scale. The anisotropy axis of the FM is parallel to the AF axis.

A schematic view of the configuration is shown in Fig. 5.3: at $T_\mathrm{N} < T < T_\mathrm{C}$ a magnetic field is applied along the anisotropy axis of the AF layer (1). The FM spins align along the field axis while the AF spins are still disordered. The

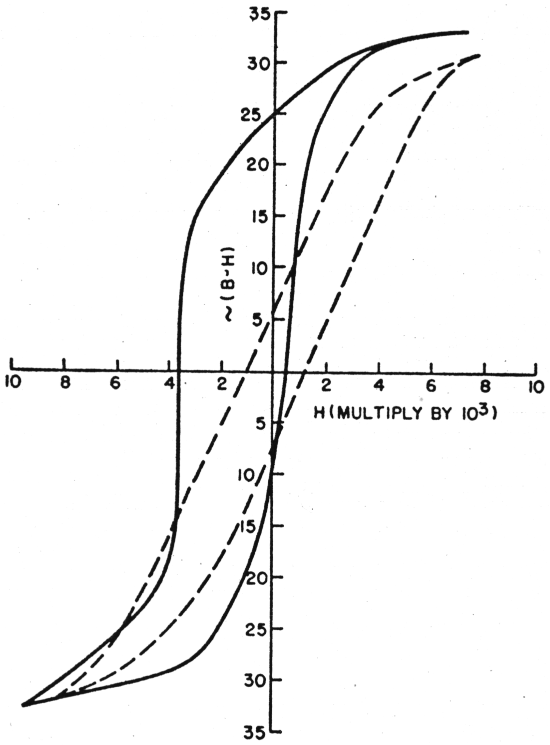

Figure 5.1: Exchange bias of Co/CoO in small particles as found by Meiklejohn and Bean [60]. The full curve shows a hysteresis loop at $T = 77\,\mathrm{K}$ after cooling in a saturating magnetic field. The dashed curve was obtained without field cooling.

sample is cooled to $T < T_\mathrm{N}$ with the field still applied (field cooling). Assuming FM coupling, the AF interface spins align along the FM interface spins and the AF orders with this interface constraint (2). Now a hysteresis loop can be performed: starting from a positive magnetic saturated state the field is reduced and finally reversed. Typically, the anisotropy of the AF, quantified by the anisotropy constant K_AF, is large and the spins of the AF remain essentially fixed. The interface coupling is assumed to be much weaker. The interface spins of the FM are (weakly) coupled to the AF interface spins and (strongly) coupled to the other FM spins. Thus, the torque exerted by the magnetic field on the FM layer is partially compensated by the interface coupling resulting in a spin reversal of the FM layer at a lower field as compared to the decoupled case (3). While increasing the field from the reversed saturated magnetic state (4) a continuous torque due to the interface coupling causes the spin reversal again to occur at a lower field (5). As a result the whole hysteresis loop is shifted by the exchange bias field H_EB to the opposite direction of $\vec{H}_\mathrm{FC}$. The behavior of the coercivity depends on the anisotropy of the AF: if it is small, the interface spins of the AF are dragged along with the FM spins, thus enhancing coercivity. If the anisotropy is very

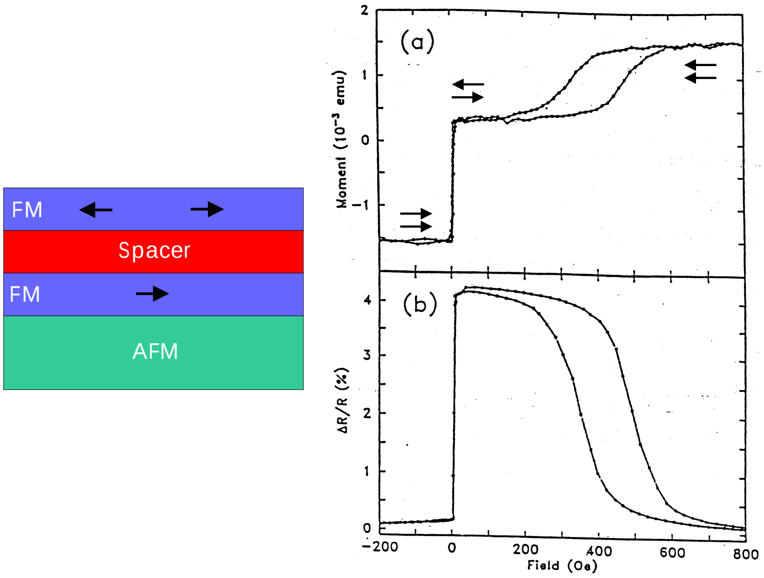

Figure 5.2: Left: Schematic diagram of a spin valve device. The topmost softmagnetic layer can easily be switched by a magnetic field, indicated by the double arrows. Right: Magnetic hysteresis loop (top) and magnetoresistance (bottom) of a GMR spin valve with $Fe_{20}Ni_{80}/Cu/Fe_{20}Ni_{80}/FeMn$ layering [65].

large, the interface spins decouple and the coercivity is not enhanced [63]. Usually, an increased coercivity can be observed corresponding to an intermediate behavior. In many experiments a reduced blocking temperature $T_\mathrm{B} < T_\mathrm{N}$, above which the EB effect vanishes, is observed. This is due to finite size effects in AF grains or AF layers in thin films [66]. The energy barrier for thermally activated spin reversal in a grain is proportional to the grain volume V [64]. For further references see [63].

The unidirectional anisotropy of an exchanged biased system can be measured directly by torque magnetometry. In addition to the uniaxial anisotropy indicated by a $\sin^2\theta$ component if the external field is set to $H_\mathrm{ext} > H_\mathrm{C}$, the torque signal exhibits a $\sin\theta$ component [63]; θ is the angle between the external field and the anisotropy axis of the AF/FM. An example for a torque curve of an oxidized Co layer is shown in the left of Fig. 5.4. The torque has an absolute minimum corresponding to $\theta = 0\,°$. If the torque loop is performed in the opposite direction a hysteresis is generated. The area W_R of this rotational hysteresis is twice the energy loss during the rotation cycle. In contradistinction to FM systems, which exhibit such a hysteresis only in a narrow range of the applied field, a high field W_R is typically found for exchange biased systems due to the torque of the FM layer exerted on the AF layer during rotation [63], as can be seen on the right of Fig. 5.4.

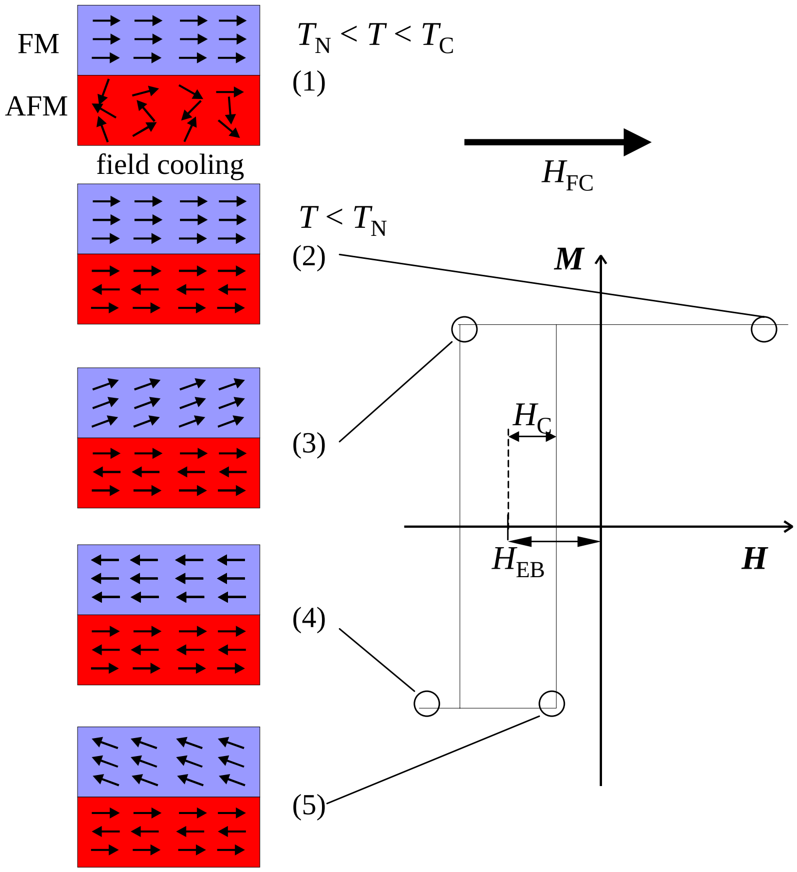

Figure 5.3: Simplified scheme of an exchanged biased system. The direction of the cooling field is as indicated. The left side sketches the magnetization directions at different stages of the hysteresis loop.

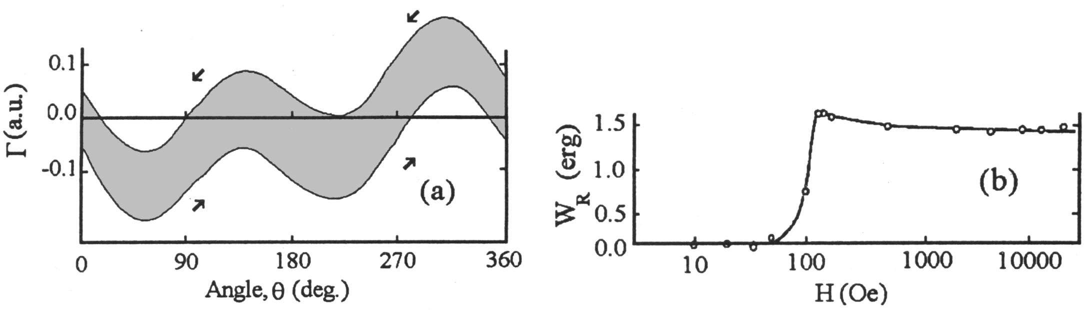

Figure 5.4: Left: Magnetization induced torque Γ for forward and backward rotation. The shaded area is twice the energy loss W_R during the cycle. Right: Energy loss W_R depending on the applied field. Both curves were obtained for an oxidized Co film [67].

In a simple Heisenberg exchange model the energy per unit area ϵ is described by [62]

$$\begin{aligned}\epsilon &= -H_{\mathrm{ext}}M_{\mathrm{FM}}t_{\mathrm{FM}}\cos(\theta-\beta)+K_{\mathrm{FM}}t_{\mathrm{FM}}\sin^2(\beta)+\\ &\quad +K_{\mathrm{AF}}t_{\mathrm{AF}}\sin^2(\alpha)+J_{\mathrm{Int}}\cos(\beta-\alpha)\end{aligned}\tag{5.1}$$

H_{ext} is the applied magnetic field, M_{FM} the saturation magnetization of the FM layer, t_{FM} the thickness of the FM layer, K_{FM} the anisotropy constant of the FM layer, K_{AF} the anisotropy constant of the AF layer, t_{AF} the thickness of the AF layer and J_{Int} the interface coupling constant. The angles are as illustrated in Fig. 5.5.

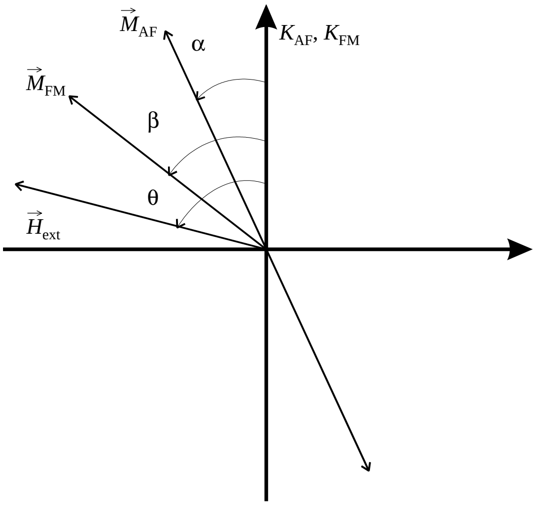

Figure 5.5: Angles between the collinear anisotropy axis of the FM and AFM with the anisotropy constants K_{FM} and K_{AF}, the external field $\vec{H}_{\mathrm{ext}}$, the magnetization of the FM layer $\vec{M}_{\mathrm{FM}}$ and the magnetization of the AF layer $\vec{M}_{\mathrm{AF}}$.

The first term describes the Zeeman energy of the FM layer in the external field. The second and third term account for the anisotropy of the FM and AF layer, respectively. These are assumed to be collinear. The last term introduces the coupling energy of the AF/FM interface J_{Int}. A further simplification may be achieved by neglecting the FM anisotropy energy: $K_{\mathrm{FM}}t_{\mathrm{FM}} \ll K_{\mathrm{AF}}t_{\mathrm{AF}}$, as frequently found in experiments [62,63]. Consequently, equation 5.1 simplifies to

$$\epsilon = -H_{\mathrm{ext}}M_{\mathrm{FM}}t_{\mathrm{FM}}\cos(\theta-\beta)+K_{\mathrm{AF}}t_{\mathrm{AF}}\sin^2(\alpha)+J_{\mathrm{Int}}\cos(\beta-\alpha)\tag{5.2}$$

After minimizing this energy with respect to α and β the loop shift H_{EB} is found to be [62]

$$H_{\mathrm{EB}} = \frac{J_{\mathrm{Int}}}{M_{\mathrm{FM}} t_{\mathrm{FM}}} \tag{5.3}$$

Thus, for a given system $H_{\mathrm{EB}} \propto t_{\mathrm{FM}}^{-1}$. Equation 5.3 also predicts that for an EB effect the following condition must be fulfilled [62]

$$K_{\mathrm{AF}} t_{\mathrm{AF}} \geq J_{\mathrm{Int}} \tag{5.4}$$

If this rule is not fulfilled the AF layer is rotated coherently with the FM layer due to the interface coupling. No EB effect should be observed, but an increase of coercivity.

Due to its interface origin the EB is often quantified as energy per unit area:

$$\Delta\epsilon = M_{\mathrm{FM}} t_{\mathrm{FM}} H_{\mathrm{EB}} \tag{5.5}$$

In the model described above several simplifying assumptions were made. In particular, the anisotropy of the layers were assumed to be uniaxial and parallel. Generally, additional crystalline anisotropies are found in crystalline layers which complicate the behavior. AF domains were found to be important for the EB which cannot be handled within the given model (see references in [63]). Since the coupling constant J_{Int} is assumed to correspond to FM coupling [62], experiments proving an AF [68] or 90° coupling (further references in [63]) cannot be explained within this model. Furthermore, if a Heisenberg like exchange coupling at the interface is assumed, J_{Int} should be chosen similar to the coupling constants in FM materials. This yields an H_{EB} which is two orders of magnitude larger than observed. Finally and probably most importantly, the AF surface is assumed to be uncompensated. No simple theoretical treatment of compensated surfaces is possible, though many apparently compensated surfaces are found to exhibit an EB of the same magnitude as uncompensated surfaces (for a list of experimentally determined H_{EB} see [63]). The low magnitude of the coupling for compensated surfaces was recently explained for $\mathrm{Ni_{81}Fe_{19}/CoO}$ bilayers within a model incorporating AF grains with small contributions of uncompensated spins and surface roughness [69]. According to this model the EB for interfaces that are presumably completely compensated is generated by small regions of uncompensated spins induced by the field cooling. The prediction of the magnitude for the EB is quantitatively compatible with a Heisenberg exchange coupling between AF and FM layers. However, no clear-cut experiment for the nature of the coupling is presently available.

5.1.2 Magnetic susceptibility of the (110)-textured sample

The (110)-textured sample was measured with the magnetic field in-plane. In this geometry demagnetization effects can be neglected. The demagnetization tensor N_{ij} is defined via a demagnetization field $\vec{H}_{\mathrm{demag}}$ [70]

$$\vec{H}_{\mathrm{demag}} = -N_{ij}\vec{M} \tag{5.6}$$

For a two-dimensional infinitely stretched plate, which is an approximation to thin films, all tensor elements referring to a demagnetization field direction within the film plane are zero. The perpendicular demagnetizing field is only depending on M_z [71]:

$$N_{ij} = \begin{pmatrix} N_{xx} = 0 & N_{xy} = 0 & N_{xz} = 0 \\ N_{yx} = 0 & N_{yy} = 0 & N_{yz} = 0 \\ N_{zx} = 0 & N_{zy} = 0 & N_{zz} = 1 \end{pmatrix} \tag{5.7}$$

Thus, the so-called shape anisotropy of a thin film promotes an easy-plane behavior. For $\mathrm{TiFe_2}$ the uniaxial magnetocrystalline anisotropy axis points along the c-axis direction (see Fig. 1.1). Consequently, for (110)-textured films the c-axis is parallel to the film plane and an easy axis-behavior is expected with the magnetic field in-plane.

Temperature-dependent magnetization measurements were performed for different cooling fields (Fig. 5.6). The sample was either cooled in the specified magnetic field (field cooled, FC) or in zero field (zero field cooled, ZFC) from $T = 280\,\mathrm{K}$ to $5\,\mathrm{K}$. The FC curves were taken during cool down at the indicated aligning field. The ZFC curves were obtained during warm up.

For the lowest cooling field ($\mu_0 H_{\mathrm{FC}} = 3\,\mathrm{mT}$) the magnetization increases with decreasing temperature corresponding to ferromagnetic behavior (see hysteresis in Fig. 5.8 and Fig. 5.12). At $T \approx 140\,\mathrm{K}$ a pronounced maximum is followed by a magnetization drop of 45%. This decrease is due to increasing antiferromagnetic order in the sample and saturates at low temperatures. The shape of the curve is very similar to those obtained for antiferromagnets if a small aligning field is applied parallel to the anisotropy axis [72]. The temperature of the $M(T)$ maximum is identified as the Néel temperature T_{N} of AF ordered regions in the sample.

However, the magnetization does not vanish for low temperatures due to FM ordered regions in the sample, as will be shown in section 5.1.3. The magnetization drop can partly be suppressed by increasing the cooling field: for $\mu_0 H_{\mathrm{FC}} = 49\,\mathrm{mT}$ a plateau is still visible for low temperatures. The magnetization follows for $\mu_0 H_{\mathrm{FC}} = 500\,\mathrm{mT}$ an almost FM-like curve, but deviations from Bloch's law at low temperatures still indicate antiferromagnetic contributions

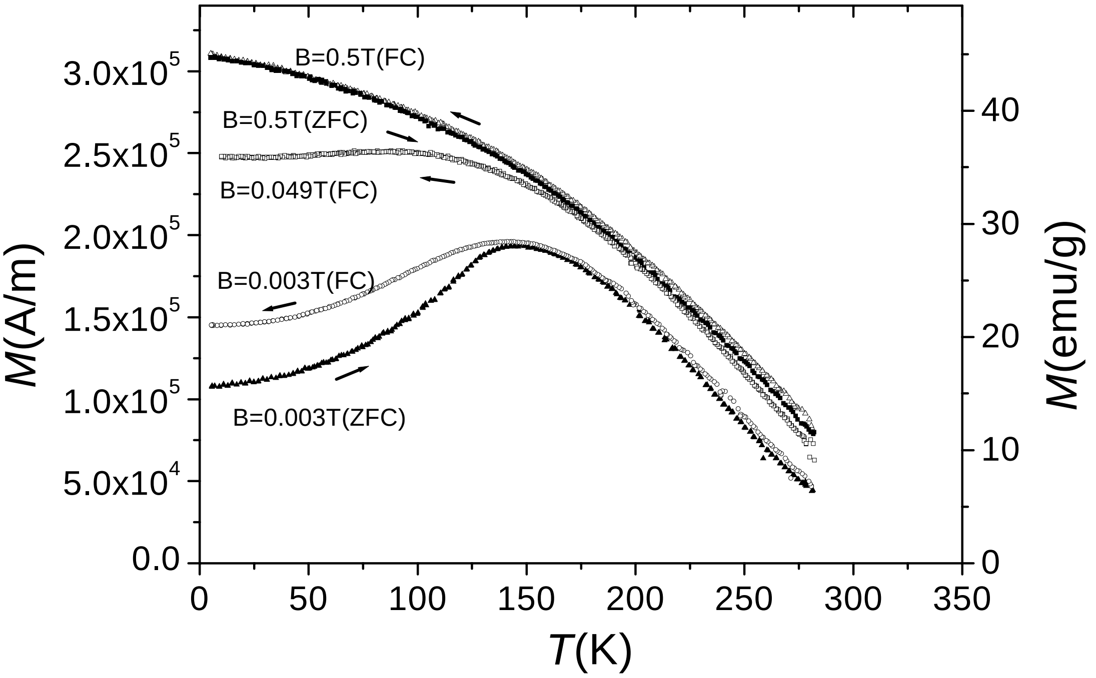

Figure 5.6: Temperature-dependent magnetization curves obtained for the sample with $x = 0.32$ and $\mathrm{TiFe_2}(110)$ texture. The direction of the temperature gradient is indicated by arrows. The corresponding applied magnetic field for field cooled (FC) and zero field cooled (ZFC) measurements is as indicated.

(see Fig. 5.7). The minimum field necessary for the suppression of antiferromagnetic signatures in $M(T)$ is a coarse measure for the antiferromagnetic exchange field and the strength of magnetism. In the present case the rather low field $\mu_0 H_{\mathrm{ext}} \leq 0.5\,\mathrm{T}$ indicates a weak antiferromagnetism for most AF regions of the sample. Furthermore, the curves are shifted to higher magnetization values for higher aligning fields H_{ext} which is due to an additional magnetization induced by H_{ext} in regions initially not being FM.

A comparison of the FC and the ZFC curves reveals that for the lowest cooling field $\mu_0 H_{\mathrm{FC}} = 3\,\mathrm{mT}$ the ZFC curve lies significantly below the FC curve at low temperatures. Both curves collapse on one curve at T_{N}. It may be assumed that during field cooling regions that order antiferromagnetically are aligned along the field direction and are frozen by exchange coupling to neighbored ferromagnetic regions below T_{N}. T_{C} of the ferromagnetic regions can be estimated by extrapolating the low cooling field curve to zero magnetization at high temperatures. This gives T_{C} in the range of 310 to 320 K. The experimental setup limits the accessible temperature range to below the Curie point.

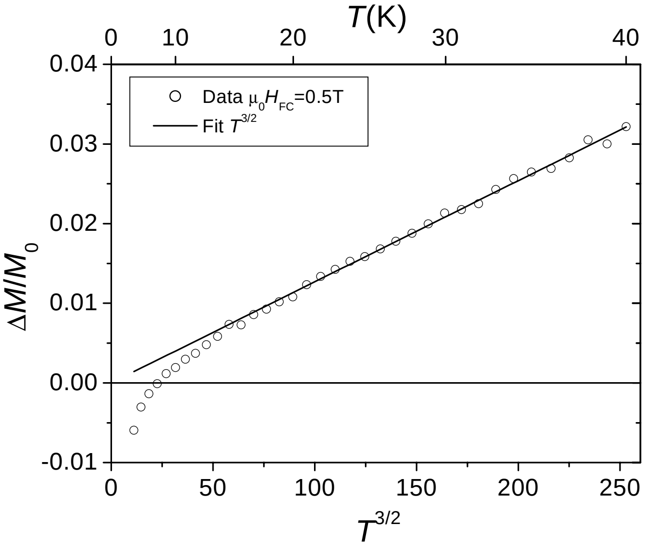

Figure 5.7: $T^{3/2}$ fit to the high temperature Bloch-like region. The low temperature deviations are due to residual AF regions.

5.1.3 Magnetic isotherms

Several magnetic isotherms (hysteresis loops) with different cooling fields were measured at $T = 5\,\mathrm{K}$, as depicted in Fig. 5.8.

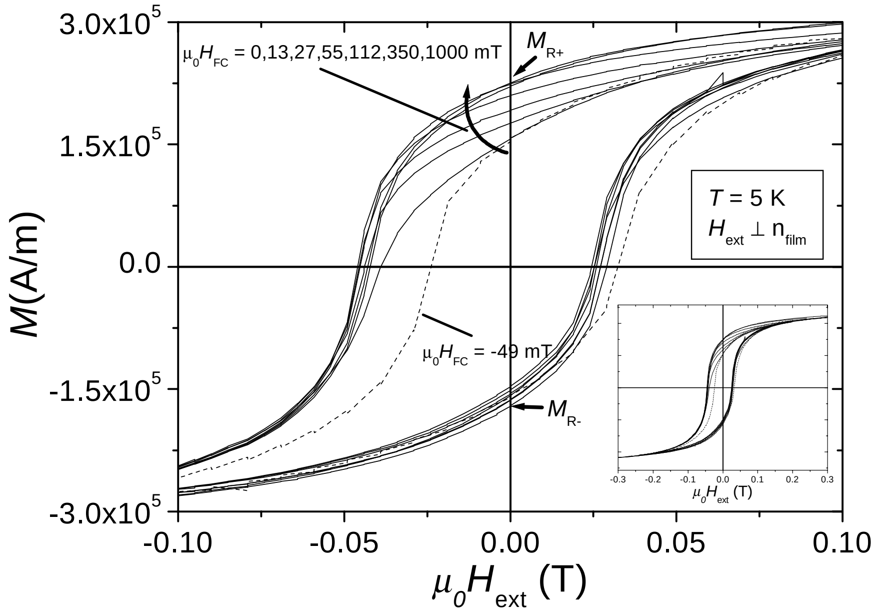

Figure 5.8: Magnetic hysteresis loops taken at $T = 5\,\mathrm{K}$ for the (110)-textured sample. H_{FC} was set as indicated (solid lines). For the dashed curve the cooling field was set to -49 mT.

Prior to the measurements the sample was warmed up to $T = 280\,\mathrm{K}$ in zero field and then cooled in the specified cooling field. An initial magnetization curve could not be measured for each loop due to the limited accessible temperature range $T < 285\,\mathrm{K}$. The sample was not treated thermally outside the magnetometer to keep its structural integrity. The loops were taken starting from the magnetic saturated state at the maximum positive field $\mu_0 H_{\mathrm{max}} \geq 0.2\,\mathrm{T}$. Subsequently, the field was cycled through the maximum negative field (decreasing field branch) and back to the maximum positive field (increasing field branch).

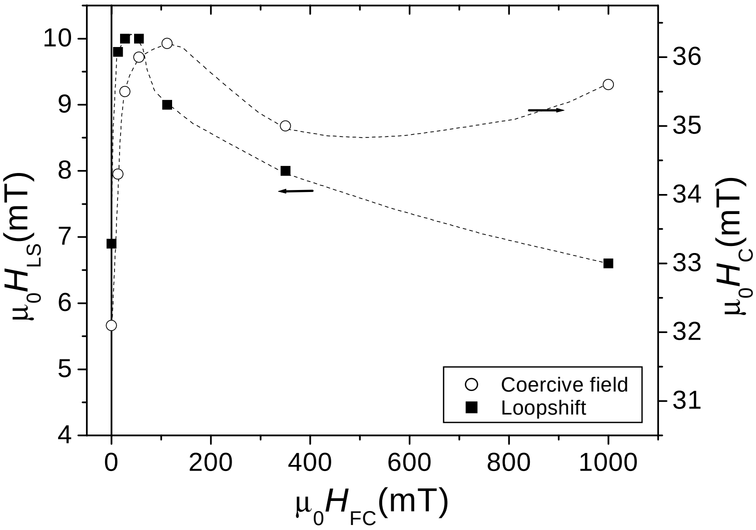

Figure 5.9: The shifting field H_{LS} (full squares) and the coercive field H_{C} (open circles) of the (110)-textured sample as determined from the hysteresis loops shown in Fig. 5.8. Dashed lines to guide the eye.

Generally, all the hysteresis loops exhibit ferromagnetic easy axis behavior with coercive field and remnant magnetization. In the as-taken loops a linear diamagnetic contribution is superimposed on the magnetization. This is caused by the $\mathrm{Al_2O_3}$ substrate. After the determination of the sample volume this contribution was subtracted using the average density ($\rho = 3.7\,\mathrm{g/cm^3}$) and the molar susceptibility of crystalline $\mathrm{Al_2O_3}$ ($\chi_m = -3.7 \cdot 10^{-6}$) found in the literature [73]. As a common feature all loops exhibit a unidirectional anisotropy in the hysteresis loop which is shifted opposite to the applied cooling field H_{FC}. An inversion of the cooling field causes the loop-shift to change its direction (dashed curve). This clearly suggests exchange-biasing in the sample. In this context, the pronounced rounding of ideally rectangular easy axis loops may be generated by domain wall motion and a superposition of loops with different H_{LS}. The evaluation of the shifting field H_{LS} and coercive field H_{C} reveals maxima for $\mu_0 H_{\mathrm{FC}} \simeq 40\,\mathrm{mT}$ and $\mu_0 H_{\mathrm{FC}} \simeq 100\,\mathrm{mT}$, respectively (Fig. 5.9). This will be further discussed in section 5.1.4.

Additionally, an asymmetry of the remnant magnetization $M_{\mathrm{R+}}$ in the decreasing field branch and $M_{\mathrm{R-}}$ in the increasing field branch can be observed. This asymmetry changes continuously with H_{FC}, as depicted in Fig. 5.10. While $M_{\mathrm{R-}}$ stays constant, $M_{\mathrm{R+}}$ is lower than $M_{\mathrm{R-}}$ for $\mu_0 H_{\mathrm{FC}} \leq 27\,\mathrm{mT}$ and higher for larger H_{FC} . $M_{\mathrm{R+}}$ saturates at $\mu_0 H_{\mathrm{FC}} \simeq 100\,\mathrm{mT}$. A possible explanation for the observed asymmetry can be deduced from the assumption that the hysteresis loops are generated by an incoherent superposition of elementary loops differing in their coercive field while exhibiting a loop-shift in the same direction. In this way, a crossover of the asymmetry function $\Delta R_{\mathrm{M}} = M_{\mathrm{R+}} - M_{\mathrm{R-}}$ for two loops with coercive field H_{C1} and H_{C2} with $H_{\mathrm{LS1}} < H_{\mathrm{LS2}}$ occurs. For constant H_{C1}, $\Delta R_{\mathrm{M}} < 0$ if $H_{\mathrm{C2}} > H_{\mathrm{C1}}$ and $\Delta R_{\mathrm{M}} > 0$ if $H_{\mathrm{C2}} < H_{\mathrm{C1}}$. For an illustration see Fig. 5.11.

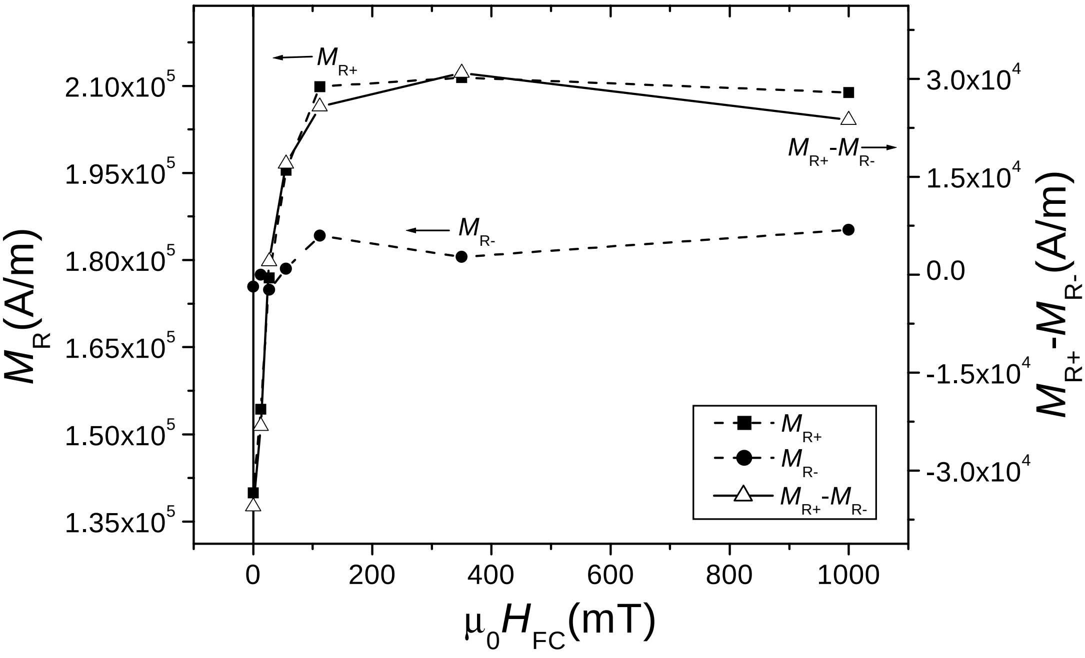

Figure 5.10: Remnant magnetization of the decreasing branch $M_{\mathrm{R+}}$ and the increasing branch $M_{\mathrm{R-}}$ (full symbols). The difference $M_{\mathrm{R+}} - M_{\mathrm{R-}}$ is a measure of the asymmetry of the hysteresis loops in Fig. 5.8 (open symbols). The values of $M_{\mathrm{R+}}$ and $M_{\mathrm{R-}}$ were taken after displacing the hysteresis loops of Fig. 5.8 by $\mu_0 H_{\mathrm{LS}}$.

However, since H_{C} and H_{LS} are correlated, in the present case probably in a complicated manner, an exact analysis remains difficult. Nevertheless, this behavior is obviously generated by the exchange bias. The given explanation is only valid if dipolar coupling between the FM regions can be neglected, i.e. the FM regions are sufficiently separated.

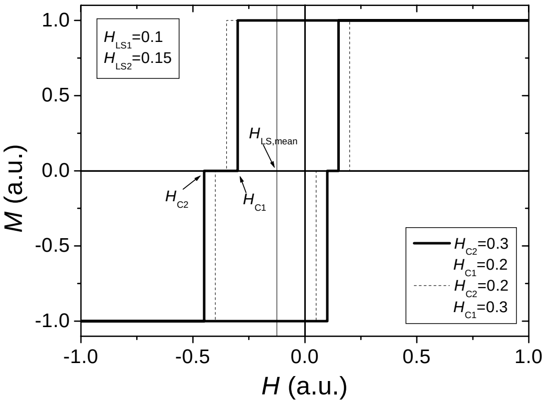

Figure 5.11: Illustration of the hysteresis loop asymmetry model for ideal rectangular loops. The parameters were set as indicated.

In Fig. 5.12 field cooled ($\mu_0 H_{\mathrm{FC}} = 49\,\mathrm{mT}$) hysteresis loops are compared. At temperatures of about 100 K and above the loop-shift disappears within the resolution of the data points. In the vicinity of T_{N} the pinning of the FM regions by the AF regions in the sample is strongly reduced and vanishes completely for $T > T_{\mathrm{N}}$ as can be seen in Fig. 5.13.

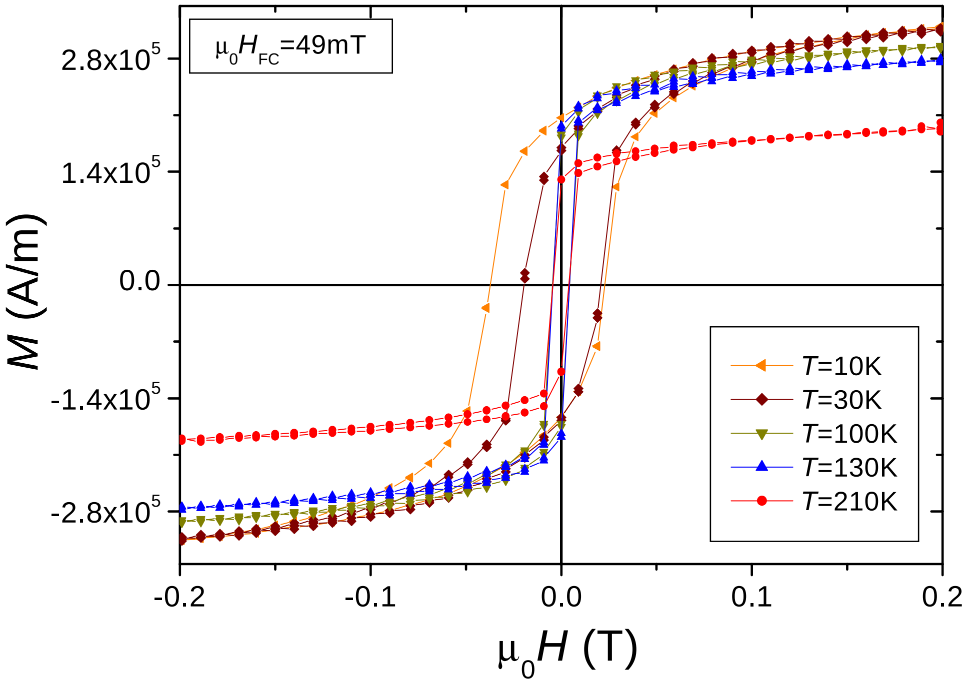

Figure 5.12: Dependence of magnetic hysteresis loops on the temperature for the (110)-textured sample. The loops were taken after field cooling with $\mu_0 H_{\mathrm{FC}} = 49\,\mathrm{mT}$.

The coercive field exhibits the same behavior: as the exchange coupling between the FM and AF regions disappears for $T \geq T_\mathrm{N}$ the coercivity is strongly reduced due to the absent exchange biasing. The values obtained for H_C at $T \geq 100$ K are close to zero. The temperature dependence of H_LS and H_C underlines the exchange-bias-like behavior.

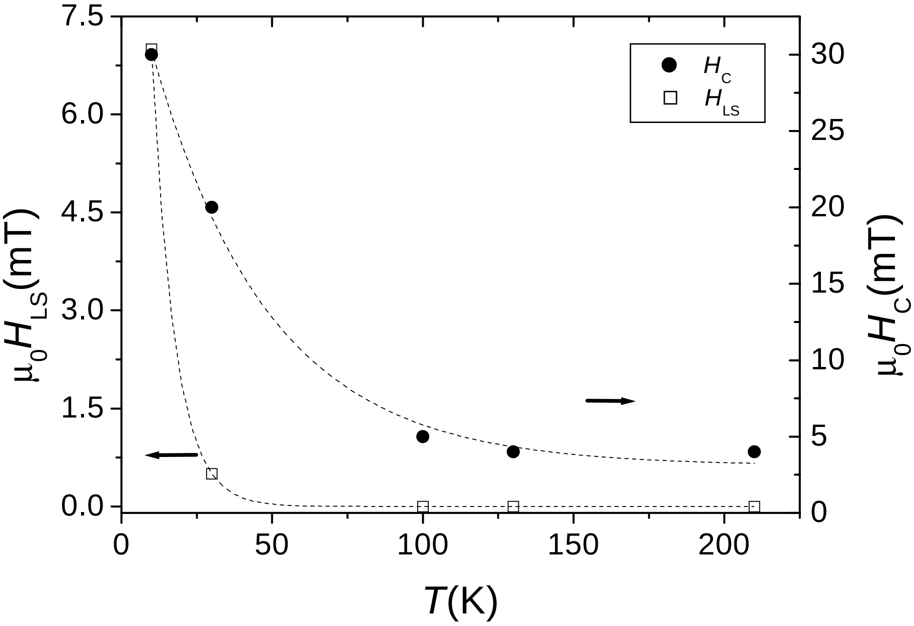

Figure 5.13: Loop shift field H_LS (open squares) and coercive field H_C (full circles) vs. temperature taken from the data of Fig. 5.12. Dashed lines to guide the eye.

Finally, in Fig. 5.14 the saturation magnetization M_S determined at $\mu_0 H_\mathrm{ext} = 0.2\,\mathrm{T}$ and the coercive field H_C, as determined from Fig. 5.12, are compared. M_S decreases with increasing T as the sample temperature approaches T_C. However, since H_C vanishes for $T \geq T_\mathrm{N}$ the decrease of H_C must also be related to the exchange biasing which disappears above T_N. In contradistinction, M_S is related to the FM regions with $T_\mathrm{C} \approx 310$ to $320\,\mathrm{K}$ (see section 5.1.2).

5.1.4 Discussion

The presented magnetization data suggest the coexistence of antiferromagnetic and ferromagnetic regions in the polycrystalline sample. For low H_FC the strong decrease of the susceptibility below 140 K indicates AF behavior, reminiscent of $\chi_\parallel$ of a classical AF like $\mathrm{MnF_2}$ [72]. The background susceptibility at low temperatures and the shape of the hysteresis loops indicate FM contributions with $T_\mathrm{C} \approx 310$ to $320\,\mathrm{K}$. The AF state is easily suppressed by aligning fields as low as

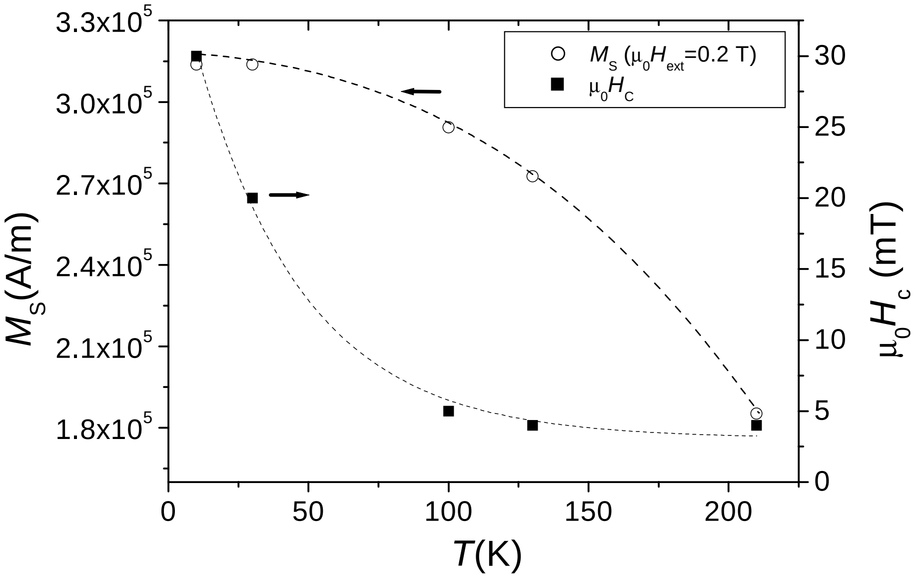

Figure 5.14: Saturation magnetization M_S at $\mu_0 H_\mathrm{ext} = 0.2\,\mathrm{T}$ (open circles) and coercive field H_C (full squares) vs. temperature taken from the data of Fig. 5.12. Dashed lines to guide the eye.

50 mT indicative of weak antiferromagnetism. A similar interpretation was given by Wassermann et al. [11] for $M(T)$ curves of polycrystalline Fe-Ti bulk samples that contained small iron inclusions in a $\mathrm{TiFe_2}$ matrix. In contrast to the thin film data the AF coupling in the bulk samples is much stronger and is not suppressed by an aligning field as large as 1 T. As for the examined thin film sample, the low deposition temperature allows for the formation of the parasitic TiFe phase. Thus, the $\mathrm{TiFe_2}$ phase is expected to be iron-rich. This is also suggested by a slightly reduced lattice constant as found in the X-ray data (see Fig. 3.2 and chapter 6). The present data suggest that the coexistence of inhomogeneous $\mathrm{Ti}_x\mathrm{Fe}_{1-x}$ in the C14 stability range partly being AF and FM induces an exchange bias coupling at the respective interfaces (see section 1.2.3). The formation mechanism and the shape of these regions was not systematically studied, but the size of these regions seems to be smaller than in [11] and in epitaxial films (see chapter 6). This is indicated by the smaller AF ordering temperature T_N. The increased surface to volume ratio promotes the exchange bias which is significantly larger than in epitaxial films. The competition of ferromagnetic alignment in the FM ordered regions and the suppression of the weak antiferromagnetism in the AF regions with increasing H_FC are assumed to lead to the maximum observed in H_LS and H_C vs. H_FC. This is supported by the $M(T)$ measurements: A mixed AF and FM behavior is noticeable at lower temperatures and low cooling fields which is partly suppressed by applying larger cooling fields, whereas at elevated temperatures above T_N a FM-type magnetization curve was obtained.

5.2 Magnetoresistance of textured thin films

5.2.1 Introductory remarks

In addition to magnetization measurements of magnetic samples the electronic transport properties may yield further insight into the magnetic configuration of differently ordered regions. Especially for the sample analyzed in section 5.1, the unidirectional anisotropy connected to the interfaces of AF/FM ordered regions may be manifested in the transport properties. Several magnetoresistive effects can be observed in magnetic samples exposed to an external magnetic field. Beside the intrinsic magnetoresistivity in metals due to the Lorentz force acting on the conduction electrons [74,75] (see Fig. 5.15a) an anisotropic magnetoresistance (AMR) is often observed in ferromagnetic alloys. In this case the behavior of the resistivity as a function of the magnetic field strongly depends on the orientation of the current with respect to the magnetic field. Smit [76] explained this symmetry break by the spin-orbit (SO) interaction which couples the spin to the crystal lattice via the electron's orbital motion. Simply stated, the SO interaction causes a mixing of spin-up and spin-down states with unoccupied states in the d-bands of magnetic d-metals into which mainly s-electrons (Mott model) may be scattered. The effective scattering cross section for the s-electrons into unoccupied d-states depends on the relative orientation of the magnetization direction and the current. The cross sections themselves depend on the local symmetry of the d-state into which the scattering occurs. The area of the d-orbital perpendicular to the current may give an estimate of this scattering cross section. Typically, the specific resistivity $\rho_{\|}$ parallel for the current being aligned parallel to the field is larger than the resistivity $\rho_{\perp}$ for the current perpendicular to the field (see Fig. 5.15). The anisotropy is expressed as the spontaneous resistivity anisotropy (SRA) which is the anisotropy normalized to the resistivity in the demagnetized state [74]:

$$SRA = \frac{\rho_{\|} - \rho_{\perp}}{\frac{\rho_{\|}}{3} + \frac{2\rho_{\perp}}{3}} \tag{5.8}$$

Another effect, observed only in ferromagnetic materials, is caused by the electronic band splitting in conjunction with spin-dependent scattering. The electronic density of states (DOS) of ferromagnets below T_{C} is separated into a spin-up (majority) and a spin-down (minority) band by the exchange interaction. At sufficiently low temperatures the probability of spin-flip scattering processes induced by magnons is very low. Thus, the specific resistivity ρ_{LT} can be described by parallel conduction in two channels with the respective specific resistivities $\rho_{\uparrow}$ and $\rho_{\downarrow}$ for majority and minority electrons:

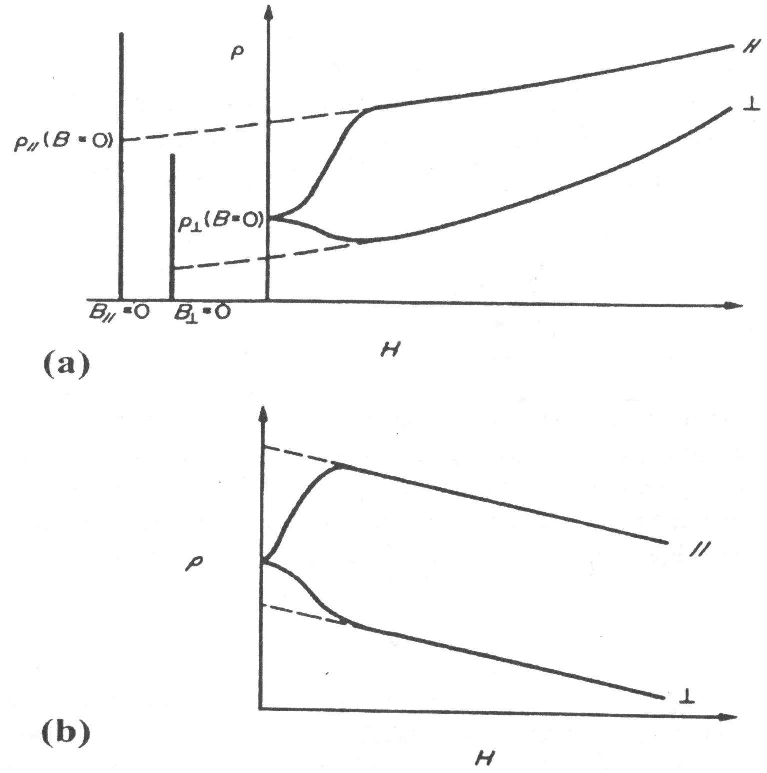

Figure 5.15: (a) Magnetic field-dependent specific resistivity $\rho_{\|}$ and $\rho_{\perp}$ for the current parallel and perpendicular to the field, respectively. The sample exhibits an AMR effect combined with a normal MR effect (see text) (b) $\rho_{\|}$ and $\rho_{\perp}$ for a sample exhibiting an AMR and a reduction of the spin-disorder resistivity [77].

$$\rho_{\mathrm{LT}} = \frac{\rho_{\uparrow}\rho_{\downarrow}}{\rho_{\uparrow} + \rho_{\downarrow}} \tag{5.9}$$

According to Fermi's Golden Rule the scattering probability and thus the resistivity is proportional to the DOS [78]:

$$\rho_{\sigma} \propto n_{\sigma}(E_{\mathrm{F}}) \tag{5.10}$$

With the spin-dependent DOS $n_{\sigma}(E_{\mathrm{F}})$ at the Fermi level E_{F}, ρ_{σ} is spin-dependent, too. Typically, for ferromagnetic alloys $n_{\uparrow}(E_{\mathrm{F}})$ is significantly lower than $n_{\downarrow}(E_{\mathrm{F}})$ thus shuntening the majority spin channel and reducing the overall resistivity according to equation 5.9. This effect is known as "freezing out" of spin disorder resistivity. This lowering of the resistivity is connected to the magnetic ordering below T_{C} as shown for Ni in Fig. 5.16.

Additionally, the application of a magnetic field results in a further decrease of the spin disorder, reducing ρ with increasing field. Due to the origin of the spin

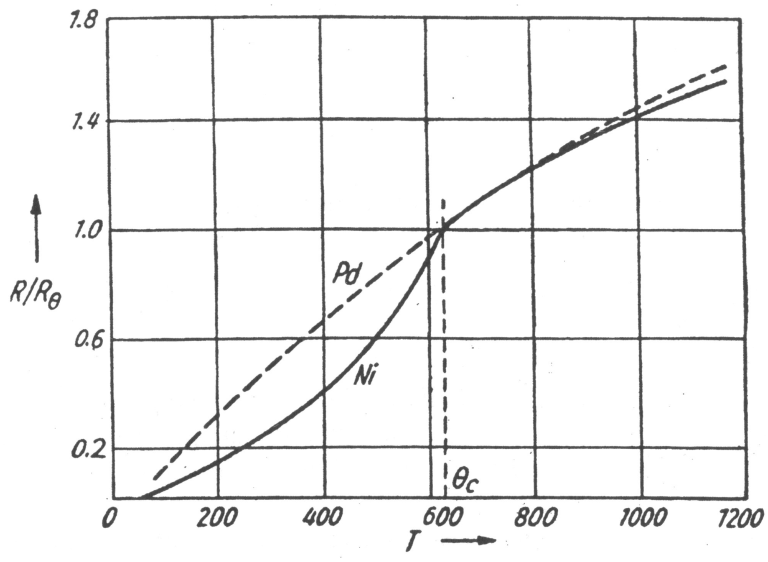

Figure 5.16: Normalized resistance of Ni and paramagnetic Pd [79]. The pronounced decrease of R_{Ni} below θ_{C} is due to the "freezing out" of spin disorder scattering.

disorder resistivity the effect is completely isotropic with regard to the magnetic field. An analogous description can be applied to the Giant Magnetoresistance (GMR) effect [80,81]. This effect can be observed for structures consisting of regions with different magnetic alignment to each other, such as AF coupled layered structures [82]. In this case, the resistivity is reduced if an external field aligns the regions parallel, corresponding to the ordered state as mentioned above. The GMR effect does not depend on the direction of the current with respect to the magnetic field, either.

5.2.2 Magnetoresistance in (110)-textured samples

Temperature- and magnetic field-dependent measurements were performed in an Oxford Instruments cryostat with liquid ^{4}He cooling. The temperature was controlled by a Lakeshore controller with a Pt100 sensor. The sample temperature was measured by a CGR thermometer mounted next to the sample. The (110)-textured thin film (see section 5.1) was contacted by Cu-wires attached to the film surface with small dots of silver paint in the four corners of the square sample surface. The external magnetic field was aligned parallel to the film plane. The resistance was measured in a four-point geometry avoiding effects of the contact resistance. In this arrangement two parallel pairs of contacts (current and voltage) along the edges were perpendicular or parallel to the field allowing for the measurement of both transverse resistance $R_\perp$ and longitudinal resistance $R_\parallel$, respectively. The thermovoltage was eliminated by reversing the current and averaging over the two voltages. The current was in the range $0.7\,\mathrm{mA} \leq I \leq 1.0\,\mathrm{mA}$, depending on the voltage stability in the respective temperature range. The noise was minimized by averaging over several data points taken under fixed parameter conditions.

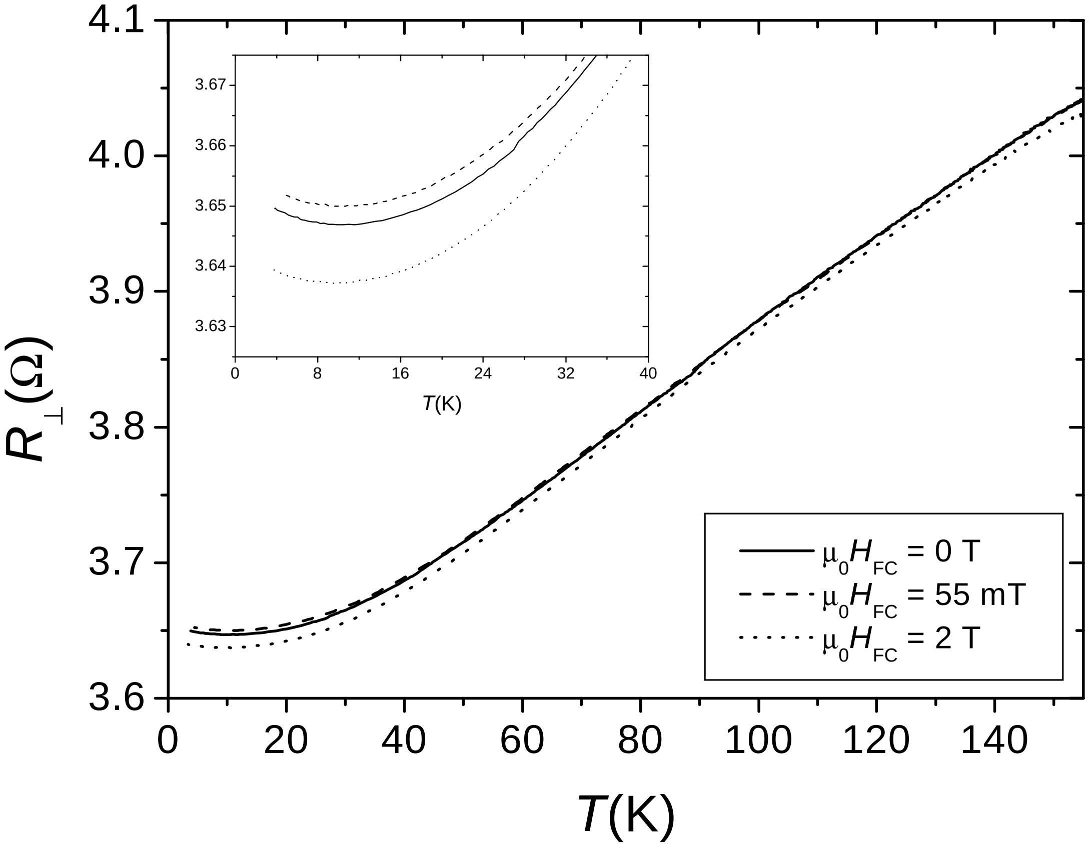

Figure 5.17: Transverse resistance of the (110)-textured sample. Three different cooling fields $\mu_0 H_{\mathrm{FC}}$ corresponding to the remnant state at 0 mT, an at low temperatures non-saturated state at 55 mT and the completely saturated state at 2 T.

Fig. 5.17 shows the temperature-dependent transverse resistance of the (110)-textured sample for different cooling fields H_{FC}. All curves exhibit an almost linear behavior between $T = 158\,\mathrm{K}$ and $T \approx 40\,\mathrm{K}$, corresponding to phonon induced scattering. Below $T \approx 40\,\mathrm{K}$ a deviation from linear behavior is observed followed by a slight increase of the resistance below $T \approx 10\,\mathrm{K}$, as observed in Kondo-like systems. The residual resistance is indicative of the large number of grain boundaries in the polycrystalline sample. The curves for different cooling fields correspond to the remnant state at $\mu_0 H_{\mathrm{FC}} = 0\,\mathrm{mT}$, an at low temperatures non-saturated state (see Fig. 5.12) at $\mu_0 H_{\mathrm{FC}} = 55\,\mathrm{mT}$ and the completely saturated state at $\mu_0 H_{\mathrm{FC}} = 2\,\mathrm{T}$. At lower temperatures the 55 mT curve exhibits a slightly increased resistance as compared to the ZFC curve. This is possibly caused by the effect of the AMR during the orientation of the magnetization with increasing field and the normal MR effect observed in metals (see section 5.2.1). The resistance in the 2 T-curve is appreciably lower over the complete temperature range with the difference to the other curves increasing at lower temperatures. This indicates the reduction of the spin disorder resistivity of the FM ordered regions with increasing field. A GMR effect due to the current passing AF and FM ordered regions can be excluded because the effect should vanish above $T_N \approx 140\,\mathrm{K}$ of the AF ordered regions, in contradistinction to the observation.

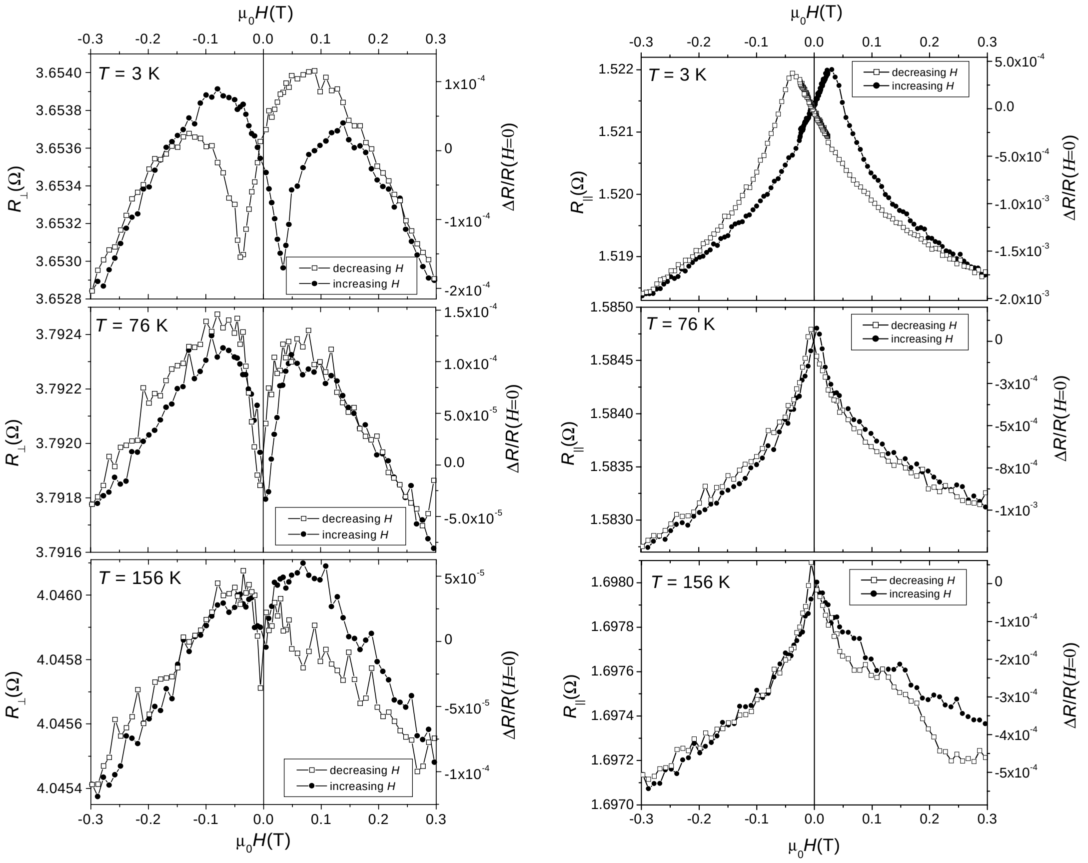

Figure 5.18: Left: transverse resistive isotherms of the (110)-textured sample. The decreasing (open squares) and increasing branch (full circles) were measured consecutively at $T = 3\,\mathrm{K}$, $76\,\mathrm{K}$ and $156\,\mathrm{K}$. Right: longitudinal resistive isotherms.

A further analysis of the electronic transport was performed by field-dependent resistivity measurements at constant temperature (resistive isotherms) in longitudinal and transverse geometry. The results are shown in Fig. 5.18. Three different temperatures were chosen according to the low temperature, intermediate temperature and high temperature range of Fig. 5.17. A complete cycle was performed ranging from the largest positive field to the largest negative field and vice versa. The maximum applied field was $|\mu_0 H_{\mathrm{ext}}| = 0.3\,\mathrm{T}$ which saturates the sample at all temperatures according to Fig. 5.8. As a common feature, all curves exhibit a linear decrease with increasing field in the high field region. Further measurements showed that this behavior is almost linear for $|\mu_0 H_{\mathrm{ext}}| \leq 2\,\mathrm{T}$ and no saturation effect is observed for either geometry. Beside this isotropic behavior, anisotropic contributions can be identified in the low field range. For the transverse loops these contributions cause local minima in the resistance which correspond, within the data point resolution, to the values obtained in section 5.1.3 for the coercive field H_{C}, at which the magnetization switches. The anisotropic resistivity contribution saturates at the saturation field H_{S} of the magnetization (see Fig. 5.8) indicated by the closure of the hysteresis loop. For the longitudinal geometry the sign of the effect is reversed: For $\rho_{\|}$ pointed maxima at H_{C} are formed and an increased slope for $H < H_{\mathrm{S}}$ is observed due to the anisotropic contribution. Again, linearity sets in for $H \geq H_{\mathrm{S}}$. In contradistinction to the common observation $\rho_{\|} > \rho_{\perp}$ (see Fig. 5.15), in the present case $\rho_{\perp} > \rho_{\|}$ is found. Additionally, the longitudinal loops unambiguously exhibit an asymmetry. As this effect can not be identified in the transverse measurements this may be related to the unidirectional anisotropy found in section 5.1. The differences between the increasing and the decreasing H branch, especially pronounced for the high temperature measurements, are due to thermal drift.

Summarized, the effects of magnetoresistance in the sample are of the order 10^{-4} at $0.3\,\mathrm{T}$ and thus rather small as compared to AMR and GMR effects observed in other materials. The isotropic contribution must be related to the ferromagnetic regions in the sample as it does not vanish above T_{N}. However, two properties deduced from the measurements appear unconventional: first, the observed AMR effect $\rho_{\perp} > \rho_{\|}$ is contrary to the usual behavior. Yet, this has been observed before, e.g. for $\mathrm{Ni}_{0.94}\mathrm{Cr}_{0.06}$ and $\mathrm{Fe}_7\mathrm{Se}_8$ [74]. Potter [83] explained such behavior with the dependence of the sign of $\Delta\rho$ on the dominating type of scattered electrons, i.e. spin up or spin down electrons. If the 3d-bands are nearly filled, small changes in energy may strongly influence the sign of $\Delta\rho$. Second, the isotropic contribution does not saturate at fields as high as $2\,\mathrm{T}$ which would be expected from conventional GMR or spin disorder effects. However, the hysteresis of Fig. 5.8 exhibit a non-zero slope in the magnetic saturation range indicating that hard-axis contributions of the FM regions are not completely aligned along the field direction even at high fields. This probably causes the non-saturating decrease of ρ at high fields. Further measurements must account for the origins of these effects.

Chapter 6

Magnetic properties of epitaxial thin film samples

The complex magnetic behavior of $\mathrm{Ti}_x\mathrm{Fe}_{1-x}$ in the C14 stability range is strongly related to structural aspects of the samples. The problem of the complex metallurgy has not been completely solved yet, expressed by the controversial statements on the range of homogeneity (ROH) and the preparational difficulties [23,11,21,22]. In polycrystalline bulk samples small amounts of Fe precipitates were detected, indicated by signatures of their T_C in high temperature susceptibility measurements [11]. In section 3.2 a series of epitaxial thin films was described, prepared with varying composition within the ROH. These films offer an alternative way to examine the magnetic properties of phase-pure C14 $\mathrm{Ti}_x\mathrm{Fe}_{1-x}$. The epitaxial film growth suppresses the formation of impurity grains such as Fe precipitates. In the present case, the phase purity within the ROH was mainly deduced from the absence of impurity reflections in longitudinal X-ray scans. Thus, possible amorphous contributions or crystalline contributions below the detection limit of the XRD cannot be entirely excluded. However, the Fe(110) reflections appeared readily if the substitution limit for Fe on Ti sites at the Fe-rich boundary of the ROH was exceeded and the dependence of the lattice constants is compatible with Vegard's law within the ROH. Both observations indicate that in the ROH Fe substitution on Ti sites is strongly favored above impurity phase formation. For the Ti-rich samples the ROH boundary could only be determined from the lattice constants as a function of x. Still, Ti substitution on Fe sites within the ROH and additional impurity phase formation beyond the Ti-rich boundary of the ROH can be expected as well. Furthermore, paramagnetic Ti impurity regions will only result in minor contributions to the magnetic susceptibility as compared to the ferromagnetic Fe precipitates.

In this chapter the results of temperature- and magnetic field-dependent SQUID magnetization measurements of epitaxial thin films in the C14 stability range are presented. In section 6.1 the magnetic susceptibility data of the series, measured at a low magnetic aligning field, is analyzed as a function of x. Additionally, magnetic hysteresis loops for the samples were taken at low temperatures. The in-plane and out-of-plane measurements are described in section 6.2. Following in section 6.4 is a discussion of the relationship of structural aspects with the magnetic properties. The chapter concludes with a discussion.

6.1 Magnetic susceptibility

The magnetic susceptibility χ is a measure for the response of a magnetic sample to an external magnetic field. For a paramagnetic or diamagnetic sample the isothermal volume susceptibility χ_V is defined as [84]

$$\chi_\mathrm{V} = \lim_{H_\mathrm{ext}\to 0} \left(\frac{\partial M}{\partial H_\mathrm{ext}} \right)_T \tag{6.1}$$

For samples exhibiting magnetic long-range order the susceptibility is only well-defined above the ordering temperature. In the FM case the susceptibility is described by the Curie-Weiß law above T_C. At T_C χ diverges. Below T_C, for an ideal soft-magnetic sample without domain wall pinning and magnetic anisotropies, the net magnetization cancels due to the formation of magnetic domains which minimize the magnetic stray field and thus the free energy. To obtain information on the magnetic response of such a sample, a small magnetic aligning field is usually applied. Commonly, the measured $\frac{M}{H_\mathrm{ext}}$ corresponds to the isothermal susceptibility, as long as the $M(H)$-response remains reversible. The magnetization values given are always expressed in the SI units of volume magnetization [A/m].

6.1.1 Measurements

All temperature-dependent magnetization curves presented in this section were obtained during cool down of the samples in an external magnetic field $\mu_0 H_\mathrm{ext} = 9\,\mathrm{mT}$ from $T = 285\,\mathrm{K}$ to $T = 5\,\mathrm{K}$. The magnetic field was applied perpendicular to the c-axis which is the easy axis of magnetization in bulk samples. In Fig. 6.1 two typical $M(T)$ curves of a stoichiometric and an Fe-rich sample are compared. For both curves, starting from high temperatures, the magnetization increases to a local maximum which is pronounced for the stoichiometric sample and much less so for the Fe-rich sample. The temperature of this maximum is identified as the ordering temperature T_N of AF ordering regions in the samples. Equally pronounced for the stoichiometric sample is the subsequent drop of the susceptibility to a local minimum at T^* which is due to increasing AF order in the sample. The increase of $M(T)$ at lower temperatures can be related to FM ordering regions. Consequently, the minimum at T^* is due to a superposition of an FM and AF susceptibility curve and is a measure for the ordering temperature

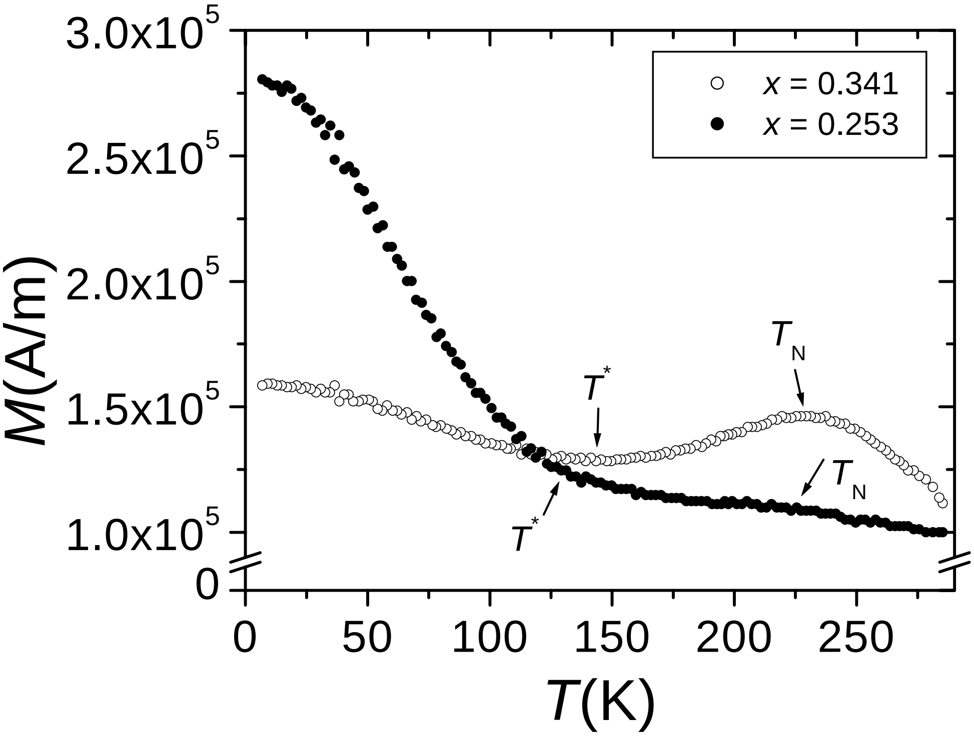

Figure 6.1: Susceptibility for $x = 0.252$ (full circles) and $x = 0.341$ (open circles). The respective ordering temperatures are marked by arrows.

of FM-like regions. An exact determination of the ordering temperature T_C from the magnetization data would only be possible by exactly modelling the complete curves. For the iron-rich sample the FM-like increase is more distinct than for the stoichiometric sample. Additionally, a background magnetization persisting to the highest temperatures measured is to be noticed.

In chapter 5 the formation of small AF and FM ordered regions in textured polycrystalline films was observed. In the case of the epitaxial samples similar contributions are found. The ratio of the contributions strongly depends on the composition. The dependence on the composition can be derived from the susceptibility measurements of the complete series which are compiled in Fig. 6.2. For all curves, both the FM and the AF contribution can be distinguished. In the range of the stoichiometric composition the maximum formed at T_N is very distinct. On decrease of x the maximum is reduced and remains only faintly visible at the iron-rich boundary of the ROH. For samples with $x > \frac{1}{3}$ the same behavior is observed, but the FM contributions appear less pronounced. In contrast to the samples at the Fe/TiFe$_2$ boundary, for the samples at the Ti-rich side the maximum at T_N remains clearly visible.

An at least qualitative determination of the contribution of the FM-like regions in the samples was achieved by comparing the magnitude of the magnetization

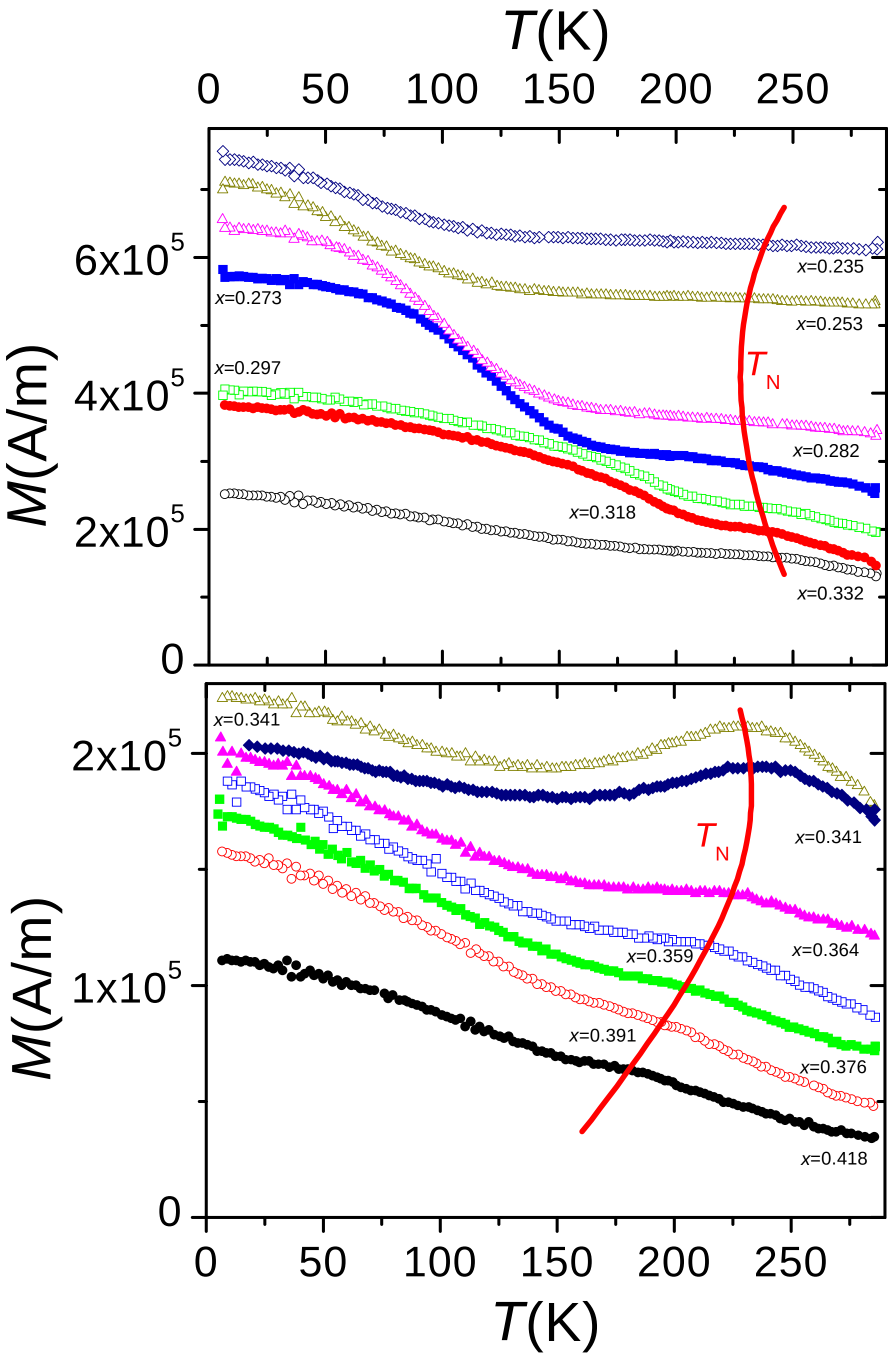

Figure 6.2: Overview of the temperature-dependent magnetization curves of the epitaxial $(00l)$-grown sample series. The applied aligning field was $\mu_0 H_{\text{ext}} = 9\,\text{mT}$. The curves are labelled with the respective Ti concentration x. The vertical curves indicate the positions of T_{N}. The relative magnetization values are to scale, but offsets were added to facilitate comparison.

at lowest temperature. In the present case the excess magnetization, which is the difference between the magnetization at low temperatures and the background magnetization at high temperatures $\Delta M = M(T = 5\,\mathrm{K}) - M(T = 285\,\mathrm{K})$, is assumed to be proportional to the volume of FM-like regions. In Fig. 6.3 ΔM is plotted as a function of the composition. A pronounced minimum is observed at the stoichiometric point indicative of a rather large contribution of AF regions. With increasing deviation from the stoichiometric composition ΔM, and thus the FM-like contributions, grow. The FM volume increase is strongly pronounced for the Fe-rich samples whereas it is found to be moderate for Ti-rich samples. At either boundary of the ROH, as determined in section 3.2.5, a maximum of ΔM, and thus the FM volume, is found. For off-stoichiometric samples outside the ROH, ΔM decreases. This effect is pronounced for the Fe-rich samples and must be related to a structural change in the samples at the ROH boundaries. This will be accounted for in more detail in section 6.1.2.

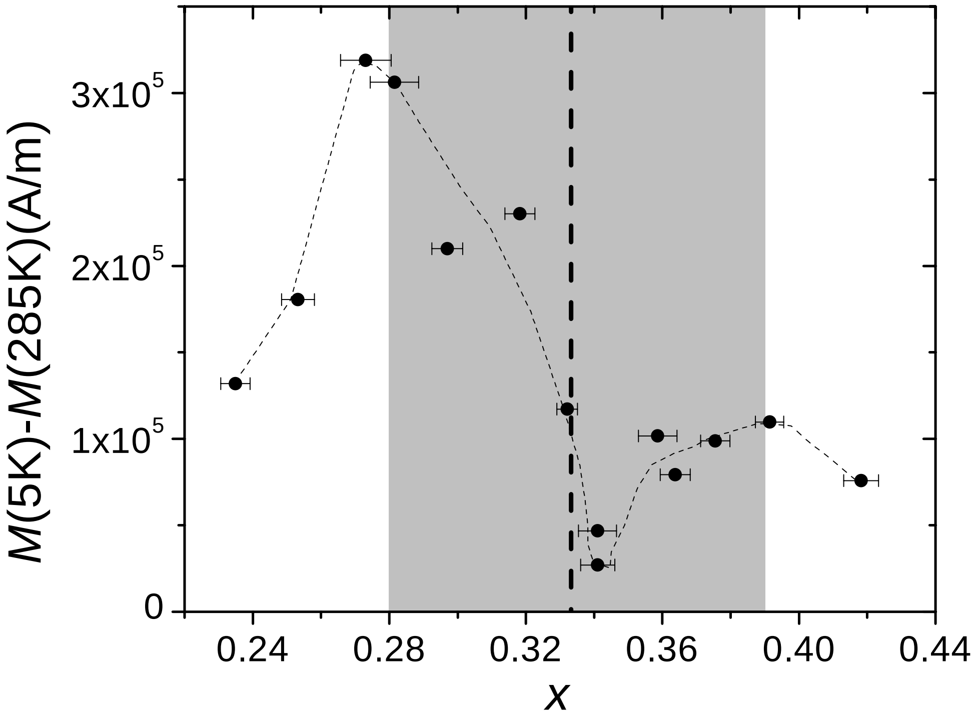

Figure 6.3: $\Delta M = M(T = 5\,\mathrm{K}) - M(T = 285\,\mathrm{K})$ taken from Fig. 6.2. ΔM can be assumed to be proportional to the volume of FM-like regions. The shaded area represents the range of homogeneity. Dashed lines are to guide the eye.

6.1.2 Magnetic phase diagram

T^* and T_N were determined from the data of Fig. 6.2 by fitting parabolas to the data which were first background corrected by subtracting a linear function. From the thus obtained characteristic temperatures, representing phase boundaries, a magnetic phase diagram was established which is shown in Fig. 6.4. In the ROH four regions can readily be identified : (1) a paramagnetic (PM) region at high temperatures, (2) an AF region, in which the FM-like contributions are paramagnetic and (3), (4) FM*/AF and AF/FM* coexistence regions on the Fe-rich and the Ti-rich side, respectively, in which a combined AF/FM behavior is found.

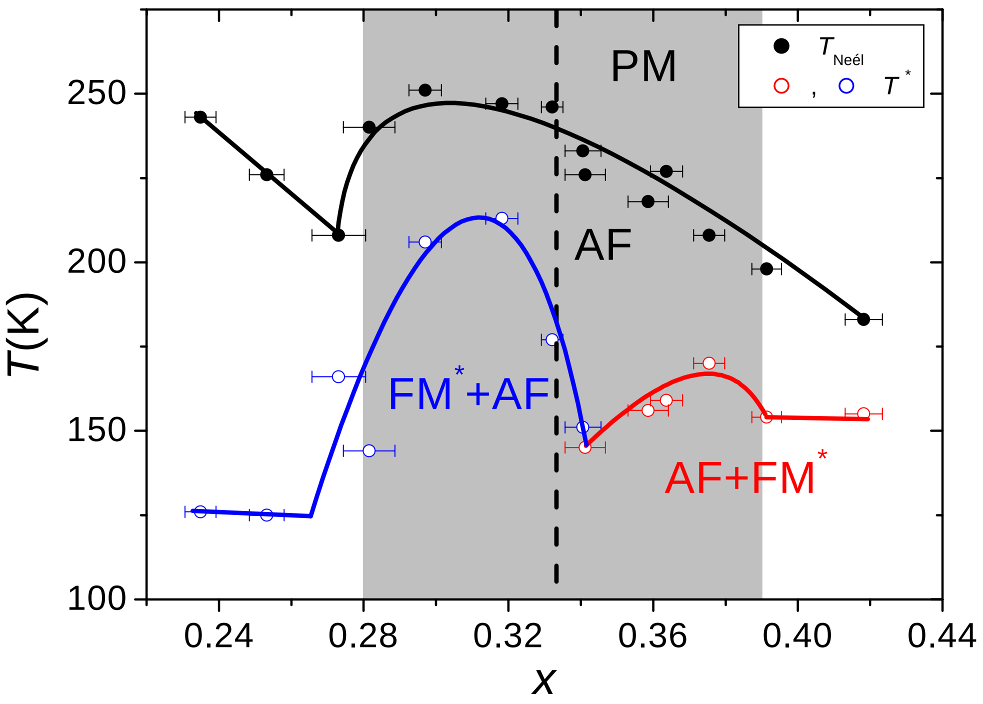

Figure 6.4: Magnetic phase diagram of $\mathrm{Ti}_x\mathrm{Fe}_{1-x}$ (001)-oriented epitaxial thin films in the C14 stability range. The phase boundaries were deduced from the data of Fig. 6.2 as indicated in Fig. 6.1. The shaded area represents the range of homogeneity.

T_N of the thin films is lower than $T_\mathrm{N}^\mathrm{bulk} \cong 275\,\mathrm{K}$ of bulk samples. This is probably due to a finite-size induced reduction of critical temperatures. A maximum of T_N is formed with a monotonous decrease to either side within the ROH. This decrease of T_N is caused by a dilution of the AF matrix due to Fe or Ti antisite occupation. The maximum of T_N would be expected at the stoichiometric point. Nevertheless, the maximum is shifted to the Fe-rich region. Since T_N is also determined by the degree of crystalline coherence in the samples, the enhancement of epitaxial single crystalline growth in the iron excess region, as discussed in section 3.2, competes with the reduction of T_{N} as a consequence of the dilution. Thus, the shift is most likely caused by this intricate interplay of dilution and coherence. Beyond the Fe-rich boundary of the ROH an increase of T_{N} is to be noticed. A possible explanation is given at the end of this section.

T^* exhibits a more complicated behavior dominated by clustering FM regions. Generally, in contradistinction to results obtained on bulk samples [11] (see below), T^* is found to be significantly lower than T_{N} in the complete compositional range covered by the thin film experiments. For the films this leads to the assumption that the C14 phase forms a well-stabilized antiferromagnetic matrix in which contributions of ferromagnetic C14 phase impurities with reduced T_{C} are embedded. These impurities are probably caused by Fe or Ti atoms on antisites breaking the symmetry of the unit cell, as was found in other experiments (see section 1.2.3).

At the stoichiometric point of the present phase diagram a local minimum of T^* is observed. This is assumed to be due to the predominant formation of the AF matrix in conjunction with small sized FM C14 phase clusters which may form a random network. On reduction of x, not only the FM network becomes more dense but the crystalline growth is also improved. A pronounced maximum of T^* is formed at $x_{T^*_{\mathrm{max}}} \approx 0.31$. Since the unit cell volume linearly decreases to the Fe-rich boundary of the ROH, a reduction of the FM C14 cluster size and thus T^* is assumed. Consequently, the constant T^* in the Fe segregation region is due to a constant minimum cluster size. On the Ti-rich side, the insertion of FM impurities caused by Ti atoms on antisites is accompanied by a degrading crystalline coherence and leads to the formation of a less pronounced maximum. Again, beyond the ROH boundary T^* remains constant.

In the following, a comparison of the magnetic phase diagrams obtained from the epitaxial thin film data and bulk samples is performed. Fig. 6.5 shows the magnetic phase diagram for bulk samples which were prepared in several experiments [11]. The data were obtained in a large magnetic aligning field of $\mu_0 H_{\mathrm{ext}} = 1\,\mathrm{T}$. This is in contradistinction to the thin film phase diagram which was determined from data taken at $\mu_0 H_{\mathrm{ext}} = 9\,\mathrm{mT}$. Different regions of FM, AF and coexisting AF/FM order can be identified. For the Fe-rich region, below $x = 0.30$, a FM state is found for all temperatures below the paramagnetic (PM) region, whereas for the thin films a coexistence region at low temperatures and an AF region above T^* is stabilized. Moreover, for all temperatures below the PM region about the stoichiometric composition, a purely AF state exists for the bulk samples. Both phase diagrams become qualitatively comparable, at least in the ROH, if it is assumed that T^* of the thin film phase diagram is shifted to above T_{N}. This can be caused by a segregation network of Fe precipitates. Such precipitates were detected by their magnetic signature at high temperatures for a

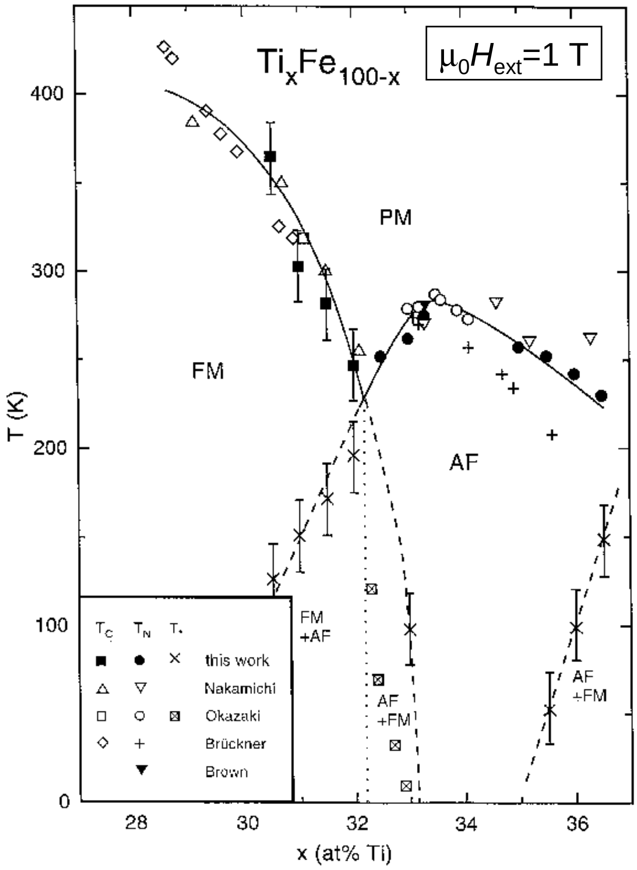

Figure 6.5: Magnetic phase diagram for 1 T aligning field of bulk samples in the C14 stability range [11]. The data were collected from several experiments as indicated by the different symbols.

set of samples analyzed in [11]. This network would then be aligned by the large magnetic field. The coupling of the Fe precipitates with the FM C14 regions may then have significantly increased T^*. However, two important features remain different: (1) the maximum of the PM/AF boundary is shifted to lower x for thin films which is due to the improved crystalline coherence in the Fe rich region of the ROH; (2) no pure AF phase is in the thin films. The Fe segregation may also explain the predominant formation of AF regions about the stoichiometric point in the bulk samples and thus explain the difference (2). The analysis of the epitaxial thin films, as described in this work, gives no hints for Fe precipitates in the ROH and is thus assumed to reflect the sole properties of Ti$_x$Fe$_{1-x}$ in the C14 stability range. In contradistinction to this is the bulk phase diagram which is most probably determined by the effects of Fe segregation.

Finally, an intuitive explanation for the drop of ΔM at the ROH boundaries in Fig. 6.3 shall be given. The effect seems to be connected to a structural change in the samples. Within the ROH, for Fe-rich samples at the boundary, the lattice is oversaturated with Fe atoms on antisites and the energy loss due to the deviations from the ideal crystal structure is rather large. Crossing the boundary, additional free energy is gained by the precipitation of small Fe clusters in the C14 phase matrix, as indicated by the formation of the Fe(110) reflections in XRD scans. The constant values of T^* suggest that the FM C14 phase clusters have a uniform size. The increasing Fe clustering reduces the number of Fe atoms on antisites in the FM-like C14 phase regions thus decreasing the FM C14 phase cluster density but not their size, and thus the magnetization of this component. On the other hand, the reduction of the FM C14 phase cluster density causes the volume of the AF C14 regions and thus T_{N} to increase, as can be seen Fig. 6.4. The Fe clusters are assumed to be initially superparamagnetic (SPM). A further decrease of x increases the size of the clusters. Thus, for very low x beyond the composition range of the experiment an increase of ΔM should be found. A similar explanation may also be valid for the Ti-rich side except for samples with a very large titanium concentration. In this case a steady reduction of ΔM beyond the ROH boundary is expected. A detailed analysis of the microstructure of the samples is needed to verify the speculations, but is beyond the scope of this work.

6.2 Magnetic isotherms

Hysteresis in magnetic isotherms (i.e. magnetic hysteresis loops) of magnetic samples is due to irreversible effects. These are, for example, caused by magnetic domain wall pinning or magnetic anisotropies. The shape of the hysteresis loops is characteristic for the integral magnetization reversal process induced by an external field. In-plane and out-of-plane hysteresis loops with the external magnetic field H_{ext} either parallel or perpendicular to the film plane were measured at temperatures between $T = 285\,\mathrm{K}$ and $T = 5\,\mathrm{K}$ on the sample series discussed in the previous section. Hysteresis loops for a sample with $x = 0.341$ taken in both geometries are presented in Fig. 6.6. If normalized to the saturation magnetization the curves reproduce the typical magnetization reversal of all samples of the series at $T = 5\,\mathrm{K}$. The in-plane loop on the left of Fig. 6.6 exhibits a mostly FM-type hysteresis loop with a remnant state, coercivity and rounded edges due to domain wall motion. At high fields, a non-vanishing slope is to be noticed which may indicate a improper correction of the diamagnetic substrate background or paramagnetic contributions. The loop shape is most probably caused by a non-easy-axis alignment of the sample. The strong magnetic anisotropy along the c-axis of the C14 structure competes with the shape anisotropy of the thin film which tends to force the easy axis into the film plane. The resulting direction of lowest free energy is canted. Furthermore, this canted easy axis is indicated by an open hysteresis even at high fields. For the present in-plane loop, the hysteresis is closed above $|\mu_0 H_{\mathrm{ext}}| \cong 0.5\,\mathrm{T}$.

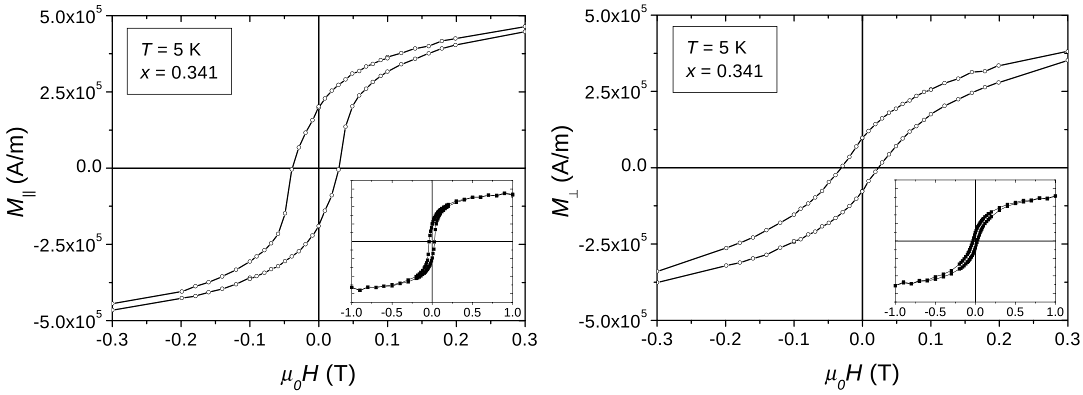

Figure 6.6: Magnetic hysteresis loops $M_{\|}(H)$ (left) and $M_{\perp}(H)$ (right) taken at $T = 5\,\mathrm{K}$ for a sample with $x = 0.341$. The insets show the maximum field range as an overview.

For the out-of-plane loop on the right of Fig. 6.6, a very similar behavior is found, except for a pronounced stretch of the loop along the magnetic field axis. Introducing an effective demagnetizing field $H_{\mathrm{demag}} = -N_{\perp} M$, for a correction with $N_{\perp} = 0.2$, a non-stretched loop with almost infinite slope at the coercive field is found. The such obtained curve is overlayed with the in-plane curve in Fig. 6.7. The main difference is given only by the saturation magnetization M_{S}. No further evaluation of the anisotropy energies contributing to the total free energy was possible, as the detailed microstructure, which strongly influences the demagnetization tensor, is not exactly known. Consequently, no demagnetization corrections were applied to the out-of-plane hysteresis loops shown in the following.

In Fig. 6.8 the $M(H)$ curves for an almost stoichiometric composition $x = 0.341$, for $x = 0.235$ in the Fe-rich region and $x = 0.418$ in the Ti-rich region are compared. Except for the saturation magnetization M_{S}, all samples exhibit the same shape for $M_{\|}(H)$ and $M_{\perp}(H)$, respectively. It has to be noticed that no contributions of the AF regions, according to the results of section 6.1, are discernible. Due to the FM C14 contributions, which are present in all samples, only FM-type hysteresis loops are obtained in the complete compositional range.

Further investigations of the magnetization reversal behavior were performed by a composition-dependent analysis of the basic parameters determining the shape of the loops. The evaluation of the out-of-plane data is complicated by the additional demagnetization effects. In the following, only the in-plane data will be analyzed. At the top of Fig. 6.9 the saturation magnetization M_{S} is depicted

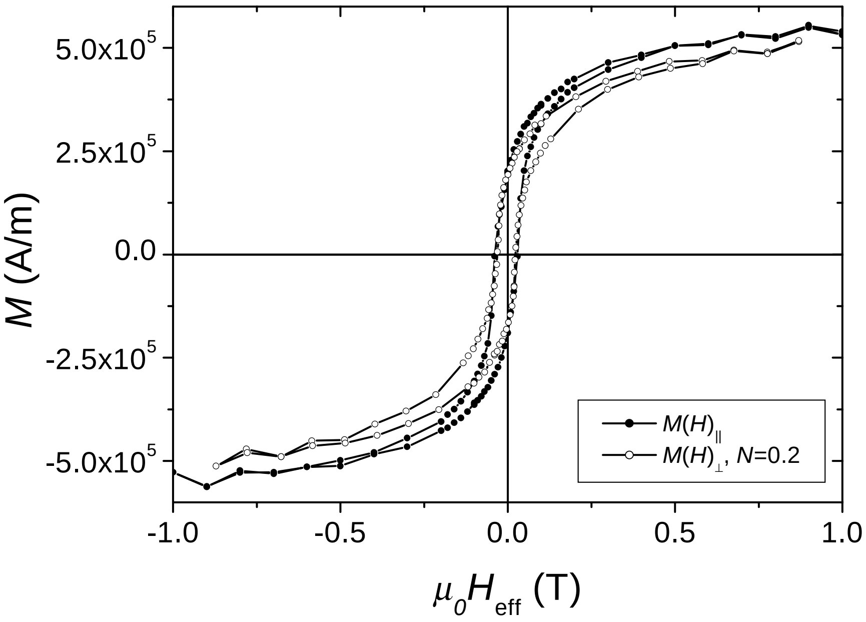

Figure 6.7: In-plane hysteresis loop $M_{\|}(H)$ (full circles) and $M_{\perp}(H)$ (open circles) for $x = 0.341$. $M_{\perp}(H)$ is corrected with an effective demagnetization factor $N_{\perp} = 0.2$. $H_{\text{eff}} = H - N_{\|,\perp}M$.

as a function of composition. The values were taken at $\mu_0 H_{\text{ext}} = 0.5\,\text{T}$, at which all the samples were magnetically saturated, but did not suffer from instabilities in the SQUID measurements occurring preferably at elevated magnetic fields. A pronounced growth of M_{S} is found for decreasing x on the Fe-rich side. This corresponds to the growing FM C14 phase contributions within the ROH allowing for long-range ordered ferromagnetism. If the FM C14 cluster-size is assumed to decrease for $x < x_{T^*_{\text{max}}} = 0.31$ (see section 6.1) the number of FM C14 clusters must disproportionate increase with decreasing x. Beyond the Fe-rich boundary Fe precipitates are assumed to mainly contribute to the still increasing M_{S}. [1]

Overall, the remnant magnetization M_{R} follows the behavior of M_{S}, as shown in the middle of Fig. 6.9. This is in accordance with the earlier observation that the shape of the hysteresis is independent of M_{S}. An indicator for the direction of the anisotropy axis in the samples is the ratio $r = M_{\text{R}}/M_{\text{S}}$. Crudely speaking, for

---

[1] For $x > \frac{1}{3}$, M_{S} is found to remain at a constant value of $3 \cdot 10^5\,\text{A/m}$. This may be explained by a compensation of the decreasing Fe concentration by growing FM contributions due to impurities induced by either substitutions of Ti on Fe antisites or lattice distortions. The significant large value for one sample at $x = 0.341$ was also found in the susceptibility measurements as a large background magnetization (see Fig. 6.13) and is probably caused by instabilities in the preparation process. In section 6.1 the formation of SPM Fe clusters beyond the Fe-rich boundary of the ROH was suggested. In this region, M_{S} is still increasing indicating that these clusters are aligned by the external field and thus contribute to M_{S}.

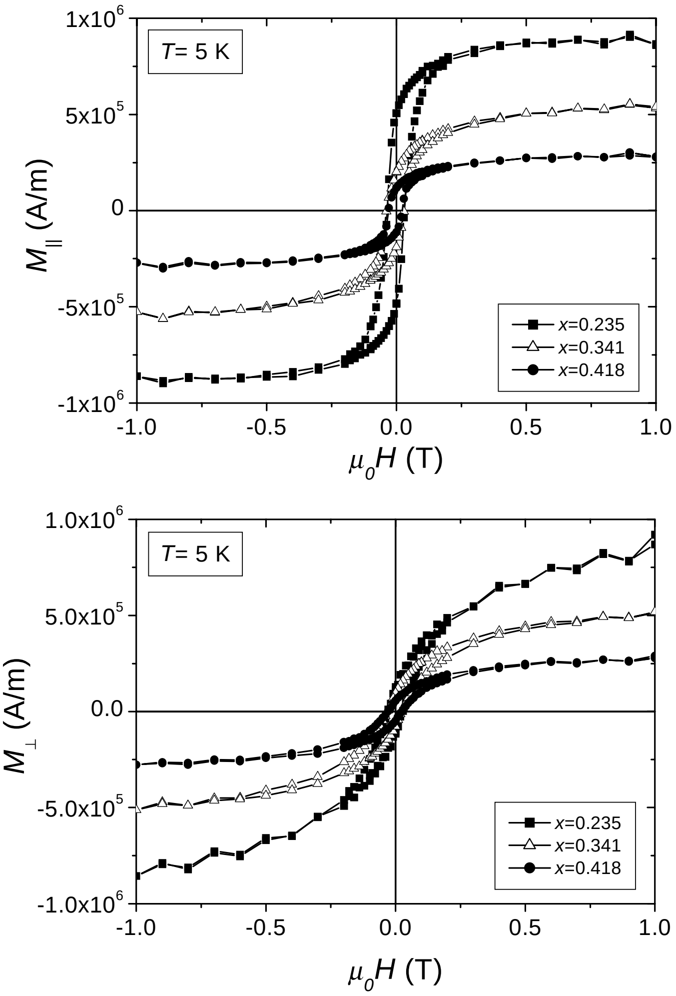

Figure 6.8: In-plane hysteresis loops $M_{\|}(H)$ (top) and out-off-plane hysteresis loops $M_{\perp}(H)$ (bottom) of samples with different composition as indicated. The oscillating behavior at high fields is due to instrumental instabilities during the measurement.

a geometry with the external field along the easy axis r is 100 %, whereas along a hard direction r decreases to 0 %. At the bottom of Fig. 6.9, a rather sharp transition occurs at the stoichiometric point from $r \approx 40\,\%$ in the Ti-rich region to $r \approx 60$ to 70 % in the Fe-rich region. Two explanations seem to be possible: either the anisotropy axis of the C14 FM regions is flipped perpendicular to the c-axis which was not observed for bulk samples. Or the crystalline anisotropy of the C14 FM regions is strongly reduced with respect to the C14 AF regions thus causing a dominance of the shape anisotropy. The latter explanation appears likely correct. On increase of x in the Ti-rich region r is steadily increasing, too. This is possibly caused by a lower crystalline anisotropy of the Ti substituted C14 FM regions.

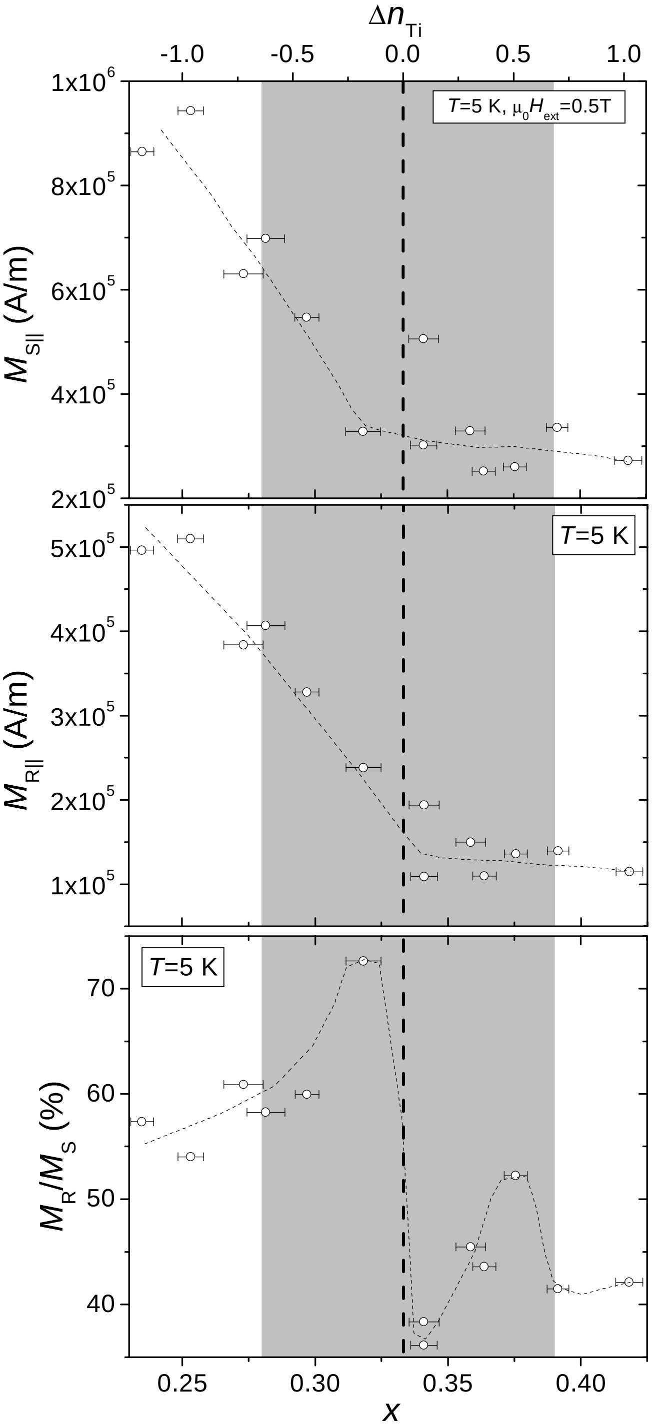

Figure 6.9: Saturation magnetization $M_{S\|}$ (top) and remnant magnetization $M_{R\|}$ (middle) as a function of composition. M_R/M_S (bottom) is an indicator of the direction of the anisotropy axis. All data were taken with the magnetic field in-plane. Dashed lines to guide the eye.

Finally, the coercivity of the samples as a function of the composition was analyzed. At the top of Fig. 6.10 the coercive field H_C is shown for the external field in the film plane. An almost reciprocal behavior as compared to $T_\mathrm{C}(x)$ is observed: for the stoichiometric composition H_C is maximal, whereas for the Fe-rich and Ti-rich regions of the ROH local minima are formed. Beyond the ROH in either the Fe- or Ti-rich region, the coercive field increases. It can be deduced that H_C is strongly correlated with the concentration of FM C14 impurity clusters. A large concentration of clusters causes a reduction of H_C from a large value, as expected for a low impurity concentration. This was observed in Monte Carlo simulations to be described in section 7.4.2. SPM Fe clusters are not expected to contribute to the coercivity.

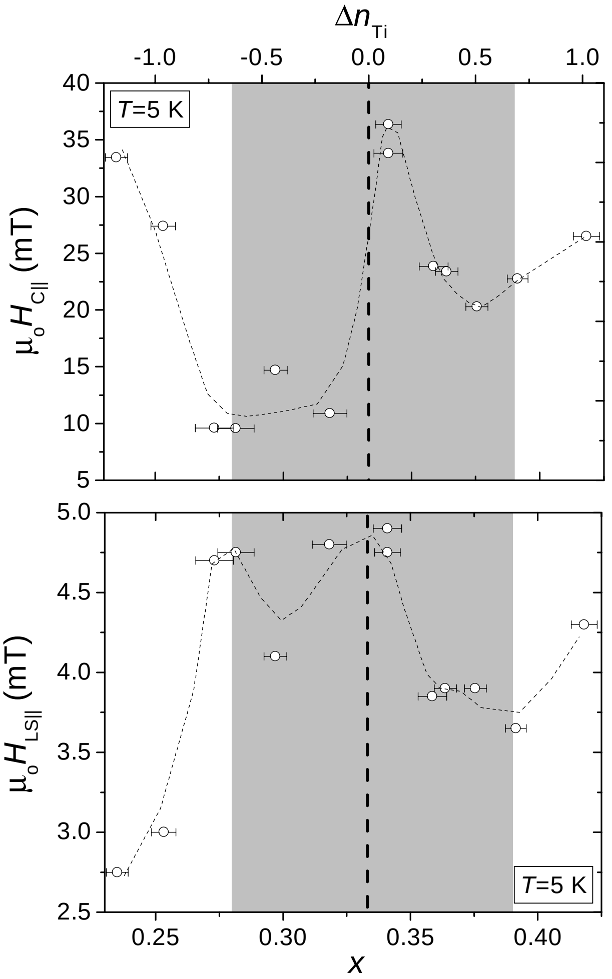

Figure 6.10: Coercive field $H_{\mathrm{C}\|}$ of the hysteresis loops taken at $T = 5\,\mathrm{K}$ (top) and negative displacement field $H_{\mathrm{LS}\|}$ with respect to zero field (bottom) as a function of composition x. All data were taken with the magnetic field in-plane. Dashed lines are to guide the eye.

All hysteresis loops exhibit a more or less pronounced displacement to the opposite direction of the applied cooling field or the remnant magnetization of the sample itself. The values of these loop shifts H_{LS}, measured for the epitaxial sample series, exhibit no distinct behavior in the ROH. Generally, all values are found to be significantly lower those than for the textured polycrystalline samples examined in section 5.1. As explained before, the epitaxial samples are assumed to have larger regions of the respective magnetic order. Thus, H_{LS} decreases with the surface to volume ratio. For large Fe concentrations outside the ROH, H_{LS} is becoming very small as the magnetization in Fig. 6.3. This is compatible with the assumption mentioned above that the formation of SPM Fe clusters reduces the C14 FM contributions and thus the effective AF/FM interface area. The small values of H_{LS} are compatible with zero if some residual magnetic flux is frozen in the SQUID. This was checked by measuring a Fe thin film reference sample. The corresponding hysteresis loops for $\mu_0 H_{\mathrm{FC}} = \pm 9\,\mathrm{mT}$ are depicted in Fig. 6.11. With $\mu_0 H_{\mathrm{LS}} \leq 1\,\mathrm{mT}$ at a coercive field of $\mu_0 H_{\mathrm{C}} = 58\,\mathrm{mT}$ the extrapolated loop-shift is significantly below all values measured for TiFe$_{1-x}$ films. All hysteresis loop displacements are thus related to the properties of the samples themselves.

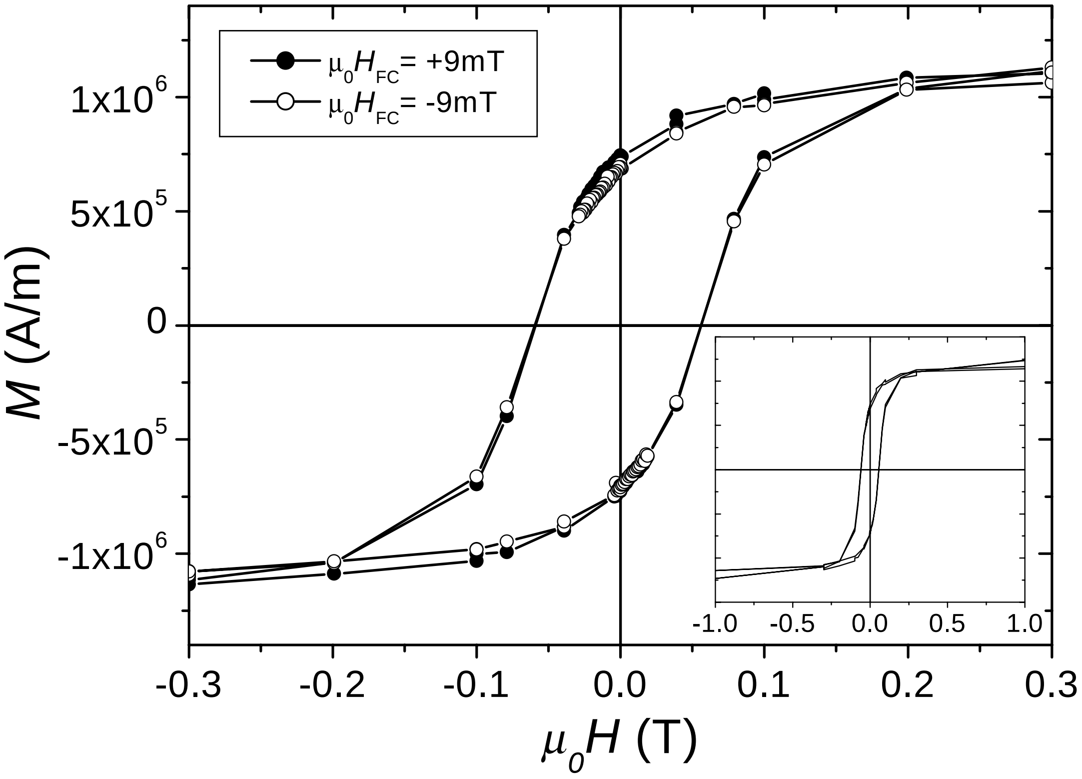

Figure 6.11: $M(H)$ of an approximately 13 nm thick (110)-textured Fe film on an $Al_2O_3(001)$ substrate. The cooling field $|\mu_0 H_{\mathrm{FC}}| = 9\,\mathrm{mT}$ was applied in positive (full circles) and negative (open circles) direction.

Further investigations were performed by the analysis of hysteresis loops. For the sample with $x = 0.341$ and low RM, the dependence of the magnetization reversal on the temperature was investigated by analysis of the data depicted in Fig. 6.12. Four hysteresis loops were taken at selected temperatures: (1) $T = 5\,\mathrm{K}$, (2) $T = 150\,\mathrm{K}$ at T^*, (3) $T = 215\,\mathrm{K}$ right below T_N and (4) $T = 285\,\mathrm{K}$, well above T_N. The slope in the hysteresis loops is almost equal in the whole temperature range. The coercive field is reduced with increasing temperature. In contradistinction, above T_N the coercivity increases again. SQUID instabilities may be responsible for this behavior, indicated by steps and asymmetry in this particular curve. For the curve at $T = 215\,\mathrm{K}$, a strongly reduced H_C is observed. Assuming a canted anisotropy axis for the AF regions, this hysteresis can be interpreted as an AF hysteresis, taken along an oblique angle with regard to the anisotropy axis. The shape of the FM-like hysteresis loops can be reproduced by Monte Carlo simulations, as is described in section 7.4.2. In the simulation, the weak spin coupling along the c-axis in the C14 AF regions combined with a significant dilution with FM impurities is responsible for the generation of the FM-type hysteresis loops.

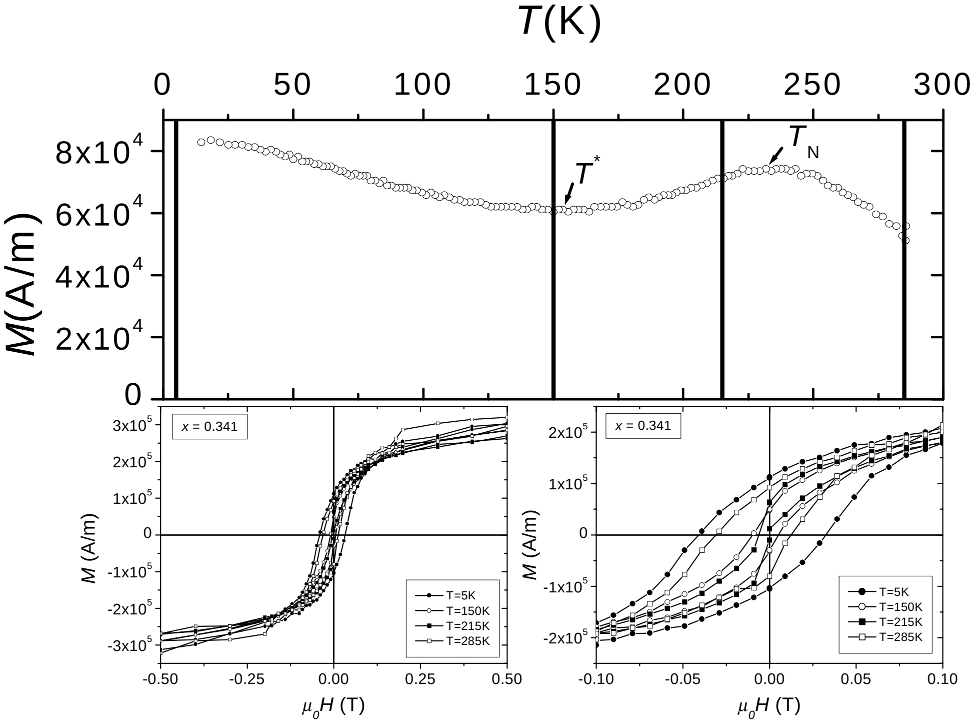

Figure 6.12: Top: Susceptibility curve for a sample with $x = 0.341$. The vertical lines indicate the temperatures at which the hysteresis loops were taken. Bottom: Hysteresis loops taken at different temperatures in the complete measured range (left) and in the hysteretic range (right).

6.3 High temperature background magnetization

In section 6.1 it was already mentioned that in the susceptibility data a residual magnetization (RM) well above T_{N} and T_{C} of the C14 Laves phase was found. Since the induced magnetization at an applied field $\mu_0 H_{\mathrm{ext}} = 9\,\mathrm{mT}$ should be negligible for magnetic regions with strong spin coupling and the Fe precipitates are readily formed only outside the ROH, the origin of this RM remains unclear. An overview of RM(x) for $\mu_0 H_{\mathrm{ext}} = 9\,\mathrm{mT}$ at $T = 285\,\mathrm{K}$ is given in Fig. 6.13. At the Ti-rich boundary of the ROH the RM is significantly smaller than at the Fe-rich boundary. About the stoichiometric composition a pronounced maximum is found. In the suggested model, for $x > \frac{1}{3}$, small weakly ferromagnetic C14 clusters are created due to Ti atoms on Fe sites. Vice versa, for $x < \frac{1}{3}$, small ferromagnetic C14 clusters, which are more strongly coupled, are formed by Fe substitution on Ti antisites. If the RM was caused by Fe precipitates already formed in the ROH, an increase of RM would be expected for lower x outside the ROH and no plausible explanation for the occurrence of the maximum could be found. To the contrary, a decrease outside the ROH is observed.

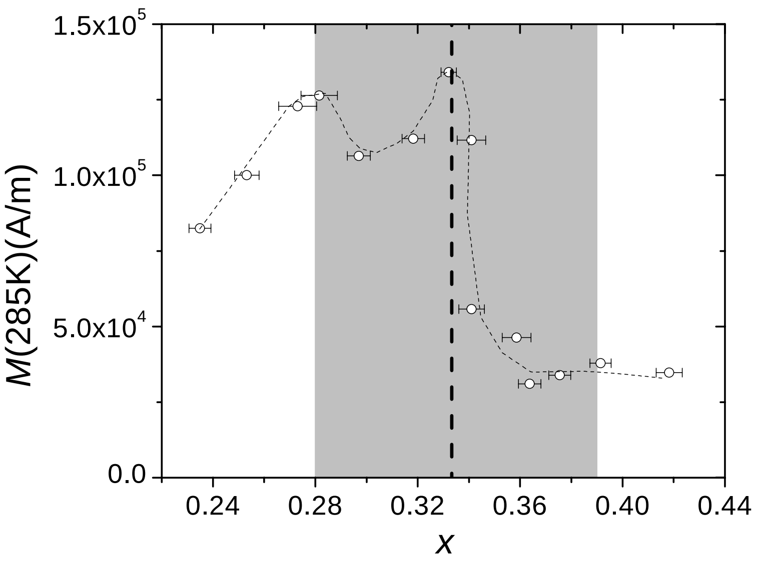

Figure 6.13: Residual magnetization M at $T = 285\,\mathrm{K}$ in an external field $\mu_0 H_{\mathrm{ext}} = 9\,\mathrm{mT}$ applied parallel to the film plane. The ROH is marked by the shaded area. Dashed lines to guide the eye.

The rather complicated behavior of the RM may be explained as follows: for large x the low concentration of Fe atoms causes a low induced magnetization. If x is reduced, this concentration increases, resulting in a gradually increasing induced magnetization inside the ROH. However, in Monte Carlo simulations (see

Fig. 7.9) it was also found that the induced magnetization at a given temperature about T_{N} and for a constant spin density increases for an increasing dilution with FM impurities. As to the origin of the maximum, one can only speculate. The transition from low RM to high RM coincides with a significant change in the anisotropy of the C14 FM regions, as was described above (see bottom of Fig. 6.9). Thus, a smaller aligning field is needed to induce a given magnetic moment. Beyond the Fe-rich boundary of the ROH, the RM is decreasing simultaneously with ΔM (see Fig. 6.3) which was ascribed to the formation of SPM Fe clusters. Since the magnetization induced in SPM clusters is small the RM follows this decrease.

6.4 Structural effects on the magnetic properties

In section 3.2.2 the important dependence of the film growth on the growth temperature and the resulting crystalline structure was described in detail. An epitaxial temperature $T_{\mathrm{epi}} \approx 825\,\mathrm{K}$ was found. In the following, the difference between the magnetic properties of thin films prepared slightly above T_{epi} and at the optimum temperature $T_{\mathrm{opt}} = 1100\,\mathrm{K}$ will be discussed.

The films prepared above T_{epi} exhibit exclusively $\mathrm{TiFe_2}(00l)$ reflections in the XRD patterns. However, the intensity of the reflections and the sublattice order of films deposited at $T_{\mathrm{epi}} < T \ll T_{\mathrm{opt}}$ is strongly reduced as compared to the epitaxial films deposited at T_{opt}. Furthermore, the less ordered films show no indication of AF contributions in both, the susceptibility and the $M(H)$ measurements. In Fig. 6.14, the susceptibility of films prepared with nearly the same composition is compared: For the well-ordered sample, a local maximum at T_{N} and an increase at lower temperatures is visible, as described in section 6.1. In contrast, for the less-ordered sample only FM behavior is found. This was checked for several samples. The respective Curie temperature is elevated as compared to the well-ordered sample. Since the sublattice order is distorted in large regions for samples prepared at lower temperatures, these regions are predominantly FM and the Curie temperature for these regions increases.

Additionally, the shape of magnetic isotherms, taken at low temperatures, was analyzed for less-ordered samples. In Fig. 6.15 a collection of hysteresis loops is presented which were taken in the in-plane and out-off-plane geometry for samples prepared in the Fe-rich region of the ROH. This region was selected because the crystalline coherence is best in the Fe-rich region of the ROH for samples prepared at T_{opt} (see section 3.2.5). For all samples the coercivity in the in-plane orientation is very small and the shape of the hysteresis loop is almost rectangular. This indicates a soft magnetic contribution combined with

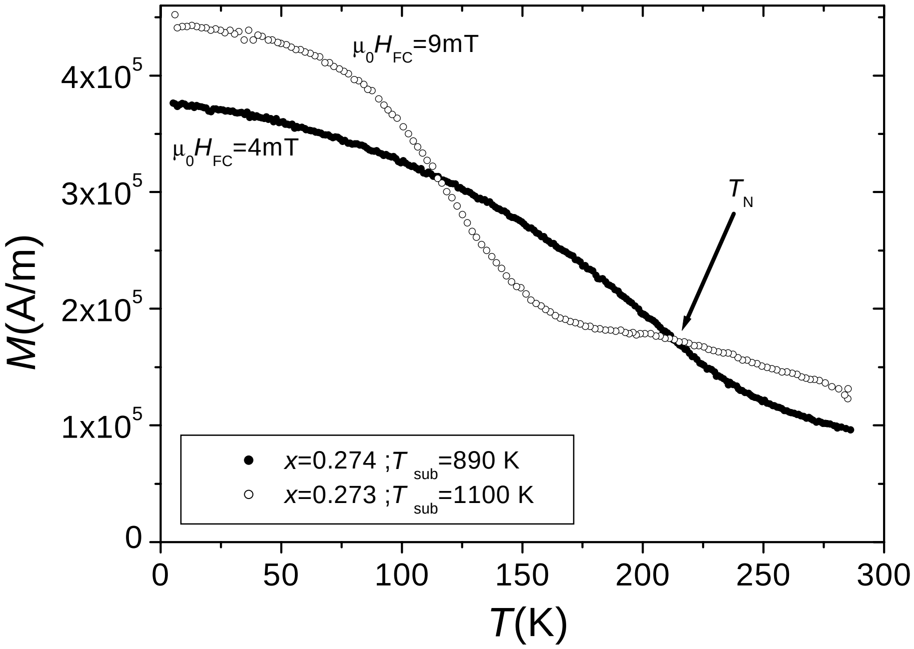

Figure 6.14: Comparison of the susceptibility data for films prepared at $T_{\mathrm{sub}} = 890\,\mathrm{K}$ (full circles) and at $T_{\mathrm{sub}} = T_{\mathrm{opt}} = 1100\,\mathrm{K}$ (open circle). The arrow indicates the position of T_{N} for the sample prepared at T_{opt}.

the shape anisotropy of the thin film and can be related to disordered Fe/Ti regions with low crystalline anisotropy. Furthermore, the measurements exhibit a pronounced opening of the hysteresis loop above the coercive field for $M_{\|}$ and a distinct hysteretic behavior of $M_{\perp}$, indicating a contribution with the easy axis directed out of the film plane. In this context, the contribution can be referred to the crystalline C14 phase in its predominantly distorted FM configuration with the crystalline anisotropy axis along the c-axis. Additionally, the differences in the measurements in Fig. 6.15 underline that the shape of magnetic isotherms, taken for samples prepared at low temperatures under comparable conditions with almost equal composition, are much more sensitive to preparational instabilities. In contradistinction, the samples prepared at T_{opt} exhibit only minor deviations even for largely differing compositions.

6.5 Conclusions

In this chapter it was shown that epitaxial $\mathrm{Ti}_x\mathrm{Fe}_{1-x}$ thin films in the C14 stability range exhibit very particular magnetic properties. The main result is the occurrence of a combined magnetic behavior of C14 phase antiferromagnetic and ferromagnetic regions, characterized by their critical temperature T_{N} and T^{*},

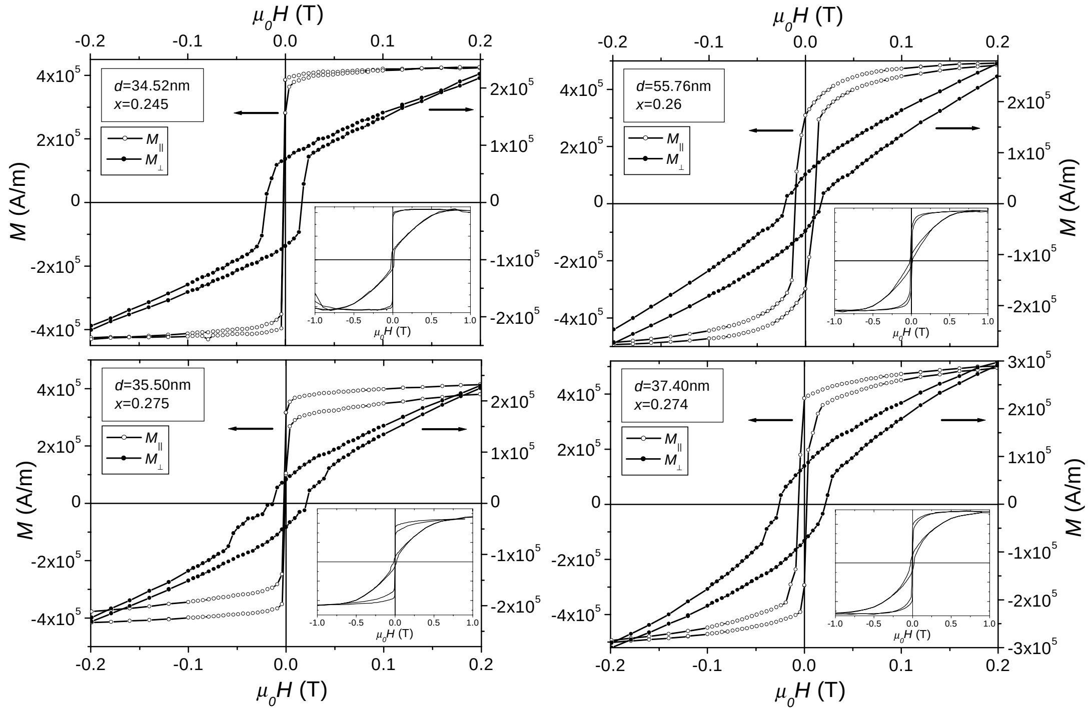

Figure 6.15: Magnetic isotherms at $T = 5\,\mathrm{K}$ of epitaxial samples prepared at $T_{\mathrm{sub}} = 890\,\mathrm{K}$. $M_\parallel(H)$ (open circles) and $M_\perp(H)$(full circles) are combined in one figure. The insets show an overview of the complete range of the respective measurements.

respectively. The dependence of the magnitude of the magnetization on the composition supports this picture. A similar coexistence behavior has also been observed for polycrystalline bulk samples [11]. From the critical temperatures a magnetic phase diagram in small aligning fields was derived. In contradistinction to the phase diagram established for polycrystalline samples in a high aligning field [11], at low temperatures a coexistence region of AF and FM contributions was found for the complete ROH. The crystalline coherence also plays a major role in the compositional dependence of the critical temperatures. Furthermore, outside the ROH in the Fe-rich region, indications of readily formed SPM Fe clusters were found. This observation is based on XRD patterns and the analysis of the composition-dependent magnetization and anisotropy behavior in the respective compositional range. The magnetization reversal depending on temperature suggests that a weak antiferromagnetism is stabilized in the ROH, distinctly observable at the stoichiometric point. In contrast to bulk samples, a magnetization is more easily induced in the thin films by an external magnetic field and the saturation field is much lower. Structurally-induced differences between the coupling constants may be responsible. This topic will be discussed in more detail in chapter 7.

Finally, a comparison of the magnetic properties was performed with thin films that are less ordered due to their significantly lower deposition temperature. As a result, the less-ordered samples exhibit no AF signatures in their magnetization behavior, emphasizing the importance of the sublattice order for the long-range magnetic order. The shape anisotropy dominates the small crystalline anisotropy in the disordered Fe/Ti regions, as is apparent from the magnetization isotherms. A significant out-of-plane contribution is added by the FM crystalline C14 phase volume fraction.

These observations indicate that epitaxially grown thin films offer an alternative pathway to the understanding of the metallurgy and the magnetic properties of $TiFe_2$ in the C14 stability range. The bulk samples examined in the literature so far are always prepared from the melt in a thermal equilibrium state. In the case of $TiFe_2$, Fe is easily precipitated, thus influencing the formation of the C14 phase and probably reducing the ROH for bulk samples to zero width at room temperature. Epitaxial thin films do not seem to suffer from this behavior, exhibiting crystalline phase purity and no indications for Fe precipitates. The magnetic properties support this picture and reflect the magnetism of pure Ti_xFe_{1-x} in the C14 stability range. However, it must not be neglected that the shape anisotropy is pronounced for thin films, and an increased crystal defect density is typical for epitaxial thin films as compared to single crystalline bulk samples.

Chapter 7

Monte Carlo simulations of a diluted Ising antiferromagnet

From the magnetization data of the epitaxial (001)-grown films it was concluded that for all compositions regions of AF and FM order coexist. The ratio of these regions is determined by the composition. For near-stoichiometric compositions predominantly AF behavior is found. The FM contributions continuously grow with increasing deviation from stoichiometry. As will be shown in this chapter Monte Carlo simulations employing an adequately chosen model Hamiltonian yield considerable insight into the interplay of chemical order of the Ti- and Fe-sublattices and the shape of the magnetization curves. The simulations not only allow for the establishment of a magnetic phase diagram but also the studying of the formation mechanisms of the differently ordered magnetic regions on a microscopic scale. After a brief introduction to Monte Carlo simulations and Ising-like systems in section 7.1, a model for an antiferromagnet, diluted by randomly distributed ferromagnetic impurities, will be proposed in section 7.2. Following in section 7.3 is the description of a graphical user interface (GUI) based C++ computer program which was specifically designed for the simulation of two and three dimensional Ising-like systems. The results of these simulations will be discussed in section 7.4. After a few comments on the problems and open questions of the simulations in section 7.5 the chapter concludes in section 7.6.

7.1 Monte Carlo simulations, algorithms and the Ising model

In this section a few introductory remarks on the Monte Carlo (MC) approach are given. For details the book of Landau and Binder [85] is warmly recommended. In solid state physics, typically a large number of particles is involved. This large number does not permit an exact analytical solution of Newton's equations if a classical approach is sufficient to begin with. In equilibrium statistical mechanics, the determination of thermal averages in many-particle systems are the main task of calculations. With the Monte Carlo simulation method a powerful tool for the treatment of such problems is available, taking proper account of statistical fluctuations in the analyzed system. Since standard Personal Computers (PC) offer sufficient computational power to handle even systems with a large number of particles nowadays, an office may be easily turned into a (physics) laboratory. In this context, "large numbers" is to be understood as an amount of particles, for which the simulations come close to the results for the by magnitudes larger numbers in macroscopic systems. The effect of finite size systems has to be analyzed for each problem separately.

In MC simulations, the path through phase space in a stochastically evolving system is followed by a sequence of numbers related to the system which are (pseudo-)randomly generated by a computer. Consequently, for different experiments with identical constraints the results will not be exactly the same. However, they will come close to each other within a statistical error, related to the length of the sequence of random numbers. Thus, the accuracy can be controlled by the number of steps performed during the simulation.

If MC algorithms are applied to problems of statistical physics, the time-dependent evolution of the system is reproduced by consecutive steps performed during the simulation. In this case, there is no direct connection or proportionality of real time and simulation time. Each step of the simulation may correspond to an infinitesimal small time, virtually separating two coinciding real-time events. In this manner, the time evolution of (more or less) independent particles in a many-body system can be mapped to the successive flow of a linear algorithm. In this context, it is an important precondition that the stochastic model (e.g. stochastic Ising model) can be described by means of a Markov chain. Below, S_i $(i = 1 \dots n)$ denotes the set of the possible states of the system. The state of the process at discrete times t_j, labelled consecutively $t_1, t_2, \dots, t_n$, is X_{t_j}. X_{t_j} is always equal to one of the states S_i. The conditional probability that the system at time t_n is in the state S_{i_n}, given that the system at preceding times was in well defined states, is consequently [85]:

$$P(X_{t_n} = S_{i_n} | X_{t_{n-1}} = S_{i_{n-1}}, X_{t_{n-2}} = S_{i_{n-2}}, \dots, X_{t_1} = S_{i_1}) \tag{7.1}$$

In a Markov process, all process steps at times t_{n-2} and earlier are forgotten and the resulting conditional probability can be interpreted as the transition probability from state i to state j [85],

$$W_{ij} = W(S_i \to S_j) = P(X_{t_n} = S_j | X_{t_{n-1}} = S_i) \tag{7.2}$$

Furthermore, the probabilistic property of W_{ij} requires

$$W_{ij} \geq 0, \qquad \sum_j W_{ij} = 1 \tag{7.3}$$

With t treated as a continuous variable the total probability $P(S_j, t) = P(X_{t_n} = S_j)$ that the state S_j is realized at time t_n, is equal to $W_{ij}P(X_{t_{n-1}} = S_i)$ [85]. The time evolution of this probability is given by the master equation [85]:

$$\frac{dP(S_j,t)}{dt} = -\sum_i W_{ji}P(S_j,t) + \sum_i W_{ij}P(S_i,t) \tag{7.4}$$

This equation can be interpreted as a continuity equation for the probability, conserving the total probability $\sum_j P(S_j, t) = 1$. In the case of the stochastic Ising model (see below), which is a relaxational model, the time-dependence can be described by this master equation [86].

Simple Monte Carlo sampling methods just randomly choose single points (i.e. particles or sites in a lattice) and weigh the value of the corresponding variable, for example, with respect to the total number of points. These methods gain accuracy with an increasing number of trials but for most problems the convergence is very slow. Importance sampling Monte Carlo methods take advantage of selection of points according to the importance of their contribution and consequently improve the speed of convergence. A simple method employing importance sampling is given by the Metropolis algorithm [87]. This algorithm is applicable for many problems and known for its simplicity. Since this algorithm was employed for most of the simulations, it shall be briefly discussed in the following within the framework of the stochastic Ising model.

The probability of a system being in the state n or m at time t is given by $P_n(t)$ and $P_m(t)$, respectively. Furthermore, the transition rate from state n to m is denoted by $W_{n\to m}$. If a model can be described by a master equation according to equation 7.4, in equilibrium it must follow $\partial P_n(t)/\partial t = 0$. The resulting expression is the *detailed balance*

$$P_n(t)W_{n\to m} = P_m(t)W_{m\to n} \tag{7.5}$$

Any transition rate $W_{n\to m}$ and $W_{m\to n}$ may be chosen if they satisfy equation 7.5. The Metropolis algorithm employs a special transition rate which depends on the energy difference between initial and final state. For a classical system the probability of a state n is given by

$$P_n(t) = e^{-\frac{E_n}{k_\mathrm{B}T}}/Z \tag{7.6}$$

with E_n the energy of state n, the Boltzmann constant k_B, the temperature T and the partition function Z. Since Markov processes follow the master equation, only the relative probabilities for a transition from state m to state n, given by $P_n(t)/P_m(t)$, are important and Z is eliminated from equation 7.6. According to Metropolis [87], detailed balance is found for

$$\begin{aligned} W_{m\to n} &= \tau_0^{-1} e^{-\frac{\Delta E}{k_\mathrm{B}T}}, \qquad && \Delta E > 0 \\ &= \tau_0^{-1}, && \Delta E < 0 \end{aligned} \tag{7.7}$$

with $\Delta E = E_n - E_m$. The time τ_0 is the time required to attempt a transition between these states.

A common example for systems, which can be handled by importance sampling MC algorithms, is the Ising model. It assumes sites on a lattice occupied by spins σ_i which point either up ($\sigma_i = +1$) or down ($\sigma_i = -1$). The next neighbor spins are coupled by an exchange interaction with coupling constant $\mathcal{J}$. Furthermore, the spins may interact by a Zeeman interaction with an external magnetic field H. The Hamiltonian can thus be written as

$$\mathcal{H} = -\mathcal{J} \sum_{<i,j>} \sigma_i \sigma_j - \mu_0 \mu_\mathrm{B} H \sum_i \sigma_i \tag{7.8}$$

The summation is performed over the whole lattice. The next neighbors interaction is indicated by the index $<i,j>$. The one dimensional model has been solved exactly. The two dimensional model was solved by Onsager [88] for the thermal properties of $L \times M$ lattices with periodic boundary conditions. The exact solution for an infinite two dimensional Ising lattice is given by [89]

$$\frac{M(T)}{M(T=0)} = \left[1 - \sinh^{-4}\left(\frac{2\mathcal{J}}{k_\mathrm{B}T}\right)\right]^{1/8} \tag{7.9}$$

The Metropolis algorithm can now be formulated for an Ising lattice considering equation 7.7 in the following way [85]:

1. Choose an initial (random) state
2. Randomly select a site i
3. Calculate ΔE for the hypothetically flipped spin at site i
4. Generate a random number $r \in]0, 1[$
5. If $r < e^{-\Delta E/k_\mathrm{B}T}$, flip the spin
6. Goto step 2

The standard measure for the MC time is the number of Monte Carlo steps per site (MCS/site). During a single MCS each site is visited once in average. In order to test the correctness of the implementation of the Metropolis algorithm, several simulations were performed with periodic boundary conditions for the two- and three-dimensional Ising ferromagnet. In Fig. 7.1 examples are shown for both types. The 2D Ising simulation is compared to the theoretical curve according to equation 7.9 and is found to be in good agreement with the theoretical curve. The 3D Ising simulation corresponds to the expected behavior, too. At the critical temperature significant fluctuations are observed. This phenomena is called *critical slowing down*. The large spatial correlations on approach of the critical point are associated with diverging correlation times.

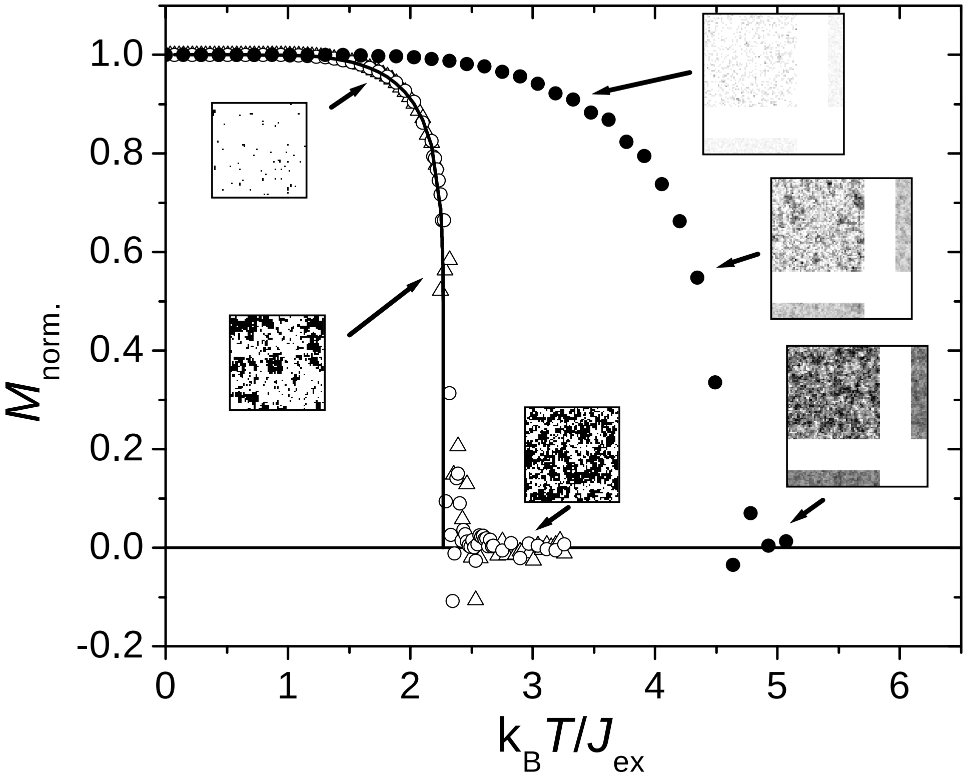

Figure 7.1: Simulated susceptibility of a 2D (open symbols) and 3D Ising ferromagnet (full circles) employing the Metropolis method. The lattice size was 60×60 for the 2D and 60×60 ×10 for the 3D simulation. The theoretical curve according to equation 7.9 (full line) is compared to the 2D data. At several temperatures during the simulation the current state of the lattice is illustrated by images: for the 2D data the black/white contrast indicates $\sigma_i = -1/+1$. For the 3D data a combined view from top, front and side with averaging about the viewers direction, which was mapped to a grey scale, is presented.

For relaxational models, such as the stochastic Ising model, the simulation time is different from real time and the long (simulation) time behavior of the relaxation function $\phi_{MM}(t)$

$$\phi_{MM}(t) = \frac{\langle M(0)M(t)\rangle - \langle M\rangle^2}{\langle M^2\rangle - \langle M\rangle^2} \tag{7.10}$$

which is the auto-correlation function of M follows an exponential law [85]

$$\phi_{MM}(t) \rightarrow e^{-t/\tau} \tag{7.11}$$

The relaxation time τ can be expressed by means of a critical power law [85]

$$\tau \propto \xi^z \propto \varepsilon^{-\nu z} \tag{7.12}$$

with the correlation length $\xi = \xi_0 \varepsilon^{-\nu}$, $\varepsilon = |1 - T/T_\mathrm{C}|$ and its critical exponent ν. z is in this context the critical dynamical exponent describing the relaxation (simulation) time behavior of the underlying model in connection with the used algorithm. For the stochastic Ising model as simulated by the described Metropolis algorithm, z is slightly larger than 2 [85], resulting in the critical slowing down observed in Fig. 7.1.

The critical slowing down can efficiently be reduced by alternative algorithms like cluster flipping methods. The Swendsen-Wang method [90] reduces the dynamical critical exponent to $z \sim 0$ in two dimensions and $z \sim 0.5$ in three dimensions [91]. The additional computation time due to the increased complexity of the cluster flipping methods must be carefully evaluated against the reduction of z. A further reduction of computational time can be achieved by the Wolff method [92] which was applied to the simulations shown in Fig. 7.2: the effect of the critical slowing down at T_C has vanished. The deviations from the theoretical curve at T_C are due to the finite size of the simulation lattice.

For the simulations described in section 7.3 and 7.4 the Metropolis algorithm was preferred. The advantage of the Metropolis method is its simplicity in connection with the increased complexity of the model proposed in the next section. Furthermore, no simple way to include external magnetic fields in the proposed model was found for the Wolff method.

Finally, care must be taken that ergodicity is maintained for the used algorithm. Each possible state in phase space of the system must be attainable by a non-vanishing probability. If this is not fulfilled, incorrect results may be obtained. For the Metropolis algorithm non-ergodicity occurs for very high temperatures [85]. In this case, the probability for a spin-flip approaches one, and during each MCS the whole spin-lattice is inverted. However, if temperatures are low, the approach remains ergodic. In some cases, ergodicity may be intentionally violated. In case of the Ising system, all possible states are two-fold degenerate and it may be desirable to keep the simulation in one half of phase space.

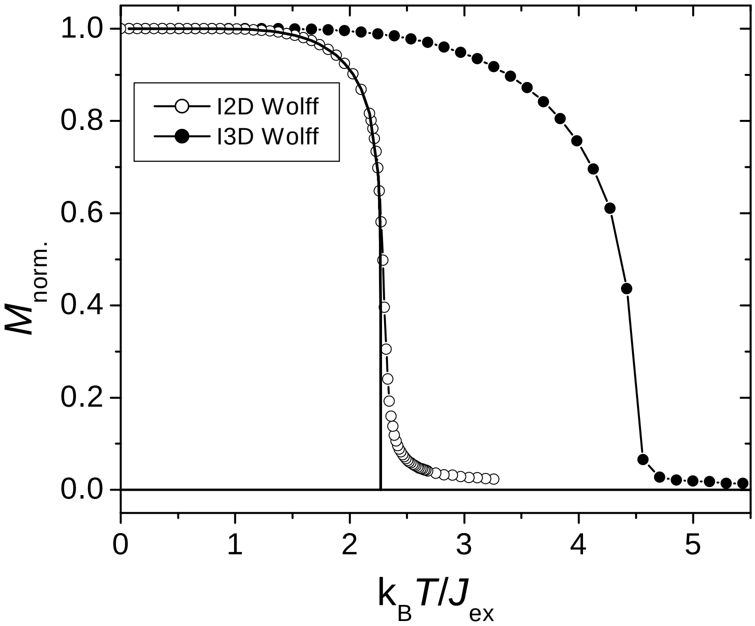

Figure 7.2: Simulated susceptibility of a 2D (open symbols) and 3D (solid symbols) Ising ferromagnet employing the Wolff cluster flipping method. The lattice size is 100 × 100 for the 2D and 60 × 60 × 10 for the 3D data. The theoretical curve according to equation 7.9 (full line) is compared to the 2D data.

7.2 Proposed Hamiltonian

From the magnetization data presented in chapter 6 a composition-dependent transition from predominantly AF behavior at the stoichiometric point to AF/FM coexistence behavior for off-stoichiometric compositions was deduced. In the model suggested here, this transition is caused by a dilution of the AF by an increasing number of FM coupling impurity sites forming FM clusters. In this context, the FM coupling is induced by the substitution of Fe on Ti antisites or Ti on Fe antisites, disturbing the symmetry of the unit cell. In the following, a Hamiltonian will be suggested which considers this formation of FM coupling impurity sites with deviations from stoichiometry and may allow for a check of the validity of the model and the determination of the nature of the clustering. This Hamiltonian was used for the MC simulations analyzed in section 7.4.

Two different types of lattice sites are to be distinguished in the model: A sites corresponding to the AF stoichiometric composition and B sites for the FM off-stoichiometric composition. The A sites couple antiferromagnetically in z-direction with A sites (coupling constant $J_{\mathrm{AA}.z} < 0$) and ferromagnetically with B sites ($J_{\mathrm{AB}.z}, J_{\mathrm{BA}.z} > 0$). The in-plane coupling of A sites with either kind of sites is always FM ($J_{\mathrm{AA}.xy} > 0$, $J_{\mathrm{AB}.xy} > 0$,$J_{\mathrm{BA}.xy} > 0$). B sites couple FM with B

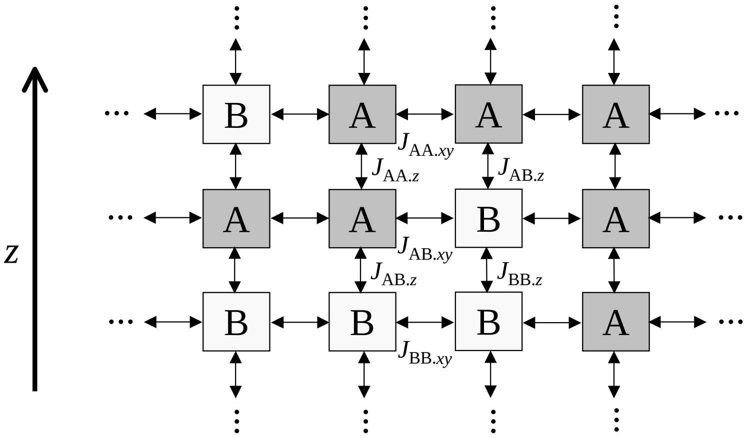

Figure 7.3: Illustration of the coupling constants as introduced in the diluted AF model. The AF coupling sites are denoted by A and the FM coupling sites by B. The coupling is indicated by arrows.

sites in x-,y- and z-direction ($J_{\mathrm{BB}.z} > 0$, $J_{\mathrm{BB}.xy} > 0$). The z-direction corresponds to the c-direction in TiFe$_2$. One possible configuration is illustrated in Fig. 7.3. In this way, the AF layered structure of the Fe(6h) atom (see Fig. 1.1) is reproduced if the lattice consists only of A sites, as depicted on the left of Fig. 7.4. The off-stoichiometric compositions correspond to a partial occupation of the lattice with B sites, illustrated on the right of Fig. 7.4.

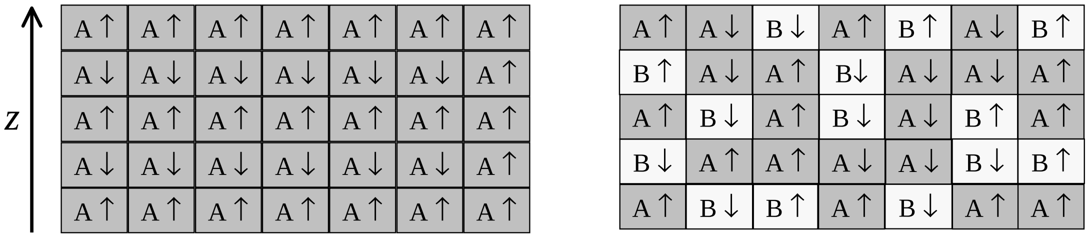

A↑	A↑	A↑	A↑	A↑	A↑	A↑
A↓	A↓	A↓	A↓	A↓	A↓	A↑
A↑	A↑	A↑	A↑	A↑	A↑	A↑
A↓	A↓	A↓	A↓	A↓	A↓	A↑
A↑	A↑	A↑	A↑	A↑	A↑	A↑

A↑	A↓	B↓	A↑	B↑	A↓	B↑
B↑	A↓	A↑	B↓	A↓	A↓	A↑
A↑	B↓	A↑	B↓	A↓	B↑	A↑
B↓	A↑	A↑	A↓	A↓	B↓	B↑
A↑	B↓	B↑	A↑	B↓	A↑	A↑

Figure 7.4: Lattice configuration for the diluted AF model. Left: Occupation probability $p = 0$ in the AF state. Right: $p = 0.4$ with a random orientation of the spins. See text for details.

In the present model, it is assumed that this occupation occurs randomly. An occupation variable c_i for each lattice site i is introduced. $c_i = 0$ if the site i is of type A and $c_i = 1$ if it is of type B. The predetermined probability distribution of the configurations $\{c_i\}$ is denoted $P\{c_i\}$. Typically, $P\{c_i\} = 1/N_{\{c_i\}}$ if $N_{\{c_i\}}$ is the number of possible configurations and the distribution is homogeneous. The relative occupation probability p of the lattice with type B sites for a given $\{c_i\}$ is then

$$p = \frac{1}{N}\sum_i c_i \tag{7.13}$$

N is the overall number of lattice sites. Following the properties of the Ising model, only two states $\sigma_i = \pm 1$ are allowed for the spins on each site and only next neighbor interactions are considered. The general Hamiltonian for the described model with spin configuration $\{\sigma_i\}$ in an external magnetic field H is then given by

$$\begin{aligned}
\mathcal{H}\{\sigma_i, c_i\} \;=\; & - \sum_{<i,j>_z} [(1-c_i)c_j J_{\mathrm{AB}.z} + c_i(1-c_j) J_{\mathrm{BA}.z} + c_i c_j J_{\mathrm{BB}.z} \\
& + (1-c_i)(1-c_j) J_{\mathrm{AA}.z}]\sigma_i\sigma_j \\
& - \sum_{<i,j>_{xy}} [(1-c_i)c_j J_{\mathrm{AB}.xy} + c_i(1-c_j) J_{\mathrm{BA}.xy} + c_i c_j J_{\mathrm{BB}.xy} \\
& + (1-c_i)(1-c_j) J_{\mathrm{AA}.xy}]\sigma_i\sigma_j \\
& - \mu_0\mu_{\mathrm{B}} H \sum_i \sigma_i
\end{aligned} \tag{7.14}$$

The summation indicated by the index $<i,j>$ is limited to the next neighbors. Via $\{c_i\}$ even non-homogeneous distributions of FM coupling sites may be realized, e.g. clusters. Considering symmetry, $J_{\mathrm{BA.i}} = J_{\mathrm{AB.i}}$ $(i = xy, z)$, 7.14 reduces to

$$\begin{aligned}
\mathcal{H}\{\sigma_i, c_i\} \;=\; & - \sum_{<i,j>_z} [(c_i + c_j - 2c_i c_j) J_{\mathrm{AB}.z} + c_i c_j J_{\mathrm{BB}.z} + \\
& +(1-c_i)(1-c_j) J_{\mathrm{AA}.z}]\sigma_i\sigma_j - \\
& - \sum_{<i,j>_{xy}} [(c_i + c_j - 2c_i c_j) J_{\mathrm{AB}.xy} + c_i c_j J_{\mathrm{BB}.xy} \\
& +(1-c_i)(1-c_j) J_{\mathrm{AA}.xy}]\sigma_i\sigma_j - \\
& -\mu_0\mu_{\mathrm{B}} H \sum_i \sigma_i
\end{aligned} \tag{7.15}$$

This expression is inspired by a Hamiltonian used for the simulation of systems with quenched randomness, such as binary alloys prepared from the melt [85]. In the present case, for the internal energy calculations the magnetic moment of a single spin was set to $|\vec{m}_\sigma| = 1\mu_{\mathrm{B}}$.

7.3 C++ implementation of the MC algorithms on a standard PC

For the simulations performed in this work the corresponding algorithms were implemented using the programming language C++. A GUI was added by usage of the Microsoft Foundation Class libraries allowing for an intuitive access to the implemented functions.

7.3.1 Random numbers

The first problem encountered is the "randomness" of the random number generator used for the MC simulations. Correlations of pseudo-random numbers generated by a computer may lead to strong deviations from the expected behavior of a MC simulation [85]. In the present case, two different generators were made accessible: (1) the standard random number generator from the Microsoft Visual C++ libraries, seeded by the realtime clock of the computer; and (2) the R250/R521 generator [93], as a modification of the Tausworthe algorithm, following the FORTRAN implementation given in [85]. The R250/R521 is seeded by the standard C++ generator initialized by the computer's time variable. Various tests were performed to check for the "randomness" of the generators. First, the convergence of the mean value towards the expectation value of a very long row of random numbers was tested. Second, the mean value of the L^2 successors were mapped to a grey scale and displayed on an $L \times L$ pixel image on the computer screen. Correlations of random numbers may then be identified by patterns in these images. Third, the Wolff cluster flipping algorithm was applied to the Ising 2D and 3D ferromagnet. Since the results of the Wolff algorithm are known for their sensitivity to correlations in random numbers [85], correlated random numbers may result in differences between different generators. Finally, the different generators were applied to the present model according to the Hamiltonian given in equation 7.15, and the results were compared. In summary, both generators were found to generate random numbers within the limits of the underlying test. Simulations with identical parameters and different generators proved identical results. However, after comparison of the autocorrelation function $\phi_{MM}(t)$ of the order parameter M in long-time runs, it turned out that for the standard C++ generator periodic peaks occurred which were not present for the R250/R521 generator. This indicates that the C++ generator produces equal sequences of numbers with an approximate periodicity of 5.5×10^8. Consequently, the R250/R521 generator was used for the simulations of $TiFe_2$, with the drawback of being 20% slower than the standard C++ generator. Sample checks with the C++ generator were made if the results appeared critical to randomness but did not result in significant deviations.

7.3.2 Simulation setup

Depending on the current simulation mode, the client window displays different graphical representations of the respective lattice. See the appendix for details concerning the program usage. For the 2D Ising model, each spin value is represented by a black ($\sigma_i = -1$) or a white ($\sigma_i = +1$) pixel. For the 3D Ising and the $TiFe_2$ model, a split view displays the lattice from the top, the front and the side. In this context, each pixel's grey value represents an average of the normalized lattice magnetization in the respective view direction, ranging from black ($M_{\mathrm{av}} = -1.0$) to white ($M_{\mathrm{av}} = +1.0$). The setup menu of the simulation provides the setting of various simulation parameters. The two random number generators described above may be selected for each model. Additionally, for the 2D and 3D Ising models, the Wolff algorithm may be chosen as an alternative to the Metropolis algorithm. Three different boundary conditions are to be distinguished:

1. Free boundary conditions

   The boundary sites are left without next neighbors outside the boundary.

2. Periodic boundary conditions

   The next neighbors of the boundary sites are situated on the opposite side of the lattice.

3. Thin film boundary conditions

   Periodic boundary conditions in the x-y-plane and free boundary conditions along the z-axis

Further parameters are the dimension of the respective lattice and the separate coupling constants for the Ising and the $\mathrm{TiFe_2}$ model. Finally, the occupation probability p (called *wk_fm* in the program) can be set in the range from 0.0 to 1.0. According to p an exact fraction $p \cdot L^2$ is occupied by FM coupling impurity sites. Another method of occupying the lattice with impurity sites would be to draw a random number for each site. By checking against p it is decided whether the site is B-type or not. However, the latter method leads to differences at least in the self-averaging behavior of the model [94]. Thus, in the present simulation the former method was used.

The simulation may be performed manually as well as controlled by a script. The temperature T[K] and an external field H[Oe] along the z-axis can be set by the respective command. Subsequently, a given number of MCS is performed. In average, during each MCS each lattice site is visited once. The net lattice magnetization is then stored in a ring buffer which contains a predefined number of the previous magnetization values [1]. The MC iteration stops if the standard deviation of the buffer's mean value is lower than a previously defined limit. Additionally, a maximum number of MCS must be defined to prevent an infinite running time. With this method, the relaxation behavior of the models is considered, allowing the system to relax within a given number of MCS. The consecutive steps contribute to the average magnetization. A large number of simulations with long running times may be performed by a script. Within this script all parameters

---

[1] In a ring buffer a new element to be added discards the oldest element

can be varied, including a loop statement for continuous variation. The generated data are stored into files of a previously defined name. Additionally, snapshot images can be saved.

It has to be mentioned that for each different calculation the simulation constraints have to be checked carefully to obtain reasonable results within a limited computing time. The number of MCS performed should be adjusted to the relaxation behavior.

7.4 Results of the simulations

Since each Hamiltonian employed for MC simulations may exhibit a different relaxation behavior, in a first step reasonable values for the minimum number of MCS to be performed before reaching thermal equilibrium had to be determined. This number is denoted n_{min} in the following. Different tests involving the variation of n_{min}, p and the coupling constants yielded an optimal $n_{\text{min}} \geq 500\,\text{MCS}$, after which the system seemed to be mostly relaxed. However, an accurate determination of n_{min} may be obtained from the autocorrelation function of the order parameter M in long-time runs. The non-linear relaxation function $\Phi_M(t)$ [85]

$$\Phi_M(t) = \frac{\langle M(t) - M(\infty)\rangle}{\langle M(0) - M(\infty)\rangle} \tag{7.16}$$

and the autocorrelation function $\Phi_{\text{auto}}(\tau)$ of $\Phi_M(t)$

$$\Phi_{\text{auto}}(\tau) = \frac{\langle \Phi_M(0)\Phi_M(\tau)\rangle - \langle \Phi_M\rangle^2}{\langle {\Phi_M}^2\rangle - \langle \Phi_M\rangle^2} \tag{7.17}$$

for $t_{\text{max}} = 1 \times 10^5\,\text{MCS}$ was determined for $p = 0.25$ and $p = 0.29$ at a magnetic field of $H_{\text{ext}} = 100\,\text{kOe}$ which was applied in most of the presented simulations. This relatively large aligning field, as compared to the experiment, was necessary to speed up relaxation. The relaxation time significantly decreases for increasing magnetic field. From this $\Phi_{\text{auto}}(\tau)$ the relaxation time τ_0 at T_{N} was estimated to be $\tau_0 \approx 3\times10^4$ MCS for a $100\times100\times10$ lattice for $p = 0.25$ (see Fig. 7.5) and $p = 0.29$. τ_0 was determined for selected temperatures and found to significantly decrease below T_{N} (see Fig. 7.5). This allows for a further reduction of the simulation time by adjusting the minimum number of MCS at a given temperature to the resulting $\tau_0(T)$-curve. This equilibrium condition will be denoted $n_{\text{equi}}(T)$ in the following. The mean value of the order parameter $M(T)$ at a given temperature was determined from the average of 1000 MCS following the $n_{\text{min}} \equiv n_{\text{equi}}(T)$ MCS necessary for relaxation. All simulation described below were performed on a $100 \times 100 \times 10$ lattice as a compromise of simulation time and finite size effects.

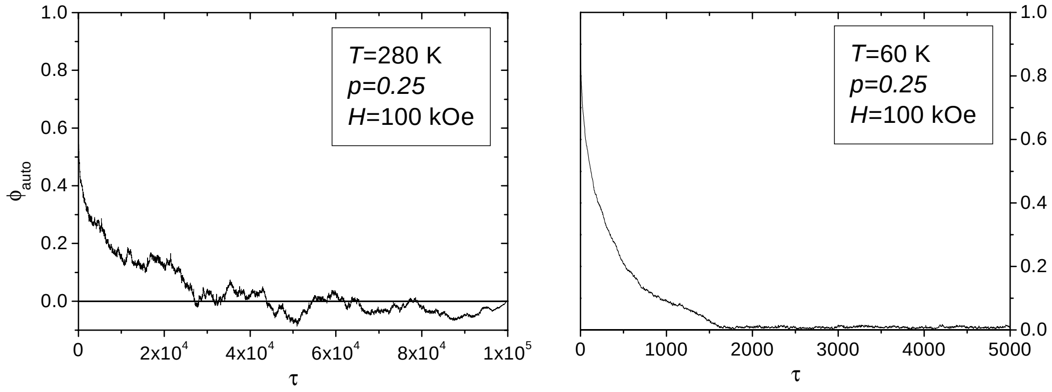

Figure 7.5: Autocorrelation function Φ_{auto} as a function of the time displacement τ for $p = 0.25$ and $H_{\text{ext}} = 100\,\text{kOe}$ at $T = 280\,\text{K}$ (left) and $T = 60\,\text{K}$ (right).

7.4.1 Results for $M(T)$

Determination of the simulation parameters

The large number of parameters contained in the present model complicates the determination of an appropriate set of parameters. These must fulfill the condition that susceptibility curves generated with these parameters are in agreement with the experimental susceptibility data (see section 6.1) and that the parameters are physically meaningful. The magnitude of the coupling energies can be expected to be in the range known for simple magnetic materials. For example, the mean field approximation yields $J = 11.9\,\text{meV}$ for Fe [72] which can be used as a guideline to start from. The resulting susceptibility data generated with $J_{\text{xx}} = 11.9\,\text{meV}$ (xx $\neq$ AA.z), $J_{\text{AA.z}} = -11.9\,\text{meV}$ and variable p are shown in Fig. 7.6 for $n_{\text{min}} = 500$. For $p = 0.0$ an AF like curve with $T_{\text{N}} \simeq 640\,\text{K}$ is found. The normalized magnetization decreases to zero as $T \to 0\,\text{K}$. T_{N} decreases on increase of p due to the dilution of the antiferromagnet by the FM coupling impurity sites. Simultaneously, the induced magnetization increases with p. For $p > 0.2$ the shape changes within $\Delta p = 0.1$ to an FM type curve with $T_{\text{C}} \approx 500\,\text{K}$. Remarkably, at low temperature the magnetization significantly increases for almost all curves, giving indications of small FM clusters ordering at much lower temperatures as compared to the long range ordered AF and FM background.

Comparing these results to the experimental susceptibility data it is found that the overall AF/FM transition behavior is reproduced. However, the respective ordering temperatures appear at too large values and, which is more important, in the FM-like regions T_{N} cannot be identified. This is most likely due to the wrong ratio of T_{N} and T_{C}. To account for these problems several simulations

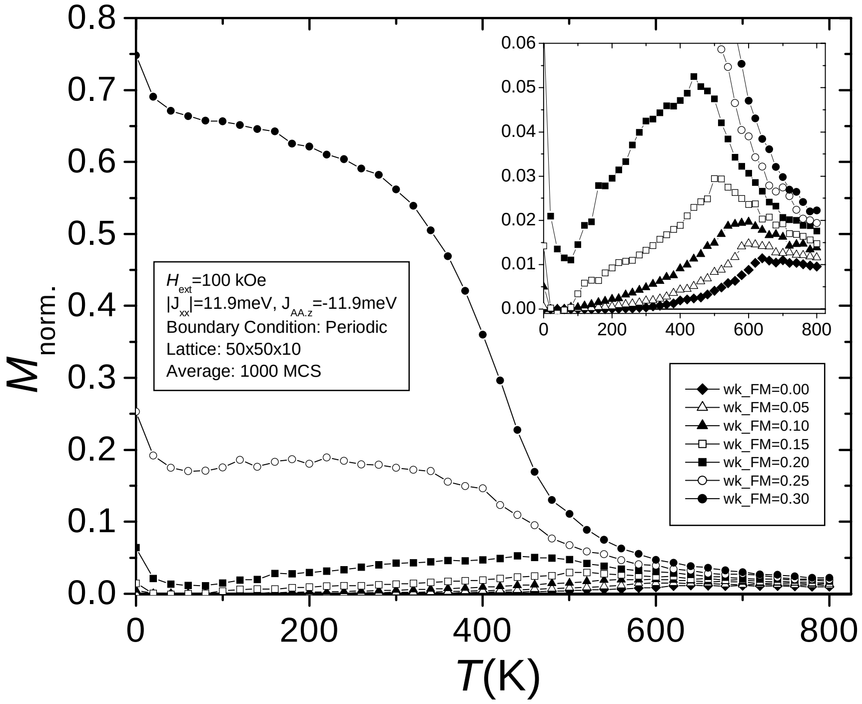

Figure 7.6: Simulated susceptibility for $J_{\text{xx}} = 11.9\,\text{meV}$ (xx $\neq$ AA.z) and $J_{\text{AA.z}} = -11.9\,\text{meV}$. The cooling was performed in an external magnetic field $H_{\text{ext}} = 100\,\text{kOe}$. The inset shows an expansion of the small M region. See text for details.

with varying coupling constants were performed. The conclusions drawn are the following:

1. To observe a minimum at T^* it is necessary that $T_{\text{C}} < T_{\text{N}}$. This can only be achieved if the average AB and BB coupling constants are chosen smaller than the absolute AA values.

2. A reduction of $J_{\text{AB.z}}$ and $J_{\text{BB.z}}$ with respect to $|J_{\text{AA.z}}|$ results in AF $M(T)$-curves up to large p-values. Nevertheless a transition to FM-like curves occurs for larger p, but the strong dilution of the AF at large p reduces T_{N} to $T_{\text{N}} < T_{\text{C}}$. A reduction of $J_{\text{AB.xy}}$ and $J_{\text{BB.xy}}$ with respect to $|J_{\text{AA.xy}}|$ results in $T_{\text{C}} < T_{\text{N}}$ while retaining the AF/FM coexistence behavior.

3. The in-plane coupling constants must be chosen relatively large with respect to the out-of-plane constants to retain the layered magnetic structure of the antiferromagnet.

After following these rules as a guideline for the ratio of the coupling constants and adapting the absolute values to the experimental data a standard set of parameters was determined (see table 7.1).

	xy	**z**
AA	11.9 meV	-2.0 meV
AB	5.0 meV	2.0 meV
BB	5.0 meV	2.0 meV

Table 7.1: Standard coupling constants determined from heuristic principles (see text for details).

Standard coupling constants and double averaging

The results for these standard coupling constants are shown in Fig. 7.7 for $n_{\mathrm{min}} = 500$. Starting from small p the curves exhibit a similar behavior as compared to Fig. 7.6: T_{N} decreases with p and M drops to zero at low temperatures due to AF ordering. In contradistinction to Fig. 7.6 the complete data collapse on a single curve in the PM temperature region. For large p (e.g. $p = 0.25$) the distinct coexistence behavior which was also observed in the experimental susceptibility curves, can be recognized: below a local maximum of M at T_{N} a local minimum is found at T^* which is the onset of ferromagnetism in the FM ordering regions of the lattice. For even larger p the lattice becomes preferably FM and allows for complete parallel alignment of the spins at lower temperature for $p \geq 0.3$. However, T_{N} remains visible as a bump on the increasing curve for all $p \leq 0.3$.

For $p > 0.2$ an anomalous behavior is observed. The shape of the curves switches apparently randomly between an overall AF-type curve with $M \to 0$ for $T \to 0$ and a coexisting AF/FM type curve exhibiting an increase of M at lower temperature. Furthermore, if the simulation for a specific p is repeated with either (1) a different random or (2) an identical $\{c_i\}$ of impurity sites, the resulting curves are distributed about the arithmetic mean curve with more or less pronounced contributions of FM ordering regions. This behavior can be attributed to a combination of different effects. First, as known from other systems with quenched randomness, with the introduction of an additional random variable, in the present case $\{c_i\}$, which is kept fixed during the simulation, a second averaging has to be carried out over the distribution $P\{c_i\}$ [85]

$$\left[\langle M\{\sigma_{i_j}, c_i\}\rangle_T\right]_{\mathrm{av}} = \int d\{c_i\}\, P\{c_i\} \frac{1}{Z\{c_i\}} \mathrm{Tr}_{\sigma_i} \left(M\{\sigma_i, c_i\} \exp[-\mathcal{H}\{\sigma_i, c_i\}/k_{\mathrm{B}}T]\right) \tag{7.18}$$

with the partition function $Z\{c_i\}$ of the configurations $\{c_i\}$ and the spin configurations $\{\sigma_i\}$. The squared brackets on the left side indicate this additional average over the $\{c_i\}$, whereas the thermal average is indicated by the the subscript T. Consequently, several magnetization curves with constant p but random $\{c_i\}$ have to be simulated, i.e. Metropolis importance sampling for the thermal

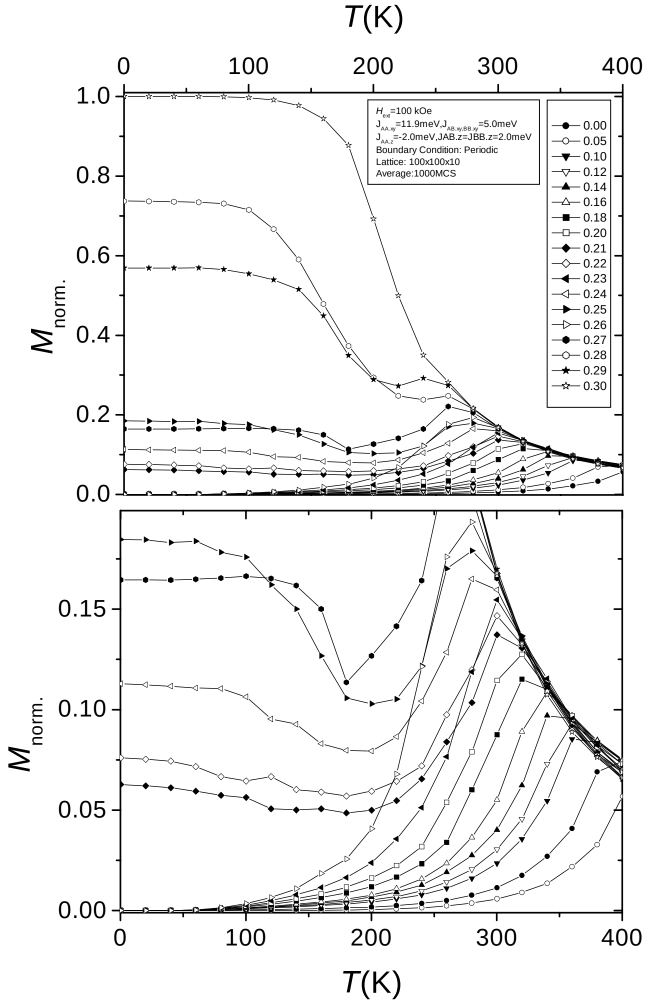

Figure 7.7: Simulated susceptibility for standard coupling constants (see annotation in the figure). The cooling was performed in an external magnetic field $H_{\mathrm{ext}} = 100\,\mathrm{kOe}$. Bottom: Expansion of the top figure with small p.

average $\langle \ldots \rangle_T$ and simple sampling for the configuration average $[\ldots]_{\mathrm{av}}$. Second, another problem is generated by multiple near-degenerate minima of the free energy which are also found for spin glasses [85]. The relaxation to the absolute minimum is very slow at low temperatures and the computation time thus becomes very large. However, the double averaging described above may also help to find the absolute minimum. An increase of the lattice size was found to not significantly help solving these problems by self-averaging. As is known from the analysis of the order parameter about T_{C} for systems with quenched randomness [85,95] a lack of self-averaging occurs, as found for the present system.

As an illustration, in Fig. 7.8 the distribution of independent $M(T)$ simulations with $p = 0.25$ and $p = 0.27$ is shown for $n_{\min} = 500$. The low temperature magnetization is widely distributed and the position of the local minimum differs slightly for each curves. In contradistinction, T_{N} is fixed at $T \cong 260\,\mathrm{K}$ and the curves collapse on one curve above T_{N}.

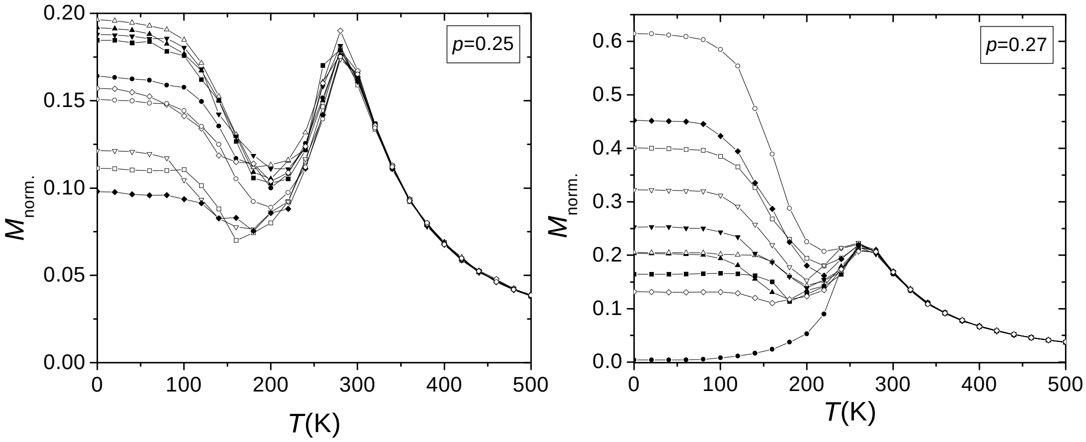

Figure 7.8: Distribution of independent $M(T)$ simulations with $p = 0.25$ (left) and $p = 0.27$ (right) using standard coupling constants. Each curve is generated with the same number of impurity sites but different configurations $\{c_i\}$.

Results for $\overline{M}(T)$

The average behavior of $M(T)$ as a function of p was determined by averaging over 10 simulations at an applied field $H_{\mathrm{ext}} = 100\,\mathrm{kOe}$. Different random configurations $\{c_i\}$ were chosen for $n_{\min} = 500$ ($p = 0.20, 0.21 \ldots 0.30$) and $n_{\min} = n_{\mathrm{equi}}(T)$ ($p = 0.26, \ldots 0.31$). The differences between these simulation series then must be related to the insufficient relaxation for $n_{\min} = 500$. The results are shown in Fig. 7.9 as a function of the reduced temperature $T_{\mathrm{norm.}} = T/T_{\mathrm{N}}^0$. $T_{\mathrm{N}}^0 = 278\,\mathrm{K}$ is taken from the $n_{\min} = n_{\mathrm{equi}}(T)$ data with $p = 0.26$. In this case, $p = 0.26$ corresponds to the largest value for which purely AF behavior was found. The transition from predominantly AF to predominantly FM behavior with increasing p is now mostly reproduced by the data of both series. T_{N} decreases with increasing p due to the dilution of the AF. A few overlapping regions are found at small p and $n_{\min} = 500$ which is most probably related to the small number of averaging points. However, the deviations remain within the error bars which are calculated as the standard error of the mean value.

$n_{\min} = 500$: Between $p = 0.20$ and $p = 0.24$ the data almost collapse on one curve with a non-zero magnetization in the low temperature range. The

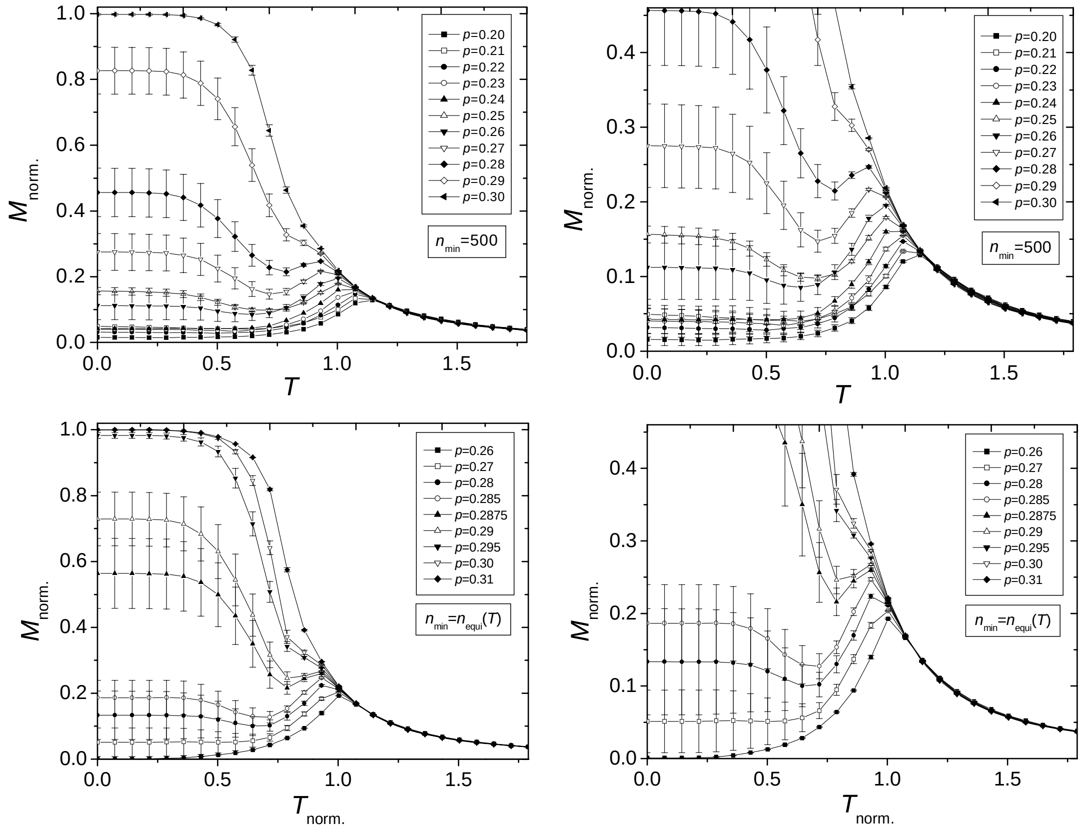

Figure 7.9: Arithmetically averaged $\overline{M}(T)$ of 10 simulations with different $\{c_i\}$ but constant p. The temperature was normalized to $T_\mathrm{N}^0 = 278\,\mathrm{K}$ of the $p = 0.26$ data for $n_\mathrm{min} = n_\mathrm{equi}(T)$. The error bars are the standard error of the mean value. The right figures show an expansion of the left figure. Top: Results for $n_\mathrm{min} = 500$. Bottom: Results for $n_\mathrm{min} = n_\mathrm{equi}(T)$.

transition from predominantly AF to FM behavior sets in at $p \approx 0.25$, indicated by a pronounced increase of $M(T)$ at lower temperatures. At $p = 0.30$ the susceptibility data exhibits an almost FM shape and is completely saturated below $T_\mathrm{norm.} = 0.4$. Nevertheless, at $T_\mathrm{norm.} \approx 1.1$ a small bump still indicates T_N and thus antiferromagnetism in the lattice. Due to the onset of ferromagnetism at lower temperatures the AF alignment is suppressed and the lattice may be saturated even in small aligning fields. As a result, the transition from predominantly AF to FM behavior occurs above $p = 0.25$ with a width $\Delta p = 0.05$.

$n_\mathrm{min} = n_\mathrm{equi}(T)$: In contradistinction, the onset for the transition is observed for $p \approx 0.28$. For $p = 0.31$ no indications of AF contribution are discernible. The width of the transition is thus only $\Delta p = 0.03$.

It can be stated that the transition of the non-relaxed system is shifted to smaller p. This implicitly means that for smaller p in the non-relaxed case FM contributions are frozen out which is supported by the non-zero low temperature magnetization even for $p = 0.20$. In the relaxed case a pure AF is found for $p \leq 0.26$.

Furthermore, it is noticed that a significant standard deviation σ_{av} of $\overline{M}$ is only found in the AF-to-FM/AF transition range. In Fig. 7.10 σ_{av} is plotted as a function of p for both simulation series. The error distribution is broader for the non-relaxed case, corresponding to the broader transition range, and exhibits an additional tail at smaller p. Considering the above mentioned possible origins of the errors it can now be stated that the errors mainly stem from the multiple minima energy landscape. Since the configuration averaging was performed identical for both series the broader error distribution for the non-relaxed case must be due to the insufficient number of MCS performed.

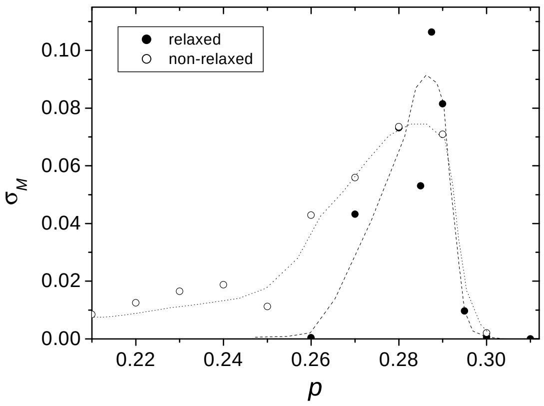

Figure 7.10: Standard errors of the mean value for the relaxed (solid symbols) and the non-relaxed series (open symbols). The dashed and dotted lines are to guide the eye.

Simulated magnetic phase diagram

As detailed in section 6.1.2, a magnetic phase diagram was determined from the characteristic temperatures observed in the $M(T)$-data of the epitaxial samples. It is now desirable to compare these experimental data to the simulation results. From the simulation data of Fig. 7.9 the critical temperatures T_{N} and T^* were determined in accordance to the process described in Fig. 6.1. The resulting phase diagram for the relaxed series is depicted in Fig. 7.11. Δp denotes the deviation from $p = 0.26$ for which still a purely AF curve was generated in the simulations and which is assumed to represent the stoichiometric $\mathrm{TiFe_2}$ with a basic amount of disorder. According to the present model and to facilitate a comparison with the experimental data of Fig. 6.4 the determined critical temperatures were drawn symmetrically to either side of the diagram. The corresponding phase names, as identified for the experimental data, were added to the diagram.

If it is assumed that $x - \frac{1}{3}$ of the experimental data is proportional to Δp of the simulations the overall behavior of T^* is reproduced by the simulations for $0.30 < x < 0.38$ of the experimental data. Outside this range the properties of the film growth significantly influence the critical temperatures of the thin film phase diagram. Furthermore, for the Ti-rich region (corresponding to positive Δp in Fig. 7.11) the experimental temperatures T^* and T_N are significantly lower due to the lower crystalline coherence of the samples which is not included in the simulation. The decrease of T_N with increasing impurities is also reproduced by the simulations. The growth-induced shift of the maximum of the T_N with respect to the stoichiometric point of the experimental phase diagram can not be simulated due to the limitations of the underlying simulation model. The observed increase of T_N for large Δp is most probably related to the determination of T_N which can only performed coarsely due to the small signature of T_N in this region.

As can be seen in Fig. 7.12 the shape of the experimental $M(T)$ curves with the local maximum at T_N and the local minimum at T^* is reproduced for the nearly stoichiometric composition at $x = 0.34$ and the iron-rich composition at $x = 0.32$. The ratio of T_N and T^* is equal to the corresponding value of the experimental data for $x = 0.32$ whereas T^* of the simulation seems to be slightly larger for $x = 0.34$. It is also to be noticed that the slope at the onset of ferromagnetism is larger for the simulations which is due to the simplifying assumptions of the Ising-model. A minimum number of FM impurities in the epitaxial samples is always present, either induced by growth defects or by impurities due to unavoidable small fluctuations of the deposition rate. This can be deduced from the fact that a significant FM contribution is only seen above $p \approx 0.285$ in the simulation data, whereas for the samples prepared at the stoichiometric composition already strong FM contributions are found.

The influence of the magnetic field on the transition behavior of the simulation was determined exemplarily for a reduced field $H_\mathrm{ext} = 9\,\mathrm{kOe}$. In these simulations T_N is only slightly elevated for p-values equal to the $H_\mathrm{ext} = 100\,\mathrm{kOe}$ data and for $n_\mathrm{min} = n_\mathrm{equi}(T)$, as can be seen on the left of Fig. 7.13. However, no FM contributions are found for $0.26 \leq p \leq 0.30$ and the field-induced magnetization is significantly reduced with respect to the $H_\mathrm{ext} = 100\,\mathrm{kOe}$ data. Single-run simulations for $H_\mathrm{ext} = 9\,\mathrm{kOe}$ and $n_\mathrm{min} = 500$ reveal that the transition range is shifted to larger p-values. For example, for $p = 0.32$ the low temperature magnetization is $M_\mathrm{LT} = 0.33$ whereas for $H_\mathrm{ext} = 100\,\mathrm{kOe}$ and $p = 0.30$ exclusively $M_\mathrm{LT} = 1.0$ was found. It can thus be stated that the increase of the aligning field shifts the percolation threshold for the onset of long-range ordered FM-regions to

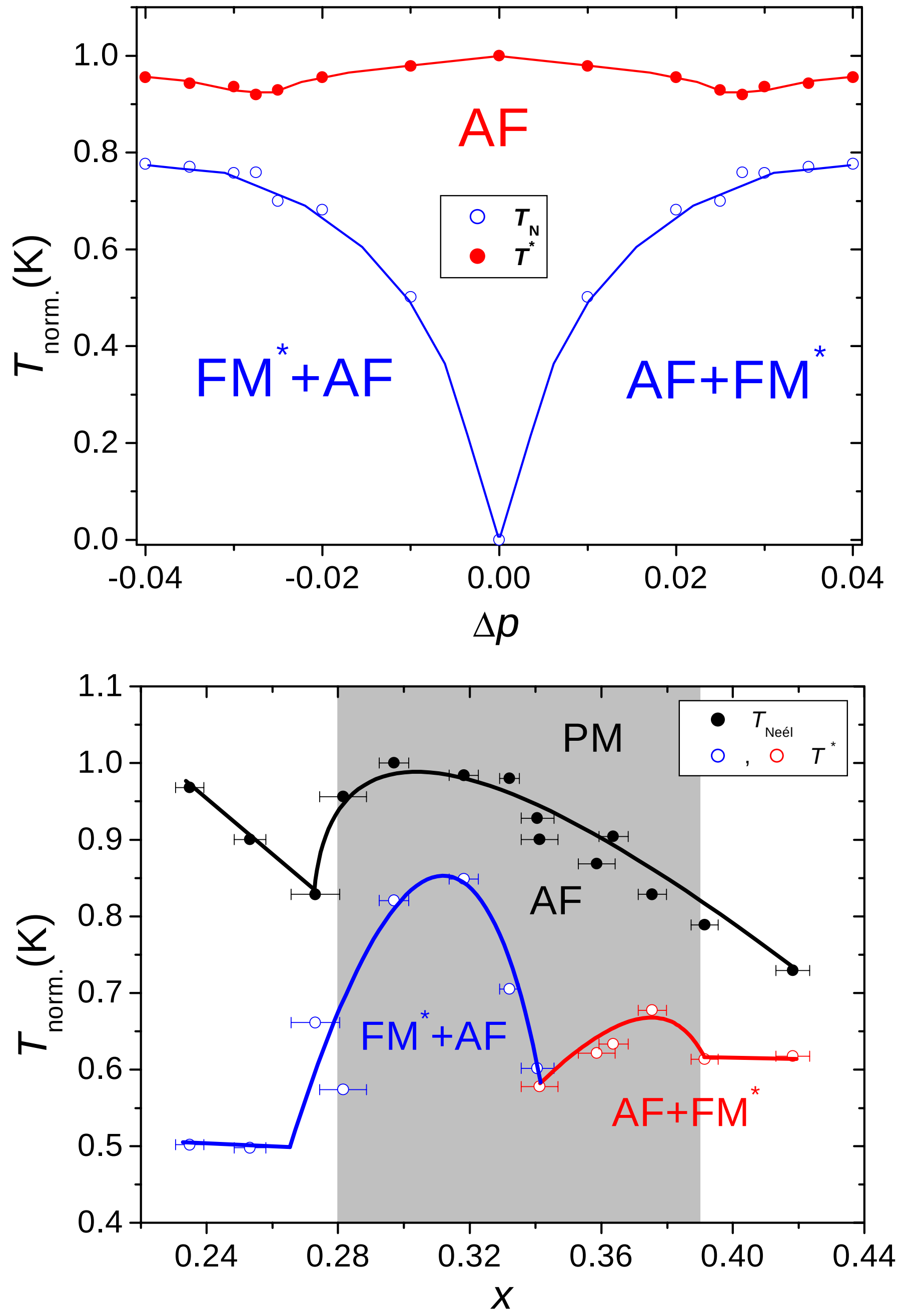

Figure 7.11: Top: Simulated phase diagram with the characteristic temperatures determined from the data at the bottom of Fig. 7.9. To facilitate a comparison with the experimental data (bottom) the characteristic temperatures were drawn symmetrically to either side of the diagram for the simulation data. The temperature T was normalized to the respective maximum of T_{N} at $p = 0.26$. The phase identities for the simulation data were chosen in correspondence to the naming chosen in the analysis of the experimental data.

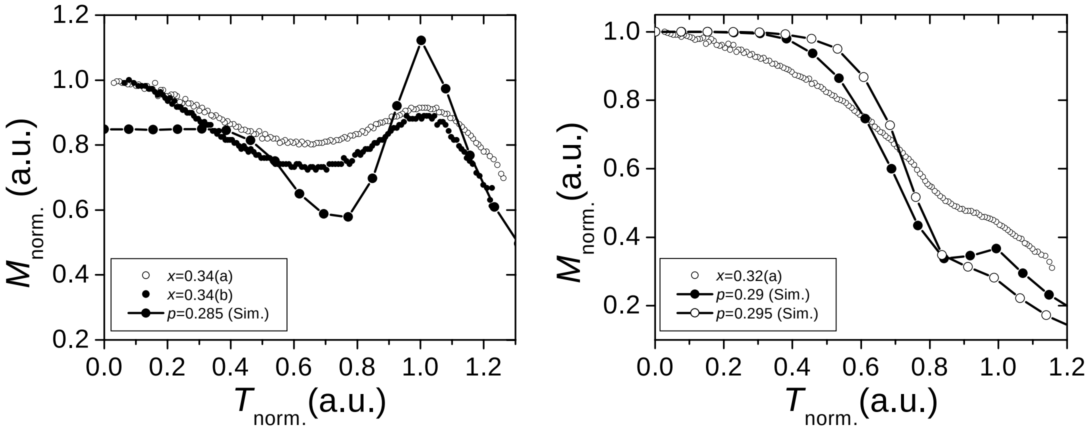

Figure 7.12: Comparison of $M_{\mathrm{exp}}(T)$ and $M_{\mathrm{sim}}(T)$. Left: $M(T)$ taken from two different samples with $x = 0.34$ compared against the $p = 0.285$ curve of Fig. 7.9. Right: $M(T)$ taken from a sample with $x = 0.32$ compared against $p = 0.29$ and $p = 0.295$. The curves were rescaled to facilitate comparison.

smaller p-values but does not significantly alter the characteristic temperatures. Consequently, at least the relations of the standard coupling constants chosen for the simulations appear to be valid. Furthermore, the aligning field $\mu_0 H = 10\,\mathrm{T}$ is still small as compared to the metamagnetic phase transition field observed for $p = 0$ (see Fig. 7.17) and is thus not assumed to strongly affect the simulated phase diagram.

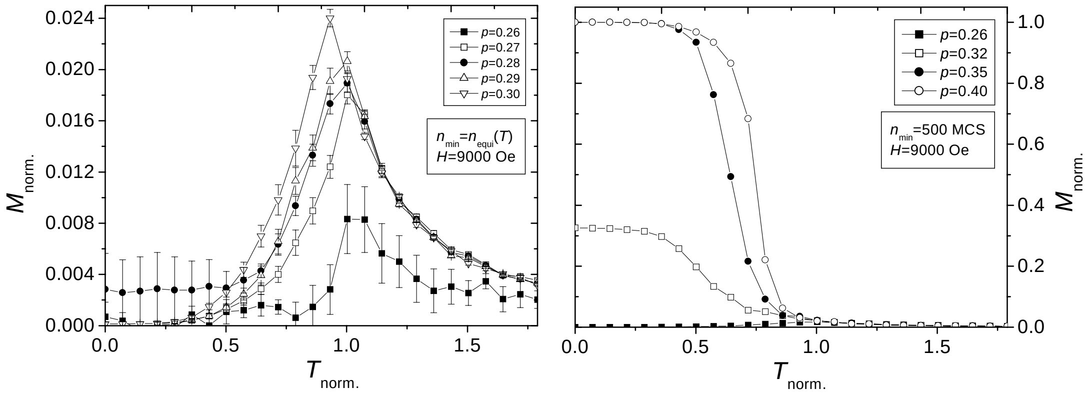

Figure 7.13: Simulated $M(T)$ data with $H_{\mathrm{ext}} = 9\,\mathrm{kOe}$. The occupation ranges from $p = 0.26$ to $p = 0.30$ for $n_{\mathrm{min}} = n_{\mathrm{equi}}(T)$ (left) and from $p = 0.26$ to $p = 0.40$ for $n_{\mathrm{min}} = 500$ (right). The temperature was normalized to $T = 278\,\mathrm{K}$ (see Fig. 7.9).

Microscopic spin configuration

A further investigation was performed by the analysis of the microscopic spin structure of the lattice for $H_{\text{ext}} = 100\,\text{kOe}$ at constant temperature. Some spin configurations (see also Fig. 7.1) for $p = 0.27$ and $p = 0.29$ at $T = 0.1\,\text{K}$ are presented in Fig. 7.14.

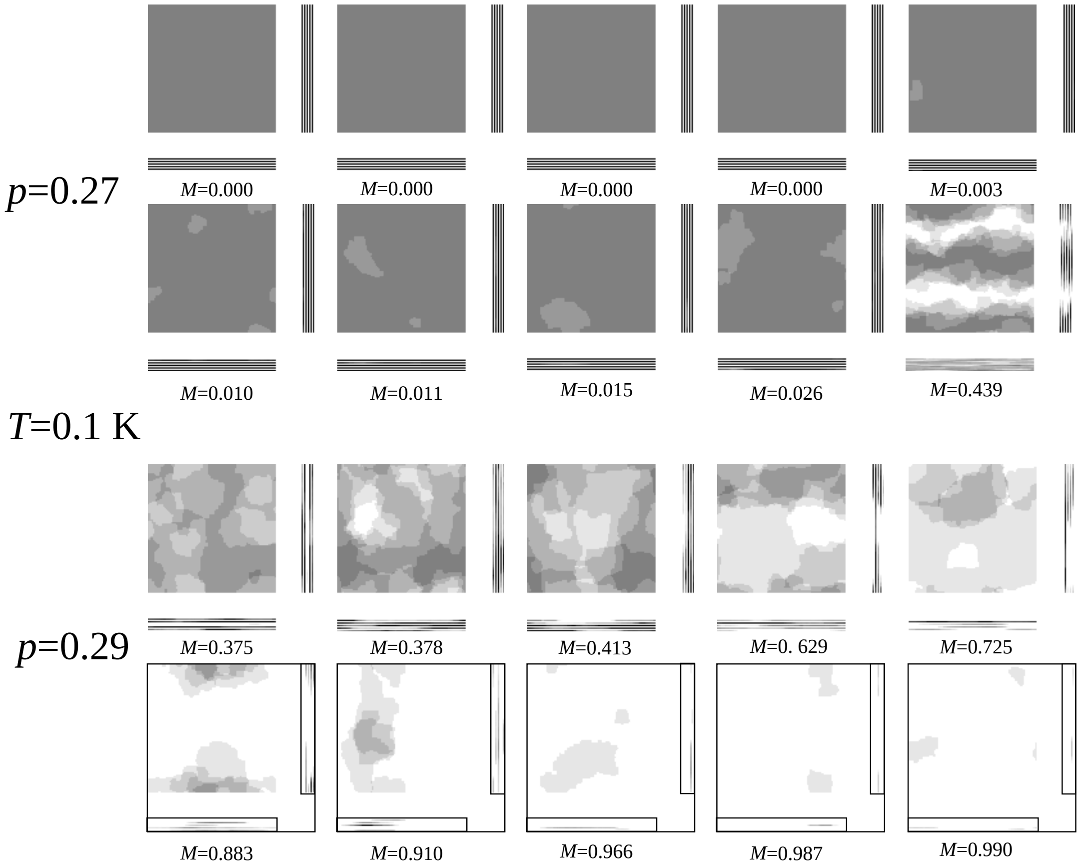

Figure 7.14: Spin structure of the 3D lattice for $p = 0.27$ (top) and $p = 0.29$ (bottom) at $T = 0.1\,\text{K}$. $\{c_i\}$ is different for each image. The net magnetization values are given below the images. For interpretation of the 3D images see caption of Fig. 7.1.

It is found that for both p values FM domains are formed and that their extension increases with the net magnetization. However, the alternating magnetic layer structure of the AF is conserved on a large scale due to the strong in-plane coupling. Consequently, the observed FM or AF domains mainly extend within the x-y-plane. For large M only small AF domains remain stable. In contradistinction to the narrow distribution of M values for $p = 0.27$, for $p = 0.29$ a wide spread of M values occurs, as was already quantified by the error bars in Fig. 7.9. The ribbon-like domain-shape, as found for the largest M-value at $p = 0.27$, or circular ribbons (Fig. 7.15, $p = 0.28$ and $M = 0.492$) are only stable for small p and occur for the relaxed simulations very rarely since the AF state is preferred for $p < 0.27$. However, for the non-relaxed simulations these structures typically occur for $p < 0.27$. As already mentioned above, the transition range is shifted to smaller p for the non-relaxed simulations.

The transition from predominantly AF to predominantly FM behavior was also analyzed by the microscopic spin structure, as shown in Fig. 7.15 for $T = 0.1\,\mathrm{K}$. Since the $M(T)$-curves are distributed about the averaged curve, the closest curves enveloping the averaged curve were chosen to obtain an impression of the spin structure for distinct p values. The average net magnetization increases with p, generated by the increasing proportions of the FM domains, as described above. The side view additionally discloses the AF contributions present in the images with smaller p, indicated by the alternating dark/light structures.

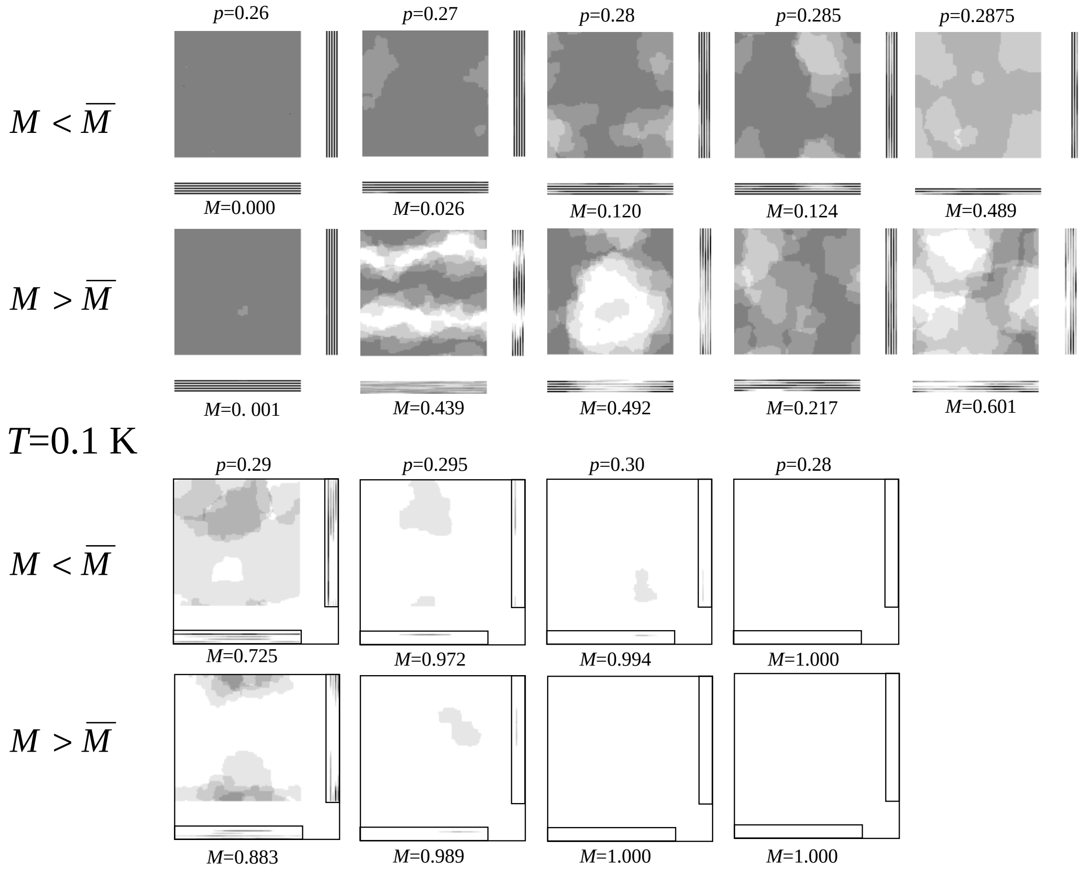

Figure 7.15: Spin structure for $p = 0.26, \ldots, 0.31$. The images were taken at $T = 0.1\,\mathrm{K}$ from the curves just above and below the average curve $\overline{M}(T = 0.1\,\mathrm{K})$ (see Fig. 7.9). The respective normalized magnetization value is denoted below each image.

The temperature dependence of the spin structure was analyzed to obtain further information on the formation of the domains. In Fig. 7.16 the $M(T)$-curve of a sample simulation for $p = 0.2875$ is shown, including the images of the spin structure at various temperatures. Starting at high temperature in the paramagnetic region the spin structure is completely disordered with a very low induced magnetization. Despite an increase of the induced magnetization, no significant order is seen in the top view on approaching $T_\mathrm{N} \simeq 257\,\mathrm{K}$. Nevertheless, the side-views already reveal the onset of a lateral spin-order with alternating planes. At the local minimum (T^*) the AF structures appear very distinct in the side-views. In the top-view large regions with increased brightness indicate distortions due to FM impurities. A further decrease of the temperature causes these regions to stabilize. The easy alignment of the FM ordering regions by the magnetic field results in a further increase of the brightness. From the side-views it can be seen that these domains are virtually two-dimensional. At the lowest temperature $T = 0.1\,\mathrm{K}$ the whole lattice is separated into FM and AF domains. It is noteworthy that the FM domains stay fixed at the position where they were initially formed. Finally, the domain structure for a given configuration $\{c_i\}$ and thus the low temperature magnetization varies from simulation to simulation, caused by the multiple minima energy landscape.

7.4.2 Results for $M(H)$

In section 6.2 the magnetic isotherms of the epitaxial thin films were discussed. The maximum magnetic field $\mu_0 H_\mathrm{ext} = 1\,\mathrm{T}$ applied is significantly smaller than the metamagnetic phase transition field of the AF regions in the samples. However, the additional random variable $\{c_i\}$ and the multiple minima problem significantly complicates the simulation of low-field hysteresis loops. In the following, simulated hysteresis loops and initial loops are presented to give an at least qualitative impression of the field dependence. Each loop was simulated for a particular configuration $\{c_i\}$. However, it was found that the shape does not significantly depend on $\{c_i\}$ for constant p. The simulations were performed for standard coupling constants. The initial loops start at zero field, increasing towards the maximum positive field $\mu_0 H_\mathrm{ext} = 1000\,\mathrm{T}$. Subsequently, the field was reduced to the maximum negative field and increased back to the maximum positive field. The simulations were performed with $n_\mathrm{min} = 500$ which did not allow for a full relaxation of the system in the case of the $M(T)$ simulations. However, it can be assumed that larger external fields significantly reduce the relaxation time. Since the position of the coercive field is of major importance for the choice of a higher density of data points, the principal behavior of H_C with n_min was checked in advance. It was found that H_C does not significantly change if $n_\mathrm{min} \gg 500$.

The results for the standard coupling constants of the present model and

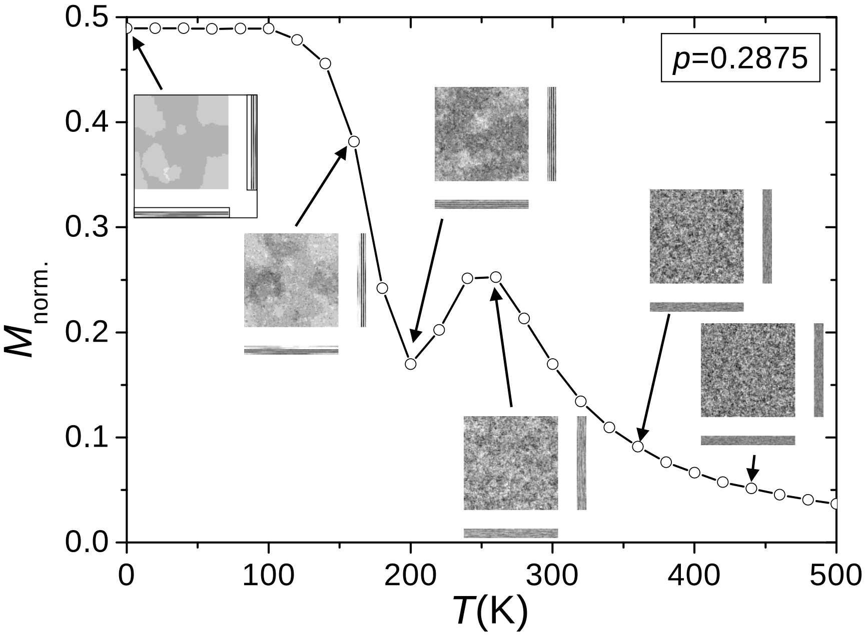

Figure 7.16: $M(T)$ and spin structure for $p = 0.2875$. The images were taken at different temperatures as indicated by the arrows. FM domains are formed at the onset of ferromagnetism and maintained to low temperatures. The shape of the $M(T)$ curves strongly varies for different simulations with identical configurations $\{c_i\}$.

p =0.0, 0.20, 0.25 and 0.29 are shown in Fig. 7.17. All hysteresis loops exhibit a FM-type shape at $T = 0.1\,\mathrm{K}$. For $T = 80\,\mathrm{K}$ and $p = 0.0$ steps are noticed in the coercive field range corresponding to coherent single layer spin flips. These flips are thus randomly thermally induced.

The coercive field H_C was determined from the data of Fig. 7.17 and is depicted as a function of p in Fig. 7.18. The overall behavior is identical for $T = 0.1\,\mathrm{K}$ and $T = 80\,\mathrm{K}$. H_C monotonously decreases with increasing p.

Comparing these results with the experimental data it can be stated that in the simulations only coherent domain rotations may occur since the dipolar interaction is not included in the model. The large rotation energy of this coherent rotation is the cause for the large coercive fields observed in the simulations. In contradistinction, the experimental hysteresis loops exhibit comparatively small coercive fields. Since the easy axis of the films was found to be canted with respect to the c-axis a domain rotation does most probably occur due to domain wall motion. The energy of this motion is much smaller than for coherent domain rotation resulting in a much smaller coercive field.

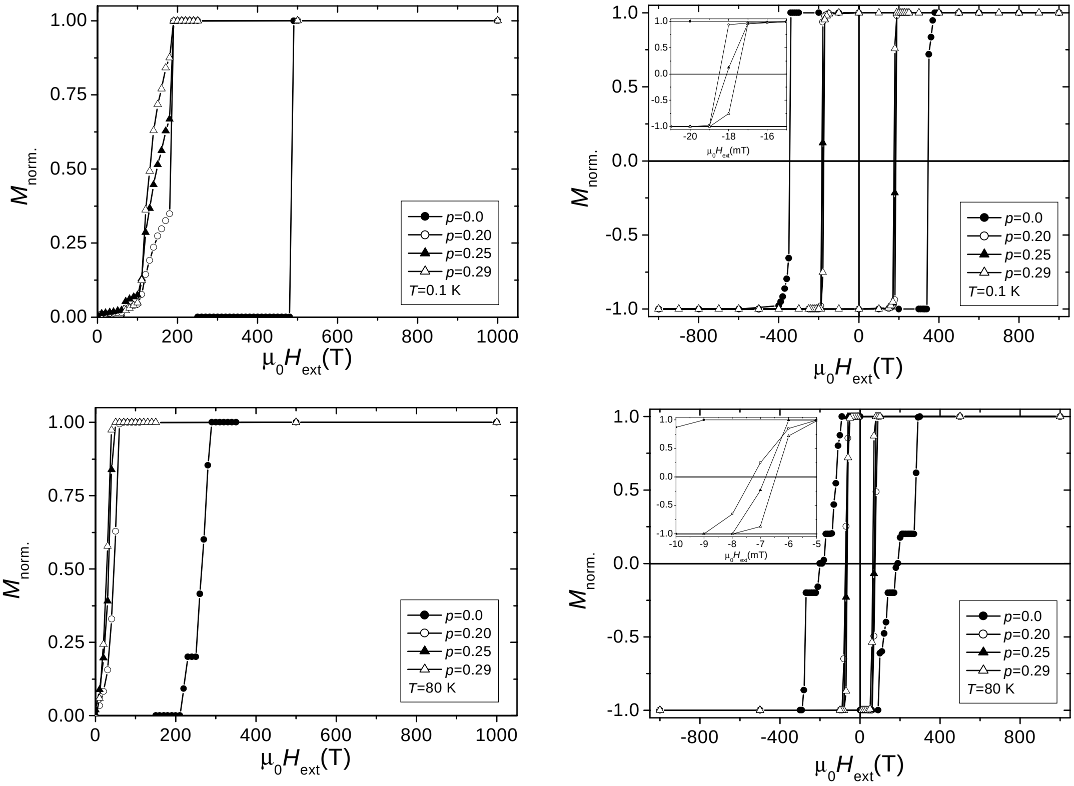

Figure 7.17: $M(H)$ for standard coupling constants and p =0.0, 0.20, 0.25 and 0.29. Left: Initial magnetization curves for $T = 0.1\,\text{K}$ (top) and $T = 80\,\text{K}$ (bottom). The insets show a magnification of the coercive region.

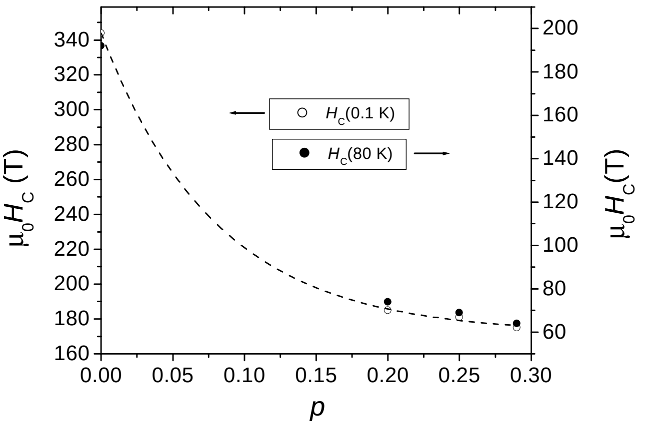

Figure 7.18: H_C for p =0.0, 0.20, 0.25 and 0.29 as determined from the data of Fig. 7.17. Open symbols for $T = 0.1\,\text{K}$ and solid symbols for $T = 80\,\text{K}$. The dashed line to guide the eye.

7.5 Problems and open questions

From the comparison of the non-relaxed and the relaxed data, as shown in Fig. 7.9, it can be concluded that the position and the width of the transition range from predominantly AF to predominantly FM significantly depends on the relaxation behavior of the model. According to the extended range of B-type impurity concentration over which the transition occurs a composition-dependent second order phase transition can be assumed. However, if the relaxation time of the spin lattice is even longer than estimated by the auto-correlation function, a further shrinkage of the transition range may occur. This might eventually lead to a first order phase transition. Long-time simulations may yield the type of transition, but are beyond the scope of this work. Nevertheless, there is no direct impact on the interpretation of the simulations: If the transition is of first order and the model is applied to the experimental data, the small unavoidable fluctuations of the deposition rate ($\geq 1\,\%$) and thus the locally varying composition of the films results in a weighted averaging over the transition range. Then the resulting $M(T)$-curves exhibit second order phase transition properties, as observed for the present samples. Finally, it has to be mentioned that the large number of different coupling constants of the model were reduced by heuristic methods. Other combinations yielding similar results may exist. Yet, the good agreement with the experimental data and the intuitive explanations of the present choice of coupling constants suggest correctness.

7.6 Conclusions

In this chapter an Ising-like Hamiltonian with quenched randomness of FM impurities was proposed as a starting point of a description of the experimental magnetization data. This Hamiltonian was applied in temperature and magnetic field-dependent importance sampling Monte Carlo simulations performed with a GUI-based simulation program on a standard Personal Computer. Following heuristic methods, the large parameter space was reduced and reasonable coupling constants for either kind of lattice sites could be determined. The shape of the temperature-dependent magnetization data obtained from epitaxial Ti$_x$Fe$_{1-x}$ thin films and the magnetic phase diagram of these films were reproduced within the limits of the underlying model. Due to these limit growth-related aspects of the experimental magnetic phase diagram are not found in the phase-diagram obtained for the MC simulations. An analysis of the detailed spin configuration generated by the simulations revealed that the magnetism can be described as an incoherent superposition of AF and FM contributions due to mainly in the x-y-plane extended AF and FM domain structures which remain stable on cooling below T_N. The results suggest that the magnetic behavior of the thin films can be attributed to a quenched disorder in the C14 lattice which is induced during the film growth. The assumptions of FM coupling impurity sites in the model and the qualitative agreement with the experimental data underline that an off-stoichiometric composition of the C14 unit cell with FM coupling determines the shape of the magnetic phase diagram. Finally, with the standard coupling constants derived only FM-type hysteresis loops could be generated. The large coercive field observed in the simulations can be attributed to coherent domain wall rotation. In the thin films the additional dipolar interaction combined with a canted easy magnetization axis leads to a magnetization reversal process predominantly determined by domain wall motion.

Conclusion and perspectives

In the present work thin films of Ti_xFe_{1-x} in the C14 Laves phase stability range were studied. Employing the MBE thin film preparation method polycrystalline (110)-oriented and highly epitaxial (001)-oriented thin films were prepared; to the author's best knowledge for the first time. The magnetic properties of a series of samples were characterized by SQUID magnetometry. The polycrystalline sample exhibited a pronounced exchange bias effect due to the interface coupling of magnetically differently ordered regions. In contradistinction, this effect was not found for the epitaxial samples. All epitaxial thin films revealed a coexistence behavior of ferromagnetic (FM) and antiferromagnetic (AF) C14 regions in composition-dependent proportions. A magnetic phase diagram was derived from the temperature dependent susceptibility data. It exhibits AF and FM regions in coexistence at low temperature. Finally, this observed compositional dependence was modelled by a random quenched disorder Hamiltonian based on the 3D Ising model. The quenched disorder was introduced by FM coupling impurity sites in an overall AF matrix thus reflecting magnetic impurities due to structural and compositional inhomogeneities in the samples. The temperature-dependent magnetization and the derived simulated phase diagram were found to be in good agreement with the experimental data.

The present work has shown that it is indeed possible to overcome the preparational difficulties of $TiFe_2$ bulk samples by the alternative approach of epitaxial thin film preparation. This approach even enhances the range of homogeneity of the C14 phase. Based on the magnetic phase diagram derived here for phase-pure C14 samples, the magnetic phase diagram for bulk samples, as suggested by [11], appears to be significantly influenced by impurity phase segregation. The thin film phase diagram established in the present work, corrected for thin-film specific signatures, can be assumed to be applicable to phase-pure C14 bulk samples as well. Nevertheless, it might be impossible to prepare such bulk samples at all.

Based on the magnetic properties of the thin films and the results of the Monte Carlo simulations the magnetism of the $TiFe_2$ system is mainly driven by magnetic phase separation which is induced by inhomogeneities in structure structure and/or composition. The energetically near-degenerate AF and FM ground state of $TiFe_2$ make this system highly susceptible to such a phase separation scenario.

Even if it is possible to prepare structurally phase-pure samples, as shown here, it remains questionable whether magnetically phase-pure material can be obtained. Naturally, these conclusions may be valid not only for $TiFe_2$ but also for other magnetics compounds exhibiting a magnetic instability due to a near-degeneracy of magnetic states.

Despite these immanent difficulties several interesting aspects deserve future investigation. To begin with, as a consequence of the successful epitaxial thin film preparation, structurally homogeneous superlattices with alternating magnetic long-range order of subsequent layers may be prepared by varying the composition of these layers. The magnetic state of subsequent layers will then not "switch" from a pure AF magnetic state to a pure FM magnetic state but from predominantly AF to predominantly FM. Furthermore, considering the occurrence of a unidirectional anisotropy in polycrystalline samples, such layered structures may also exhibit a pronounced exchange bias effect without the additional complications of interface strain and interdiffusion, commonly unavoidable in AF/FM interface studies. Also, layers with a composition gradient about the stoichiometric point will exhibit a continuous transition from AF to FM. Further experiments may be performed on such samples. Spin polarized tunnelling experiments, as a local probe of magnetism, may yield additional insight into the true nature of the magnetic behavior of the samples. The observed agreement of the experimental data and the proposed model of quenched disorder does not rule out that the magnetic "granularity" is in fact a dynamic phenomenon [96–100]. Since spin-polarized STM measurements can only image (quasi-)static magnetic structures, the degree of static magnetic separation in $TiFe_2$ could be judged by this technique. Alternatively, fast probes, such as spin-polarized magnetic neutron scattering, could give insights into the degree of dynamic phase separation. All this has to remain for future resolution.

Appendix

User's guide to the Monte Carlo simulation program 'FE2TI'

The Monte Carlo simulation program was written in the C++ programming language employing the Microsoft Visual C++ 5.0 environment and the Microsoft Foundation Class (MFC) libraries. The executable file 'Fe2Ti.exe' was compiled for the x86 processor family. Its functionality was tested on the Microsoft Windows 9x and Windows NT 4.0 operating system. The program is controlled by either script-files, which describe in a keyword-based language the batch-job to be performed, or by its graphical user interface. On program startup the script-file 'default.ini' is executed which contains the standard settings for the program and may be modified by a simple text-editor. A screenshot with an expansion of the menu structure is shown in Fig. 7.6.

Following is a description of the available menu commands:

Datei File-related commands. The only implemented command is 'Save Image'.

- **Save Image** Save the current image in the viewing window to media. A file-requester is used to enter the file-name.

Bearbeiten No commands implemented.

Ansicht Enable or disable toolbar and status line.

Generator Commands for reliability tests of the random number generators.

- **Check Gen C** Generates random numbers with the C++ libraries generator between 0 and 255 and displays a 2D-array as a grey-scale image. Subsequently generated arrays are averaged with the previous and the resulting average image is displayed. If the generator produces random numbers the image should evolve into a homogenously grey area. The default number of iterations is 100. The average value of the numbers is denoted next to the image and should converge to 127.5.

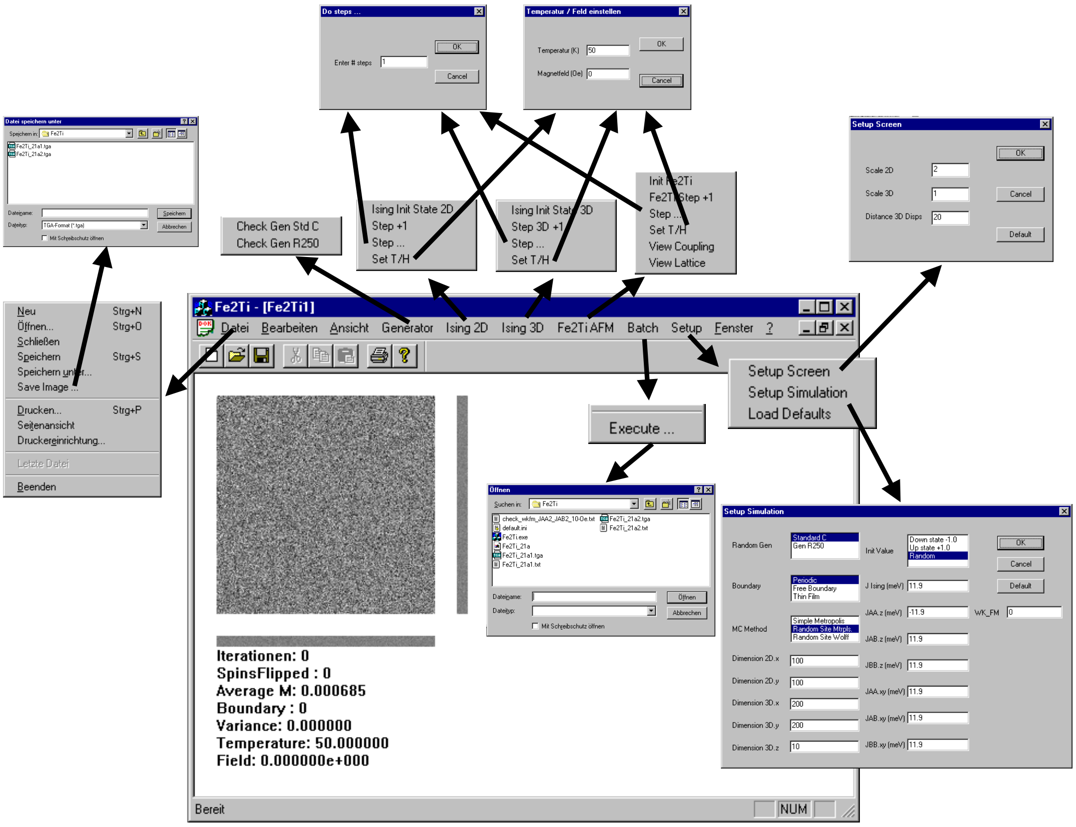

Enter # steps: 1

Temperatur (K): 50
Magnetfeld (Oe): 0

Speichern in: Fe2Ti
Fe2Ti_21a1.tga
Fe2Ti_21a2.tga
Dateiname:
Dateityp: TGA-Format (*.tga)

Scale 2D: 2
Scale 3D: 1
Distance 3D Disps: 20

Suchen in: Fe2Ti
check_wkfm_JAA2_JAB2_10-0e.txt
default.ini
Fe2Ti.exe
Fe2Ti_21a
Fe2Ti_21a1.tga
Fe2Ti_21a1.txt
Fe2Ti_21a2.tga
Fe2Ti_21a2.txt
Dateiname:
Dateityp:

```
Iterationen: 0
SpinsFlipped : 0
Average M: 0.000685
Boundary : 0
Variance: 0.000000
Temperature: 50.000000
Field: 0.000000e+000
```

Random Gen: Standard C / Gen R250 (selected: Standard C)
Init Value: Down state -1.0 / Up state +1.0 / Random (selected: Random)
Boundary: Periodic / Free Boundary / Thin Film (selected: Periodic)
MC Method: Simple Metropolis / Random Site Mtrpls. / Random Site Wolff (selected: Random Site Mtrpls.)
J Ising (meV): 11.9
JAA.z (meV): -11.9
WK_FM: 0
JAB.z (meV): 11.9
JBB.z (meV): 11.9
JAA.xy (meV): 11.9
JAB.xy (meV): 11.9
JBB.xy (meV): 11.9
Dimension 2D.x: 100
Dimension 2D.y: 100
Dimension 3D.x: 200
Dimension 3D.y: 200
Dimension 3D.z: 10

Fig. A.1: Screenshot of the simulation program. The available submenu windows are indicated by the arrows.

- **Check Gen R250** Generates random numbers with the R250/R521 generator [93]. See 'Check Gen C'.

Ising 2D Commands for the 2D Ising model.

- **Ising Init State 2D** Initializes the lattice with values according to the setup parameter 'Setup → Setup Simulation → Init value'.
- **Step +1** Performs a single Monte Carlo step on the Ising 2D lattice employing boundary conditions as defined in 'Setup → Setup Simulation → Boundary'. Various current variables are displayed next to the image:
  - **Iterationen** Current number of MCS performed with the current parameters.
  - **SpinsFlipped** Number of spins flipped during the last MCS.
  - **Average M** Normalized magnetization of the current lattice state.
  - **Boundary** Number of boundary sites visited during the last MCS. This should be a value close to the actual number of boundary sites.

  - **Variance** Error of the mean value of a number of previous M-values defined by the internal parameter 'NumLastMs' (see below).
  - **Temperature** Current temperature in K.
  - **Field** Current applied magnetic field in Oe.
  - **AvAvM2D** Mean value of a number of previous M-values defined by the internal parameter 'NumLastMs' (see below).
  - **Energy** Energy of the lattice in meV.
- **Step** Requests the number of MCS to be performed (see above).
- **Set T/H** Enter temperature in K and magnetic field in Oe.

Ising 3D Commands for the 3D Ising model (see Ising 2D).

Fe2TiAFM Commands for the $TiFe_2$ quenched disorder model.

- **View coupling** Switch to a display mode in which the impurity sites are displayed dark.
- **View lattice** Switch to a display mode in which the up-spins are displayed dark.

For the remaining commands see 'Ising 2D'.

Batch Commands for performing batch tasks.

- **Execute** Request the file-name of the batch job to be performed. The job is started immediately after selecting 'OK'.

Setup Command for the program setup.

- **Setup Screen** Setting of display relevant parameters:
  - **Scale 2D** The number of pixels displayed for each lattice site in the 2D displays is scaled in x- and y- direction with this value. Only positive integers are allowed.
  - **Scale 3D** See 'Scale 2D'.
  - **Distance 3D Disps** Sets the number of pixels between the z-view and the the x- and y-views.
- **Setup Simulation** Setting of simulation relevant parameters:
  - **Random Gen** Select the random number generator to be used: 'R250/R521' [93] generator is a Tausworthe algorithm [101]. 'Standard C' generates random numbers with the C++ libraries generator.
  - **Boundary** Sets the boundary conditions:

        - **Periodic** The next neighbor of a boundary site to a specific direction is placed on the opposite side.
        - **Free Boundary** Beyond the lattice boundaries no next neighbors.
        - **Thin film** Periodic boundary conditions in the x-y-plane and free boundary conditions in z-direction (only valid for 3D models).
    - **MC Method** Sets the Monte Carlo method:
        - **Simple Metropolis** The lattice sites checked are not selected randomly but sequentially starting from the beginning of the first row to the end of the last row and the Metropolis algorithm is applied.
        - **Random Site Metropolis** The lattice sites checked are selected randomly and the Metropolis algorithm [87] is applied.
        - **Random Site Wolff** The lattice sites checked are selected randomly and the Wolff algorithm [92] is applied.
    - **Dimension** Sets the lattice dimensions for 2D- and 3D-models.
    - **Init value** Sets the initialization value for the lattice to either spin up, spin down, random or antiferromagnetic (AF).
    - **J Ising** Sets the coupling constants in meV for the 2D- and 3D-Ising model.
    - **J XX.xx** Sets the coupling constants in meV for the $TiFe_2$-model.
    - **WK_FM** Sets the p-value for the $TiFe_2$-model.
- **Load Defaults** Execute 'default.ini' and, thus, set the default values.

Fenster Arrange the client windows in the main window.

? Display copyright information.

With the menu command 'Batch → Execute' a sequence of commands may be performed. This is necessary for long-time calculations which require the variation of parameters. A brief description of the available commands are given below:

OUTPUT Filename Set output-filename (default: "default_out").

STOREIMAGE SPIN|COUPLING Immediately store an image of the current displayed state (either spin or coupling) in file with name *current output-filename+number+SPIN—COUPL*.

OUTPUTPARMS PAR_Temp|PAR_M|PAR_H|PAR_Iter Sequence of output parameters (default: PAR_Temp PAR_M PAR_H PAR_Iter).

OUTPUTDETAIL Filename Set output-filename for logging (default: ”default_log”).

SET DETAILLOG ON|OFF Set logging on/off (default: off).

SELECTMODEL I2D|I3D|FE2TI Selection of simulation model to be used (must be specified).

SELECTDIM2D ⟨dimx⟩⟨dimy⟩ Set dimensions of 2D model (default: 100 100).

SELECTDIM3D ⟨dimx⟩⟨dimy⟩⟨dimz⟩ Set dimensions of 3D model (default: 100 100 10).

SELECTGEN GEN_R250|GEN_STANDARD_C Set pseudo-random number generator (default: GEN_R250).

SET NUMLASTMS ⟨word_number⟩ Set number of magnetization values for average and error calculation (default: 10).

SET ACCURACY ⟨real_number⟩ Set threshold of the relative error $\sigma/\overline{M}$ for calculation stop (default: 1E-3). If $\sigma/\overline{M} <$*real_number* then stop iterating.

SET WK_FM ⟨$\mathbf{0.0 \leq}$ real_number $\mathbf{\leq 1.0}$⟩ Set probability for FM coupling site in $TiFe_2$-model (default: 0.0).

SET TEMPERATURE ⟨pos.real_number⟩ Set temperature in K.

SET FIELD ⟨real_number⟩ Set magnetic field in Oe.

SET DISPLAYFRAME ⟨pos.word_number⟩ Display only n-th frame while iterating (default: 1).

SET INIT ZERO|ONE|RANDOM|AF Set initial occupation of sites in each MC-step and reconfigure lattice (default: RANDOM).

SET MAXITER ⟨ulong⟩ Set max. iterations in each step (default: 100).

LOOP LTEMPERATURE|LFIELD|LWK_FM STEP ⟨from⟩⟨to⟩⟨step⟩ Do for-loop with variation and step-size.

SET REINIT TRUE|FALSE Reinit lattice after each loop step (default: FALSE).

SET JAAz|JABz|JBBz|JAAxy|JABxy|JBBxy|JEx ⟨real_number⟩ Set coupling constants in meV.

SET BOUNDC PERIODIC|FREE Set boundary conditions.

SET MCMETHOD SIMPLEM|RANDOMM|RANDOMWOLFF Set Monte Carlo method to simple or randomsite Metropolis or Wolff.

END Declares end of script (must be entered !).

It has to be noted that no blank lines are allowed until the 'END'-command is set. As an introduction a sample script-file is printed below. The comment after the command lines must not be entered into the script-file.

OUTPUTPARMS PAR_TEMP PAR_M PAR_H PAR_ITER PAR_ERROR PAR_WKFM
(Causes the sequence of output data to be: temperature, magnetization, field, number of iterations performed, the error of the mean value and p.)
SELECTMODEL FE2TI
(Selects the quenched disorder $TiFe_2$-model for the simulation.)
SELECTDIM3D 100 100 10
(Set the 3D dimensions.)
SET JAAz -2.0
SET JABz 2.0
SET JBBz 2.0
SET JAAxy 11.9
SET JABxy 5.0
SET JBBxy 5.0
(Set the $TiFe_2$ coupling constants.)
SET NUMLASTMS 1000
(Set the number of iterations to be averaged to 1000 MCS.)
SET MAXITER 1500
(Set the maximum number of iterations per data point to 1500.)
SET ACCURACY 1E-3
(Set the stopping condition $\sigma/\overline{M}$ to 0.1%.)
SET FIELD 9000.0
(Set external field to 9000 Oe.)
SET DISPLAYFRAME 20
(Show only 20th image while iterating.)
SET REINIT FALSE
(Do not reinit the lattice after the iteration cycle.)
SET BOUNDC PERIODIC
(Set periodic boundary conditions.)
SET MCMETHOD RANDOMM
(Select the random Metropolis algorithm.)

SET STOREFRAME 1
(Store each image in a .tga-file while appending an incrementing number to the file-name.)
SET DETAILLOG OFF
(Do not store detailed information of each iteration.)
SET WK_FM 0.35
(Set $p = 0.35$.)
SET INIT RANDOM
(Initialize the lattice with a random spin configuration.)
OUTPUT Out_035
(Set start of output file-name to 'Out_035'.)
LOOP LTEMPERATURE 500.1 0.1 STEP -20.0
(This starts the iterating: The temperature is cycled from 500.1 K down to 0.1 K with a step-size of 20 K. The average M-values of the last 1000 iterations are stored in the output file for each temperature.)
STOREIMAGE COUPLING
(Save the coupling information into a .tga-file.)
END
(This is mandatory. After this command comments may be inserted.)

Bibliography

[1] F. Laves and H. Witte, Metallwirtschaft **14**, 645 (1935).

[2] S. Asano and S. Ishida, J. Magn. Magn. Mater. **70**, 39 (1987).

[3] S. Asano and S. Ishida, J. Phys. F: Met. Phys. **18**, 501 (1988).

[4] S. Asano and S. Ishida, J. Phys. Condens. Matter **1**, 8501 (1989).

[5] E. Hoffmann, P. Entel, E. Wassermann, K. Schwarz, and P. Mohn, J. Phys. **IV**, Colloq. C2-117 (1995).

[6] R. P. Elliot, OSR Technical Note OSR-TN-247 (1954).

[7] E. Piegger and R. S. Craig, J. Chem. Phys. **39**, 137 (1963).

[8] T. Nakamichi, J. Phys. Soc. Jpn. **25**, 1189 (1968).

[9] C. W. Kocher and P. J. Brown, J. Appl. Phys. **33** (Suppl.), 1091 (1962).

[10] W. E. Wallace, J. Chem. Phys. **41**, 3857 (1964).

[11] E. F. Wassermann, B. Rellinghaus, T. Roessel, and W. Pepperhoff, J. Magn. Magn. Mater. **190**, 289 (1998).

[12] P.Villars and L. D. C. (Ed.), *Pearson's Handbook of Crystallographic Data for Intermetallic Phases, Second Edition* (ASM International, Materials Park, Ohio 44073, USA, 1996).

[13] Y. Muraoka, M. Shiga, and Y. Nakamura, J. Phys. Soc. Jpn. **40**, 905 (1976).

[14] Y. Nishihara and Y. Yamaguchi, J. Phys. Soc. Jpn. **54**, 1122 (1985).

[15] Y. Nishihara and Y. Yamaguchi, J. Phys. Soc. Jpn. **55**, 920 (1986).

[16] Y. Nishihara, J. Magn. Magn. Mater. **70**, 75 (1987).

[17] Y. Nishihara and Y. Yamaguchi, J. Phys. Soc. Jpn. **52**, 3630 (1983).

[18] S. Ishida, S. Asano, and J. Ishida, J. Phys. Soc. Jpn. **54**, 4695 (1985).

[19] S. Ishida and S. Asano, J. Phys. Soc. Jpn. **54**, 4688 (1985).

[20] S. Ishida, S. Asano, and J. Ishida, J. Phys. Soc. Jpn. **54**, 3925 (1985).

[21] W. Brückner, K. Kleinstück, and G. E. R. Schulze, Phys. Stat. Sol. **23**, 475 (1967).

[22] T. B. Massalski (Ed.), *Binary Alloys Phase Diagrams, Second Edition* (ASM International, Materials Park, Ohio 44073, USA, 1996).

[23] P. Stauche, S. Erdt-Böhm, M. Brinkmann, and H. Bach, J. Cryst. Growth **166**, 390 (1996).

[24] P. J. Brown, J. Deportes, and B. Ouladdiaf, J. Phys. Condens. Matter **4**, 10015 (1992).

[25] G. K. Wertheim, J. H. Wernick, and R. C. Sherwood, Solid State Commun. **7**, 1399 (1969).

[26] J. Pelloth, R. A. Brand, and W. Keune, J. Magn. Magn. Mater. **140-144**, 59 (1995).

[27] E. F. Wassermann, J. Magn. Magn. Mater. **100**, 346 (1991).

[28] P. Entel, E. Hoffmann, P. Mohn, K. Schwarz, and V. L. Moruzzi, Phys. Rev. B **47**, 8706 (1993).

[29] C. E. Guillaume, C. R. Acad. Sci. **125**, 235 (1897).

[30] E. F. Wassermann, in *Ferromagnetic Materials*, edited by K. H. Bushow and E. P. Wohlfarth (North-Holland, Amsterdam,1990), Vol. VI, p. 240.

[31] N. W. Ashcroft and N. D. Mermin, *Solid State Physics* (Saunders College, West Washington Square, Philadelphia PA19105, USA, 1976).

[32] T. Schneider, M. Acet, B. Rellinghaus, E. F. Wassermann, and W. Pepperhoff, Phys. Rev. B **51**, 8917 (1995).

[33] E. F. Wassermann, B. Rellinghaus, T. Roessel, J. Kästner, and W. Pepperhoff, Eur. Phys. J. B **5**, 361 (1998).

[34] P. P. Macri, S. Enzo, N. Cowlam, P. Rose, G. Principi, and R. Gupta, J. Appl. Phys. **79**, 3730 (1996).

[35] S. H. Liou and C. L. Chien, J. Appl. Phys. **55**, 1820 (1984).

[36] C. L. Chien and S. H. Liou, Phys. Rev. B **31**, 8238 (1985).

[37] C. Heske, Master's thesis, Technische Hochschule Darmstadt, 1993.

[38] M. Huth, Ph.D. thesis, Technische Hochschule Darmstadt, 1995.

[39] R. Du, Ph.D. thesis, University of Illinois at Urbana-Champaign, 1900.

[40] W. Kraus and G. Nolze, Powdercell 1.0, Bundesanstalt für Materialforschung und -prüfung, Berlin, http://www.bam.de.

[41] M. V. Nevitt, J. Appl. Phys. **31**, 155 (1960).

[42] K. Ikeda, T. Nakamichi, K. Noto, Y. Muto, and M. Yamamoto, Phys. Stat. Sol. (b) **51**, K39 (1972).

[43] L. G. Parratt, Phys. Rev. **95**, 359 (1954).

[44] GIXA (**G**lancing **i**ncidence **X**-ray **a**nalysis): low-angle diffraction simulation software package (Phillips).

[45] SEMQuant V3.2, Oxford Instruments.

[46] Dr. Jochen Geerk and Dr. Gerhard Linker, Institut für nukleare Festkörperphysik, Karlsruhe.

[47] RUMP 2.0, ©Computer Graphic Service, Ltd., http://www.genplot.com.

[48] T. Steinborn, Ph.D. thesis, Technische Hochschule Darmstadt, 1994.

[49] C. Flynn, J. Phys. F: Met. Phys. **18**, L195 (1988).

[50] M. Huth, "Epitaxial thin films of intermetallic compounds", in *Handbook of Thin Film Materials*, Vol. 1, H. S. Nalwa (ed.), Academic Press, San Diego 2002, p. 587-626.

[51] P. F. Miceli and C. J. Palmstroem, Phys. Rev. B **51**, 5506 (1995).

[52] R. I. Barabash, W. Donner, and H. Dosch, Appl. Phys. Lett. **78**, 443 (2001).

[53] J. Köble and M. Huth, Material Science Forum **373**, 137 (2001).

[54] L. Vegard, Z. Phys. **5**, 17 (1921).

[55] A. Wienss, Master's thesis, Johannes Gutenberg-Universität Mainz, 1996.

[56] Matlab 5.1, ©The MathWorks, Inc., http://www.mathworks.com.

[57] Mathematica 4.0, ©Wolfram Research, Inc., http://www.wolfram.com.

[58] J. D. Jackson, *Klassische Elektrodynamik* (Walter de Gruyter, Berlin, New York, 1983).

[59] Origin 6.0, ©OriginLab Corporation, http://www.originlab.com.

[60] W. H. Meiklejohn and C. P. Bean, Phys. Rev. **102**, 1413 (1956).

[61] W. H. Meiklejohn and C. P. Bean, Phys. Rev. **105**, 904 (1957).

[62] W. H. Meiklejohn, J. Appl. Phys. Suppl. **33**, 1328 (1962).

[63] J. Nogues and I. K. Schuller, J. Magn. Magn. Mater. **102**, 203 (1999).

[64] A. E. Berkowitz and K. Takano, J. Magn. Magn. Mater. **200**, 552 (1999).

[65] B. Dieny, V. S. Speriosu, S. S. Parkin, B. A. Gurney, D. R. Wilhoit, and D. Mauri, Phys. Rev. B **43**, 1297 (1991).

[66] D. Lederman, C. A. Ramos, V. Jaccarino, and J. L. Cardy, Phys. Rev. B **48**, 8365 (1993).

[67] M. Takahashi, A. Yanai, S. Taguchi, and T. Suzuki, Jpn. J. Appl. Phys. **19**, 1093 (1980).

[68] J. Nogues, D. Lederman, T. J. Moran, and I. K. Schuller, Phys. Rev. B **76**, 4624 (1996).

[69] K. Takano, R. H. Kodama, and A. E. Berkowitz, J. Appl. Phys. **83**, 6888 (1998).

[70] W. J. M. de Jonge, P. J. H. Bloemen, and F. J. A. den Broeder, "Experimental Investigations of Magnetic Anisotropy", in *Ultrathin Magnetic Structures*, vol. 1, J.A.C Bland, B. Heinrich (Eds.), Springer-Verlag, Berlin, 1994.

[71] S. Blügel, "Magnetische Anisotropie und Magnetostriktion (Theorie)", in *Magnetische Schichtsysteme*, 30. IFF-Ferienkurs Jülich, Forschungszentrum Jülich GmbH, Jülich, 1999.

[72] C. Kittel, *Einführung in die Festkörperphysik* (R. Oldenbourg Verlag, München, 1996).

[73] R. R. Gupta, *Landolt-Börnstein, Vol. 16, Diamagnetische Suszeptibilität* (Springer Verlag, Berlin, Heidelberg, 1986).

[74] T. R. McGuire and R. I. Potter, IEEE Transactions on Magnetics **MAG-11**, 1018 (1975).

[75] J. P. Jan, "Galvanomagnetic and thermomagnetic effects in metals", in *Solid State Physics*, vol. 5, F. Seitz and D. Turnbull (Eds.), Academic Press, 1957, pp. 1-96.

[76] J. Smit, Physica XVI, no. 6 (1951).

[77] A. Fert and C. Vouille, "Magnetoresistance overview: AMR, GMR, TMR, CMR", in *Magnetische Schichtsysteme*, 30. IFF-Ferienkurs Jülich, Forschungszentrum Jülich GmbH, Jülich, 1999.

[78] A. Fert and P. Bruno, "Interlayer Coupling and Magnetoresistance in Multilayers", in *Ultrathin Magnetic Structures*, vol. 2, J.A.C Bland, B. Heinrich (Eds.), Springer-Verlag, Berlin, 1994.

[79] N. F. Mott, Adv. Phys. **13**, 325 (1964).

[80] M. N. Baibich et al., Phys. Rev. Lett. **61**, 2472 (1988).

[81] G. Binasch et al., Phys. Rev. B **39**, 482 (1989).

[82] P. Grünberg, Phys. Rev. Lett. **57**, 2442 (1986).

[83] R. I. Potter, Phys. Rev. B **10**, 4626 (1974).

[84] W. Nolting, *Grundkurs: Theoretische Physik Band 6* (Verlag Zimmermann-Neufang, Antoniusstraße 9, 56766 Ulmen, Germany, 1996).

[85] D. P. Landau and K. Binder, *A guide to Monte Carlo simulations in statistical physics* (Cambridge University Press, Cambridge, UK, 2000).

[86] K. Kawasaki, in *Phase Transitions and Critical Phenomena*, vol. 2, C. Domb and M. S. Green (Eds.), Academic Press, London, 1972.

[87] N. Metropolis, A. W. Rosenbluth, M. N. Rosenbluth, A. M. Teller, and E. Teller, J. Chem. Phys. **21**, 1087 (1953).

[88] L. Onsager, Phys. Rev. **65**, 117 (1944).

[89] H. J. Elmers, "Magnetismus dünner Filme", in *Magnetische Schichtsysteme*, 30. IFF-Ferienkurs Jülich, Forschungszentrum Jülich GmbH, Jülich, 1999.

[90] R. H. Swendsen and J.-S. Wang, Phys. Rev. Lett. **58**, 86 (1987).

[91] J.-S. Wang, Physica A **164**, 240 (1990).

[92] U. Wolff, Phys. Rev. Lett. **62**, 361 (1989).

[93] A. Heuer, B. Duenweg, and A. M. Ferrenberg, Comput. Phys. Commun. **103**, 1 (1997).

[94] S. Wiseman and E. Domany, Phys. Rev. Lett. **81**, 22 (1998).

[95] S. Wiseman and E. Domany, Phys. Rev. E **52**, 3469 (1995).

[96] R. B. Griffiths, Phys. Rev. Lett. **23**, 17 (1969).

[97] B. M. McCoy, Phys. Rev. Lett. **23**, 383 (1969).

[98] J. F. Dillon, Jr., E. Y. Chen, and H. J. Guggenheim, Solid State Commun. **16**, 371 (1975).

[99] C. Binek and W. Kleemann, Phys. Rev. Lett. **72**, 1287 (1994).

[100] C. Binek, M. M. P. de Azevedo, W. Kleemann, and D. Bertrand, J. Magn. Magn. Mater. **140-144**, 1555 (1995).

[101] S. Kirkpatrick and E. Stoll, J. Comput. Phys. **40**, 517 (1981).

List of Publications

Preparation and Structural Analysis of $\mathrm{Fe}_{2+x}\mathrm{Ti}_{1-x}$ Thin Films in the C14 Laves Phase Stability Range
J. Köble and M. Huth
Journal of Crystal Growth **234**, 666–678 (2002).

Induced Unidirectional Magnetic Anisotropy in $\mathrm{Fe}_2\mathrm{Ti}$ Thin Films
J. Köble and M. Huth
Proceedings of the 8th **E***uropean* **M***agnetic* **M***aterials and* **A***pplications Conference 2000, Kiyv, Ukraine*
Material Science Forum **373**, 137–140 (2001).

Controlling the Intralayer Structure of Co/Pt-Superlattices
P. Haibach, J. Köble, M. Huth and H. Adrian
J. Magn. Magn. Mater. **198–199**, 752-754 (1999).

MgO Surface Microstructure and Crystalline Coherence of Co/Pt-Superlattices
P. Haibach, J. Köble, M. Huth and H. Adrian
Thin Solid Films **336**, 168-171 (1998).

Acknowledgements

At this point I would like to mention that the present work was only made possible with the help of many people.

The whole work was supervised by Dr. M. H. who went never tired of giving help and advice in situations that seemed to be stuck. The discussions with him quite frequently turned my dejection due to obviously bad results into new perspectives. His exemplary support, his vast knowledge and his good ideas vitally improved the quality of this work. The time he spent for the final corrections of the thesis cannot be taken for granted.

I also wish to thank Prof. Dr. H. A. who accepted me as a member of his work group and eventually made possible my participation in research and the presentation of my results on several conferences in Germany and abroad. The very good equipment of the labs and his support of the work group were essential for the efficient completion of the present work.

Furthermore, I must say that I really enjoyed the work in the lab with my colleague and room mate J. O. who was always ready for help and discussion. I must also thank him for his condolence on my breaking of several crucibles while trying to evaporate iron and beg forgiveness for stealing his preparation time...Wir waren nie wirklich unzufrieden, oder ?

Without the technical experiences and ideas of J. H. most instruments and installations in the labs would not be running. I am glad that he always took at least a short amount of his precious time to aid me in my work.

Special thanks must go to A. D. who performed uncountable EDX measurements on my samples. The high accuracy of her measurements was crucial for the whole experiment.

The work group of Prof. A. has been a second family for me and I enjoyed not only the daily work with its members but also the private events that were not neglected. Especially Dr. M. B. took great care of our ”family” (Go, Mainz 05, go !!!).

My whole work is, however, a consequence of the nice cooperation with the former supervisor of my diploma thesis Dr. P. H. who virtually introduced me to the secrets of thin film preparation. I enjoyed several bottles of beer with him, too.

From the technical stuff of our institute three persons are to be mentioned as representatives: Mr. G. and Mr. G. who took care of the "cool fluid of life", i.e. the liquid Helium so crucial for the SQUID magnetometer. P. B. represents the reliable work of the mechanical workshop .

Additionally, I want to thank Dr. W. P. of the work group of Prof. B. for his essential hints to the performance and interpretations of the Monte Carlo simulations.

The Rutherford backscattering analysis was performed by Dr. G. L. and Dr. J. G. of the Forschungszentrum Karlsruhe who thus earn my best regards. Furthermore, without the proper maintenance of the 4-circle diffractometer by Dr. habil. L. W. another important part of this work would not have been realized.

I must not forget the efforts of my old school mate M. G. who had to suffer the correction of my physicists english language and spent his precious time for me.

Finally, without the support of my family and the psychological care of my wife J. I would have never made it that far.

This work was supported by the Materialwissenschaftliches Forschungszentrum Mainz.

Eidesstattliche Erklärung

Hiermit erkläre ich an Eides Statt, dass ich die vorliegende Arbeit selbstständig und nur unter Verwendung der angegebenen Hilfsmittel angefertigt habe.

Bisher habe ich noch keinen Promotionsversuch unternommen.
Mainz, Dezember 2001